Application of CCDs (Charge Coupled Devices) to Polarimetry and Spectropolarimetry

by

Jaber Naghizadeh-Khouei, B.Sc., M.Sc.

Thesis
submitted to the
University of Glasgow
for the degree of
Ph.D.

Astronomy and Astrophysics Group
Department of Physics and Astronomy,
University of Glasgow,
Glasgow G12 8QQ

March 1998

ProQuest LLC.
789 East Eisenhower Parkway
P.O. Box 1346
Ann Arbor, MI 48106 – 1346

To

my brother Nasa

for his patience and love.

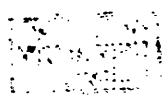

Acknowledgements

It has been a rather long and tiring journey to complete this thesis and I feel that I could not have made it without the support and friendship of certain people.

Primarily, my sincere thanks goes to Dr. David Clarke, who has been throughout this scholarly odyssey an excellent mentor, patient, encouraging, inspirational and supportive. Thanks to Dr. Clarke I avoided many errors, and I was taught a great deal on how to arrange my thoughts, express myself in a clear scientific manner and be consistent with my writing. It is also with great pleasure to acknowledge and thank Dr. Clarke for his friendship.

Further thanks are due to Mr. Colin Hunter for making and assembling the stellar polarimeter and the blue sky spectropolarimeter. His help in installing and ferrying the instruments back and forth for modifications from Cochno station was immeasurable. Thanks also goes to many people at RoE, mainly Horst Hendimerick who introduced me to the Starlink packages and for his help in writing some of the software programs to analyse the blue sky data.

There are numerous friends past and present who have kept my spirits up in Glasgow. To mention but few, Tasos, Richard and Victor.

Summary

Ideally, we would like to have at our disposal a "universal" instrument which could record all available information, i.e. the full Stokes vectors I, Q, U, V as function of spatial co-ordinates X and Y and wavelength λ at given time t. The practical limitations of spectral dispersers now being used for high resolution observations, narrow band filters or spectrographs each permit only the measurement of a limited sub-set of these parameters. Filters record $I(X, Y)$ at a fixed wavelength and the spectrograph record (I, λ, Y) at a fixed X, where X is the direction perpendicular to the slit and Y along it. An important element to any instrumentation is the detector system and to achieve the above, a detector system must possess 2-dimensional characteristics. The application of CCDs to stellar polarimetry has been slow, one problem being that the polarimetric modulators favoured with photomultiplier detection are not immediately applicable. Since, instrumental, observational and data reduction techniques are very different in these two detector systems.

At the start of this work (1991) high-precision polarimetric data are obtained by polarimeters which employ photomultiplier detectors, with measurement accuracy controlled by photon counting statistics. For low levels of polarization, simple error analysis provides uncertainty estimates for q and u of $\sigma_q = \sigma_u = (\frac{2}{N})^{\frac{1}{2}}$ where N is the total photon counts. Current errors may sometimes be quoted as low as $p \sim \pm$ 0.0001 so requiring photon counts just greater than 10^8. The photon detection rate for stars in usually $\sim$ or $> 10^5 s^{-1}$ such that the required integration times are $\sim$ 1000 seconds. For large aperture telescopes and for measurements of the brighter stars, the photoelectron production rate may be embarrassingly high, ($\sim$ or $> 5 \times 10^5 s^{-1}$). At such rates, dead-time problems associated with photon counting systems may be apparent, introducing measurements bias on q and

u greater than their estimated errors. Chapter 2 highlights such effects in results claiming to detect short term temporal changes in line-of-sight interstellar dust column. Most polarimetrists are aware of the dead-time problem and avoid it by using neutral density filters to reduce the detectable flux and then extending the experimental time to accumulate the necessary photon count - a somewhat defeatist solution. With the purpose of increasing efficiency and improving the measurement accuracy, it is important that new techniques should be explored.

Chapter 3 describes an alternative way of observing low levels of stellar polarization. The technique involves recording equally exposed frames at fixed orientation of the modulator. This required four CCD exposures with the half-wave plate setting at 0°, 45°, 22.5° and 67.5°. One of the problems in using a CCD for observations of bright stars is that CCD pixels cannot handle a very high photon flux. The CCD will saturate in a short time, and the result will be shorter integrations to avoid saturation. A way of getting more photons on one CCD exposure is to defocus the star and, by that, spread the light over a larger area on the CCD (e.g. 5000 pixels). In order to test this method a polarimeter was built to observe the defocused stars. It is demonstrated that it is possible to detect low levels of polarization by this defocused method. The data presented shows that from a single run of $4 \times 30s$ exposures of the bright unpolarized standard star, θBoo (mag 4.05), with $\sim 3 \times 10^5$ electrons per pixel and with 3000 pixels, the standard error is $< \pm\ 0.0001$, an accuracy that could only be achieved by a photoelectric polarimeter using an integration time $\sim 10\times$ longer. These results indicate the power of the technique in its application to accurate measurements of low polarization associated with bright stars.

Spectropolarimetric instrumentation is described with presented measurements of the Ring effect (Fraunhofer line filling-in) in the light of the daytime sky. Although Rayleigh scattering is wavelength independent, there is a $p(\lambda)$ variation in the light from the sky caused by absorption, secondary scattering, ground reflection, etc. In addition, at high spectral resolution, polarization variations can be detected across the solar Fraunhofer lines, the cause being associated with an intensity line filling-in effect (Ring effect). Most research in this area relates to the "straight forward" recording of temporal variations of line depth intensities. There is, however, no consensus on the behaviour as recorded by different observers. One explanation for this is that variable polarization features are

also present and these may affect the recorded profiles according to the individual spectrometer senstivities to polarized radiation. The only way to investigate the phenomenon meaningfully is by spectropolarimetry.

So far spectral line $p(\lambda)$ investigations have been performed by sequential measurements alternating between wavelength positions corresponding to the line core and the nearby continuum. This kind of observational technique is inefficient and the results provide no real understanding of the phenomenon. A 2-D detector system capable of undertaking multi-point spectropolarimetry is desirable.

The spectropolarimeter described in Chapter 4 consists of a polarimetric modulator (a rotatable superachromatic half-wave plate) followed by a high quality plastic sheet polarizer all placed prior to the slit of the spectrometer. A variation of Fessenkov's method was employed whereby three frame sets were recorded at half-wave plate orientations separated by 30°. Observations were conducted at Glasgow University Observatory.

Because of the rapid secular changes in brightness and polarization resulting from the continuous apparent solar movement, the spectral data for each wave-plate orientation from the long series of measurement were stored so that the three necessary intensities required to calculate each value of polarization and position angle could be interpolated for unique times. Observations were carried out only on absolutely cloudless skies to avoid inhomogeneities in the sky brightness distribution. Two Fraunhofer lines were chosen for this study, namely magnesium triplet ($\sim$ 5183Å) and H_β ($\sim$ 4861Å).

New polarization "anomalies" were discovered in the spectra of the blue sky. Photometric analysis was undertaken where the ratio of line bottom to continuum showed that there are no diurnal changes in the spectral profiles of the blue sky. This contradicts others workers in which they claim that there is a diurnal change within the spectral lines. It is suggested that the previous observations may have contained instrumental effects.

The spectral observations show that at large scattering angles, depression in polarization occurs on the blue shoulders of the magnesium triplet lines with a small enhancement in the red shoulder continuum. At low scattering angles there is no detectable variations in polarization across the line feature. The polarization spectra of Hβ line show no such

effects at large scattering angles. However, at small scattering angle the effects are similar to those of the magnesium line. It is shown that these depressions and enhancements depend on the relative amounts of secondary scattering both of the Rayleigh and Raman components.

Some of the research in this thesis has already been published. The list of publications are as follows;

Section: Chapter 2, Section 3.1

Title: "A Reassessment of Some Polarization Standard Stars"

Authors: D. Clarke and J. Naghizadeh-Khouei

Journal: *The Astronomical Journal*

Year: 1994

Volume: **108**, No. 2

Pages: 687–693.

Section: Chapter 3 & 4

Title: "Polarimetry Using CCD Detectors"

Authors: D. Clarke and J. Naghizadeh-Khouei

Book: *Proceeding of the Eighth Conference on Sensors and their Applications*

Editors: A.T. Augousti and N.M. White

Publishers: Institute of Physics

Year: 1997

Pages: 303–308.

Contents

Chapter 1

Introduction

1.1 Introduction to Polarimetric Parameters

The oldest astronomical detector is the human eye. The eye, however, is very subjective, the basic signal is not available for processing outside the immediate impression within the brain. Important too, is that it is generally insensitive to any polarization carried by the radiation. Any astronomical observation of a source consists of extracting a certain subset of the received radiation and measuring its characteristics with the help of one or more detectors. This incident radiation can thus be measured and studied in many ways to further our understanding of astrophysical sources. One quality which electromagnetic waves possesses is called "polarization". Polarization describes the degree to which the direction of the electric or magnetic vector changes in a regular fashion.

Optical polarimetry is a term which has recently been adopted to denote any type of optical measurements where light polarization plays a key role, and where polarization itself is a carrier of information. It also refers to measurement of the state of polarization of light which is emitted from various sources, over a wide range of wavelength, or which is scattered by different objects. The sources may range from minute atomic samples to entire galaxies; and the objects may range from atoms, molecules or microscopic particles to whole planets and stars.

A full mathematical description of the polarization quality of light was given by Stokes (1852), who introduced four quantities now known appropriately as the Stokes's parameters. These are expressed only in terms of direct observables of the electromagnetic field, namely, the intensities and the relative phase difference between the orthogonal wave components. In addition they are applicable to completely polarized or partially polarized light. Thus, they give a complete description of the state of polarization.

Consider the electric disturbance of a pair of classical waves which are orthogonal to each other, such that (cf. Born and Wolf, 1965),

$$E_l(t) = E_{l0}\cos[\omega t + \delta_l(t)] \tag{1.1}$$

$$E_r(t) = E_{r0}\cos[\omega t + \delta_r(t)] \tag{1.2}$$

where E_{l0} and E_{r0} are the amplitudes (constants), ω is the angular frequency and $\delta_l(t)$, $\delta_l(t)$ are the phases, all at instantaneous time t. For such a beam as described, the Stokes' parameters may be expressed as;

$$\begin{aligned} I &= E_{l0}^2 + E_{r0}^2 \\ Q &= E_{l0}^2 - E_{r0}^2 \\ U &= -2E_{l0}E_{r0}\cos\delta \\ V &= 2E_{l0}E_{r0}\sin\delta \end{aligned}$$

You might relate this to "nature" by developing the Stokes' parameters to include the notion of time/wavelength averaging and that

$$\begin{aligned} I &= < E_{l0}^2 + E_{r0}^2 > \\ Q &= < E_{l0}^2 - E_{r0}^2 > \\ U &= < 2E_{l0}E_{r0}\cos\delta > \\ V &= < 2E_{l0}E_{r0}\sin\delta > \end{aligned}$$

The Stokes' parameter I is simply the intensity of the beam. Generally, the Stokes' parameters are normalized to the total intensity and written as $q = \frac{Q}{I}$, $u = \frac{U}{I}$ and $v = \frac{V}{I}$. The v parameter (circular polarization) is of no real concern in this thesis. When describing linear polarization only two Stokes' vectors are used, namely, $\{q, u\}$. It follows that the degree of linear polarization, p and its azimuth Ψ are;

$$p = (q^2 + u^2)^{\frac{1}{2}} \quad \text{and} \quad \Psi = \frac{1}{2} \arctan \frac{u}{q}$$

The degree of polarization, p, is generally expressed as a decimal fraction or in percentage notation. For example, $p \simeq 0.60$ or 60 percent, is common for terrestrial blue sky, while the precision of the stellar polarimetry reported in this thesis is typically about $\leq \pm 0.0001$ or ± 0.01 percent. [Precision is used to define the standard error (σ) of the mean measured value of p (or q, u).]

Detailed expositions and terminology and physics of polarized light can be found in the books by Clarke and Grainger (1971), Shurcliff (1967) and Gehrels (1974).

1.2 Application of Polarimetry to Stellar Sources

The great promise of astronomical polarimetry is that the observed polarization of astronomical objects might provide useful geometrical insight into the nature or behaviour of an object that cannot be resolved by any other means. Optical polarimetry has had mixed results as an astronomical tool, largely because the results have been difficult to interpret. Polarimetry can make both important quantitative and qualitative contributions to astronomy. For example, the polarimetric identification of sulphuric acid in the atmosphere of Venus by Young (1973) and the determination of the inclination of binary systems by Rudy and Kemp (1978) are the good examples of its quantitative potential.

The first (theoretical) step towards the concept of intrinsic stellar polarization was taken by Chandrasekar (1946, 1947) who published the solutions of the radiative transfer equation in an illuminated plane parallel atmosphere with Rayleigh scattering. This work predicted that in early-type single stars where electron scattering is the predominate source of opacity, radiative asymmetry is present, with limb polarization predicted at 12%. Symmetry

over the stellar disk would produce an overall zero polarization, but Chandrasekar suggested that polarization might be observed in certain eclipsing binary system. A binary system containing a hot early-type star and a cooler companion, the eclipsing of the hot star should result in a breaking the of polarization symmetry - thus resulting in a variable polarization during the eclipse phase. Measurements of the eclipsing binaries U Sag and RY Per by Janssen (1946) and Hiltner (1947) showed no net polarization from these systems. It was apparent that the intensity variable polarization effects were too small to be detected by photographic polarimeters.

Fortunately, commercially available photoelectric sensors (in particular, the photomultiplier) were coming into regular use. Both Hall and Hiltner developed photoelectric polarimeters. Their search for the intrinsic polarization effects from eclipsing binary system (CQ Cep) showed a constant polarization, also present in many field stars at similar distances. Further independent studies by Hall (1949) and Hiltner (1949) showed that the light from the majority of distance stars, irrespective of spectral type, exhibit linear polarization. Hiltner and Hall are credited with the serendipitous discovery of interstellar polarization (ISP).

Following the discovery and through subsequent work on the wavelength dependence of the ISP, many of the properties of the interstellar medium have been determined. For instance much has been learned about the size distribution and chemical composition of the interstellar dust. Another well studied feature of the interstellar medium is the structure of the Galactic magnetic field determining its direction. Aligned polarization vectors trace the field lines through the paramagnetic grain alignment mechanism of the Davis and Greenstein (1951).

For example Dyck et al. (1971) found a correlation between polarization and infra-red excess in very late type stars (see Figure 1.1) and Kruszewski et al. (1968) observed a maximum in the degree of polarization at minimum light for v CVn. Figure 1.2 shows a typical set of such observations.

The main asymmetries giving rise to astronomical polarization are magnetic fields and non-uniform distributions of scattered radiation. Polarimetry is the most direct method

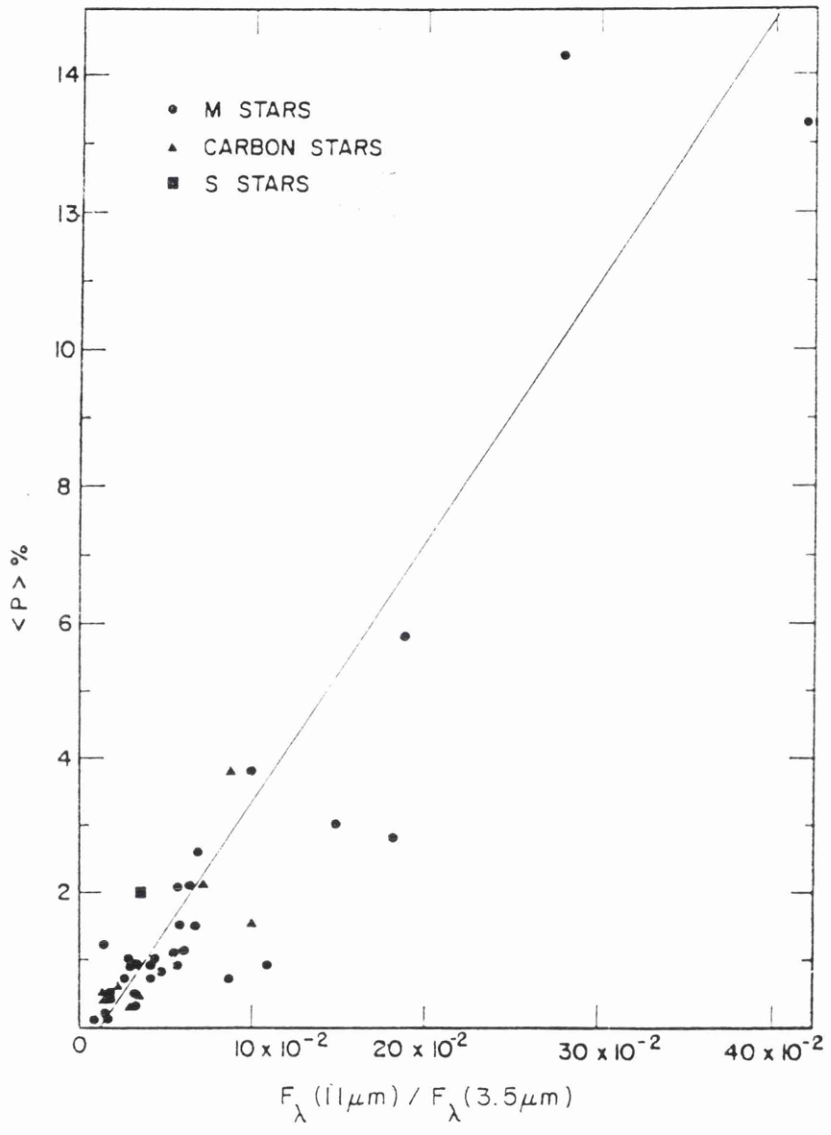

Figure 1.1: Evidence of correlation between infra-red excess and degree of polarization. [Taken from Dyck et al. 1971]

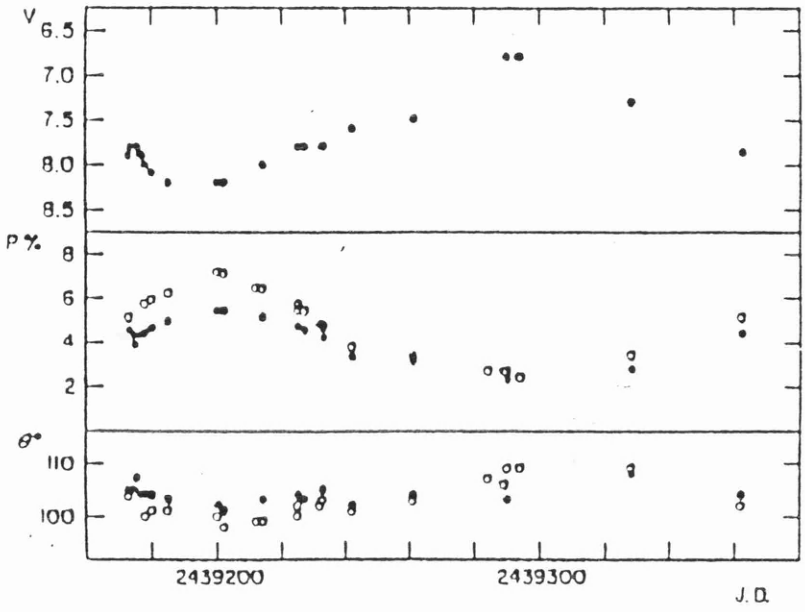

Figure 1.2: Time variability in visual light, polarization and position angle of a CVn star. [Taken from Kruszewski et al. 1968]

of detecting magnetic fields, which in astronomy range from 10 micro-gauss in interstellar space to tera-gauss in pulsars. Searches for intrinsic polarization due to magnetic fields was initiated mainly by Babcock (1947) on peculiar Ap stars through the Zeeman effect. Be stars, with their equatorial electron disks, provide an asymmetric scattering generating values of $p \sim 1\%$ (Serkowski, 1970).

With the improvement in p accuracy, through developing technology, it later became possible to detect intrinsic effects generated by the stars themselves, these being related to particular spectral types, etc.

Since the degree of intrinsic polarization of starlight is usually of order one percent or less, the original method of measurement, using photographic plates, could only be applied to a small number of highly polarized stars. The lower limit of the photographic detection of, p, is 5 to 10%, while modern photoelectric devices and two-dimensional detectors such as CCDs, can measure polarization levels to accuracies of about 0.001%. Hence the advent of these detectors have accelerated the development of more accurate photometric and polarimetric instrumentation. Table 1.1 gives an indication of the remarkable range of polarization and the diversity of polarization sources encountered in astrophysics.

There are far too many polarigenic mechanisms occuring in astrophysical situations to be

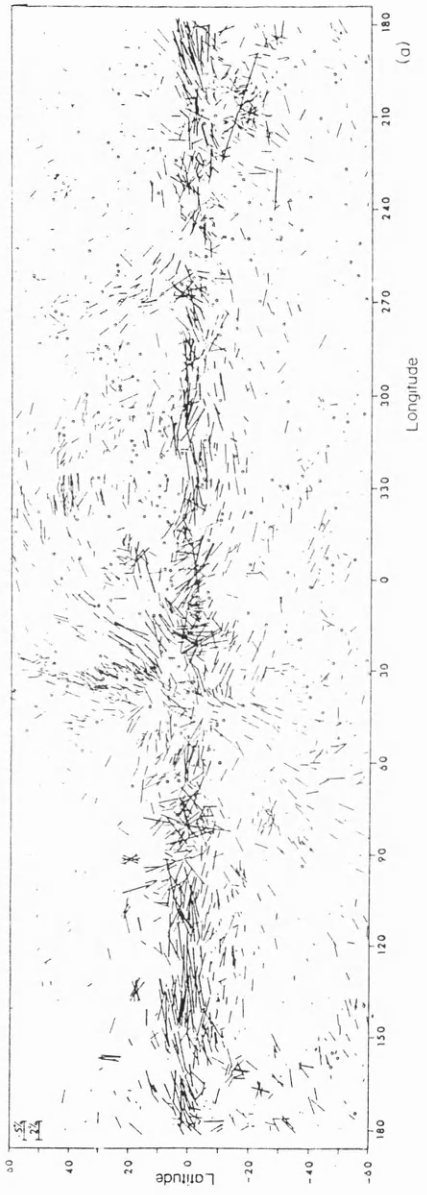

Figure 1.3: Polarization vector associated with ISP indicate the general form of the Galactic magnetic field. [Taken from Mathewson and Ford 1971]

listed in this thesis. Some of the mechanisms giving rise to linear and circular polarization are as follows.

- **Scattering of light by small grains**: zodiacal light, comets, Venus, Jupiter, reflection nebulae, atmospheres of late-type stars, spiral galaxies, interstellar polarization.
- **Scattering of light by molecules (Rayleigh scattering)**: Terrestrial Blue sky, Jupiter and other outer planets, Venus.
- **Scattering of light by free electrons (Thompson scattering)**; solar corona, envelopes of early-type stars.
- **Hanle effect**: Due to resonance scattering of bound electrons in magnetic field. Linear polarization in emission lines of solar chromosphere and corona.
- **Zeeman effect**: sunspots and magnetic stars (circular and linear polarization in spectral lines).
- **Synchrotron emission**: crab nebula, pulsars, galactic radio emission, quasars.

Most of the earlier observations were made using broad passbands or with just one wide-band filter giving only a crude wavelength resolution or none at all. Advances in polarimetric optics have also contributed to this increase in measurement accuracy. For instance Serkowski (1974a) and Tinbergen (1974) have described the various optimum combinations of optical elements such as half- and quarter-wave plates, superachromats and efficient, wide band polarizers. Schemes to compensate automatically for sky background light polarization have proposed by many workers (see Serkowski, 1974a and Metz, 1979).

An era has now arrived in which polarimetry can be performed at high spectral and spatial resolution, using low noise detectors with high detector quantum efficiency. There are many cases were the improvement of polarimetric accuracy has increased our knowledge of astrophysical phenomena. It would be beyond the scope of this thesis to consider every theoretical and observational case. An example, however, is that of Clarke and Bjorkman (1998) who have made a polarimetric study of the Be binary star ϕ Persei.

Polarization Source	**Linear (p)**
Planets	$> 20\%$
Interstellar Dust (Linear)	10%
Interstellar Dust (Circular)	0.05%
Sun and Ap Stars (Zeeman effect)	100%
Be Stars	$\sim 1\%$
Algol Binaries	0.02%
White dwarfs (Zeeman effect)	12%
Symbiotic stars (Raman scattering)	8%
Reflection Nebulae (including Herbig-Haro & Bipolar)	60%
Synchrotron (Crab Nebula, Blazers)	50%
Synchrotron (extragalactic jets)	20%

Table 1.1: Maximum observed or expected degree of polarization at optical wavelengths.

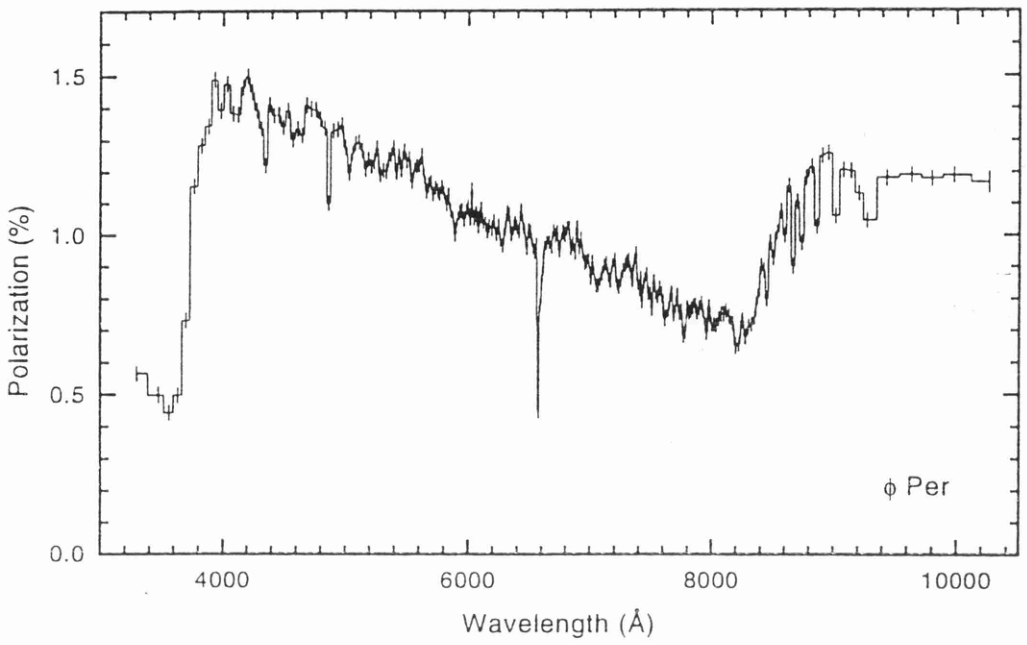

Figure 1.4: A sample of spectropolarimetric data for ϕ Per. Individual pixels provide $\Delta p \sim 0.005$ and combination to simulate a broader band allows $\Delta p \sim 0.00001$ to be achieved. [Taken from Clarke and Bjorkman 1998]

Their observations show an increase in accuracy by a factor of just greater then ten over the usual reported stellar polarimetry. Clarke and Bjorkman (1998) state in their conclusions;

> Differences in instrumental off-sets and/or long term changes in the stellar scattering cloud and the relatively poor accuracies of the early data set prevented any meaningful outcome.

They have shown that for measurements with accuracies $\Delta p \approx 0.003\%$, new phenomena related to the geometry of the ϕ Per system has been revealed. Their work promotes the notion of the usefulness of striving to achieve polarimetric accuracies of $\Delta p \approx \pm 0.001\%$. Their spectropolarimetric observations (see Figure 1.4) were carried out with a CCD detector and with the data averaged into the equivalent of six passbands to increase the general accuracy.

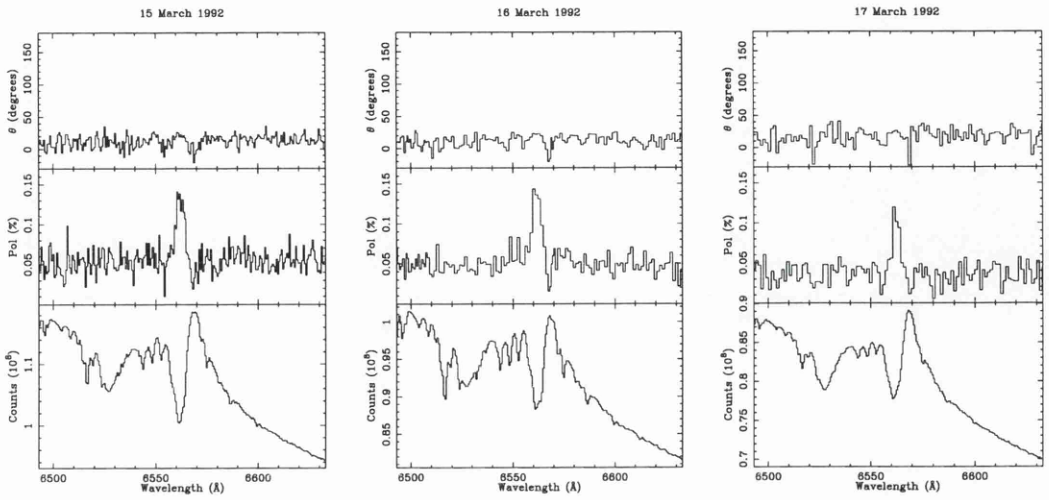

Figure 1.5: Spectropolarimetric observations of ζ Puppis binned to a constant error of 0.02%. [Taken from Harries and Howarth 1996]

Another example is the observations of hot stars, which show mass loss via hot, highly-ionized stellar winds possibly driven by radiation pressure. For rapidly rotating stars theory predicts that the mass-loss will be more extensive at the equator, due to the reduction of the effective surface gravity caused by the centrifugal force. Although Howarth and Prinja (1989) observed a positive correlation with $v \sin i$ and mass-loss rate in their sample of >200 O stars, there is little direct evidence for wind asphericity in normal O-stars in the literature. Harries and Howarth (1996) have made spectropolarimetric observations of a rapidly rotating O4 supergiant ζ Puppis. Figure 1.5 clearly shows a change in polarization vector at Hα and it is stable in the continuum and line polarization over the three nights. The authors have concluded that the structure is a flattened wind due to the star's rapid rotation. The above conclusion could not have been made without, Δp being $< 0.02\%$.

It is self-evident that improving p accuracy is a worthwhile pursuit.

1.3 Polarimetry of the Terrestrial Blue Sky

The earliest recorded application of polarimetry to terrestrial blue sky was by Arago in 1809. He discovered that the light from the sunlit sky is partially polarized and established the fact that the polarization maximum in the sky is located at about 90 degrees from the Sun. He also discovered the existence of a point zero polarization (neutral point of Arago) at position 20 - 25 degree above the antisolar direction. There are two other neutral points that normally exist in the sunlit sky, the Babinat and Brewster points discovered in 1840 and 1842 respectively.

It was not until 1871 that an explanation of the polarization of the blue sky was first provided by Lord Rayleigh. Lord Rayleigh (1871) described this phenomena in terms of scattering by particles of size much smaller than the wavelength of light and showed that the scattered brightness varies according to a $\frac{1}{\lambda^4}$ law.

He showed further that a fraction, $\frac{1}{(1+\cos^2\theta)}$, of the scattered light will be polarized in the plane perpendicular to the plane of the scattering and a fraction, $\frac{\cos^2\theta}{(1+\cos^2\theta)}$, will be polarized in that plane. Hence, the degree of polarization, $\frac{(1-\cos^2\theta)}{(1+\cos^2\theta)}$, will be zero in and opposite to the incident direction. It is also expected that a 100 percent polarization will be obtained at an elongation of 90° from the sun. While his theory explained several of the observed features of the colour and polarization of the blue sky, however it failed to account for the location of the neutral points and the fact that the maximum value of the degree of polarization does not reach 100 percent. Lord Rayleigh attributed this to the phenomena of multiple scattering in the Earth's atmosphere, which results in a depolarization. It has become evident that the deviation of the actual polarization field of skylight given from the elementary scattering theory is due to a combination of molecular anisotropy, multiple scattering, atmospheric aerosols, and reflection of light from the local ground cover be it soil, sand, vegetation, water, etc. (see Coulson, 1974).

The contribution of these effects to the sky brightness and polarization make the modelling that much more complicated. All of the scattering mechanisms operating in the terrestrial atmosphere have been considered to be elastic processes, that is processes in which no change in the wavelength of the scattered light occurs.

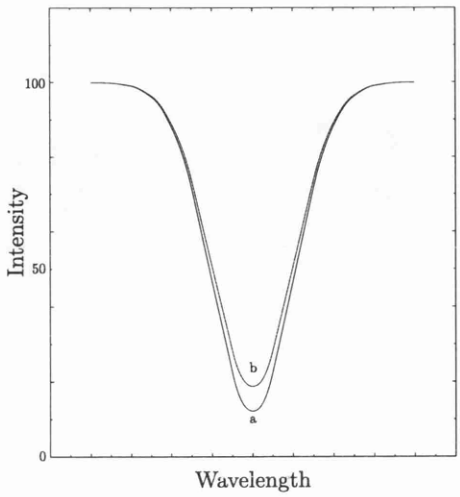

Figure 1.6: comparison of the spectrum of direct sunlight (a) and of scattered skylight (b).

There is also an observational phenomenon referred to as a "filling-in effect", or the "Ring effect", whose origin remains an enigma. For many years it was widely believed that the spectrum of the blue sky (except for the $\frac{1}{\lambda^4}$ dependence) was identical to that of the direct Sun. In fact, when the profiles of Fraunhofer lines in the spectrum of the blue sky light are compared with the line profiles from the direct sunlight, the former are found to be less deep (see Figure 1.6). This intensity "filling-in" was first reported by Grainger and Ring (1962) who observed it in the H line of Ca (II).

Grainger and Ring (1962) interpreted the phenomenon in terms of an additional radiation akin to a fluoresence with emission spreading over the spectral domain encompassing the recorded line profiles. Many subsequent spectrophotometric observations of the effect have been undertaken by various researchers but no consensus on its behaviour or on its interpretation has emerged.

The disparity of results and conclusions is clearly seen in the literature. For example, Barmore (1975) demonstrated that the absolute intensity of the added component varies

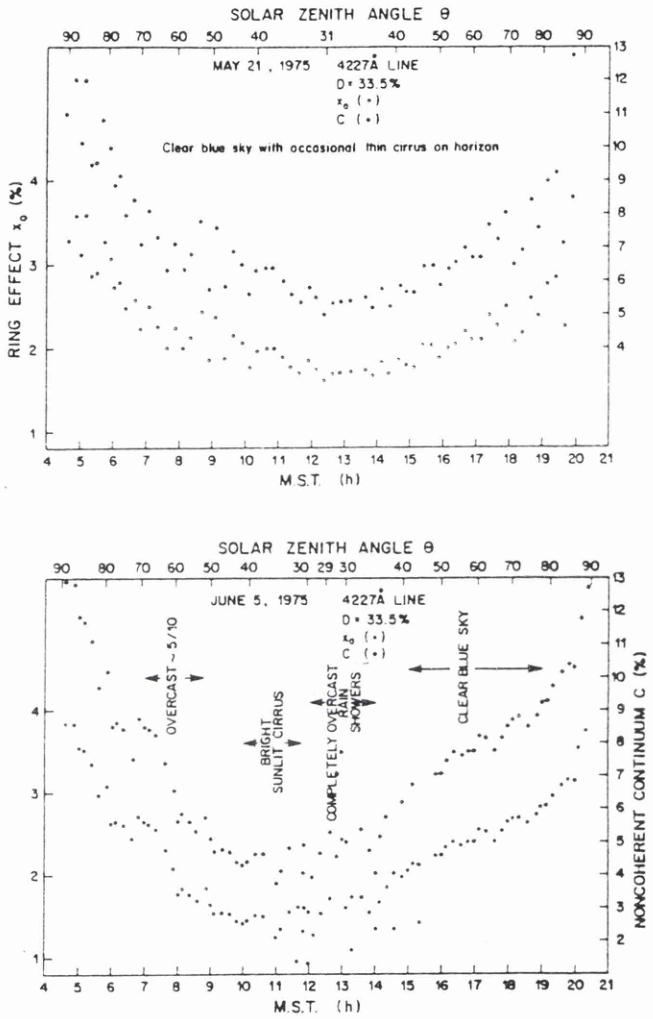

Figure 1.7: Observed variation of measured Ring effect (○) and associated continuum (●) at 4326Å FeI. [Taken from Harrison 1976]

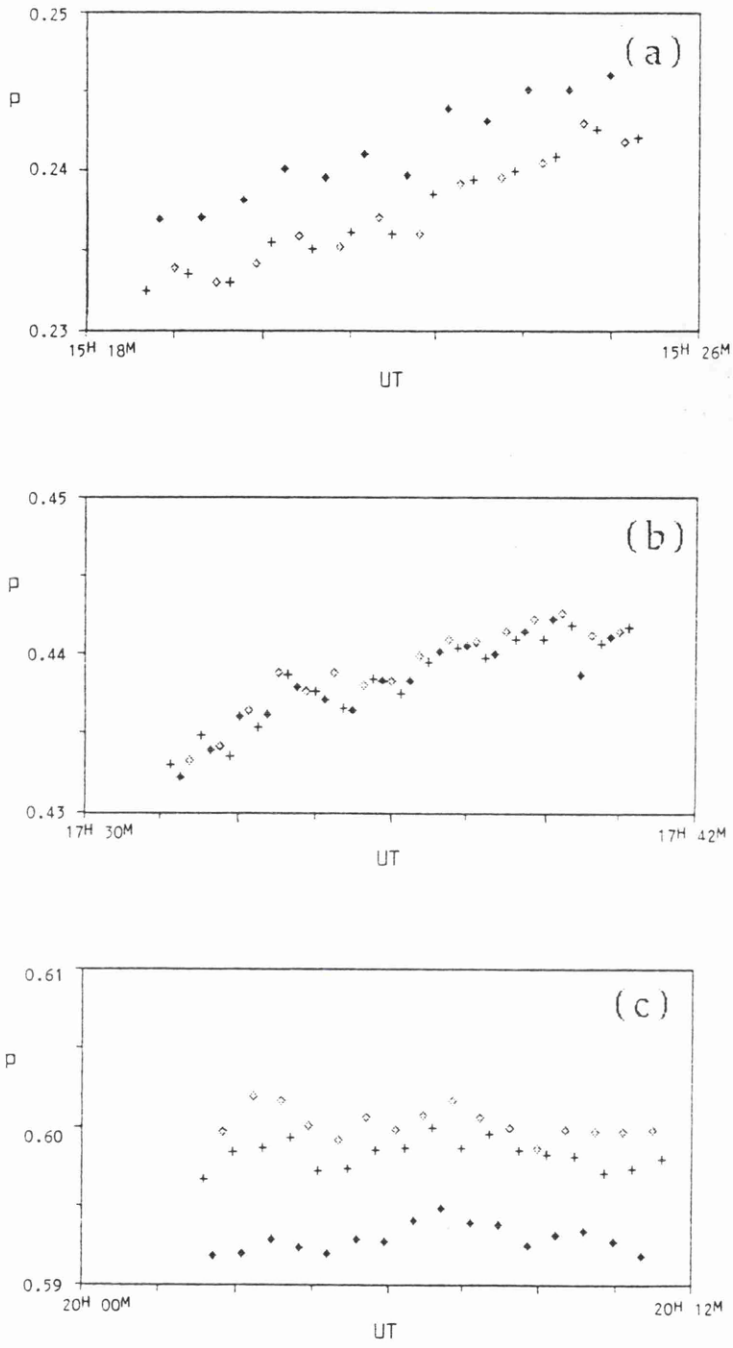

The variation of the degree of polarization, p, at the Hβ line of the zenith sky according to UT during three portions of the day 1988 Jun 24. Points marked ✦ refer to measurements in the core of the line, those marked + , ◇ refer to measurements in the red and blue continua respectively. Part (c) corresponds to solar zenith angles from 86° to 87° and clearly displays records of a reduced polarization at the line centre; part (b) covers solar zenith angles from 67° to 68°, there being no difference of p across the line; part (a) covers solar zenith angles from 48°.5 to 49°.5 and displays an enhanced polarization at the line centre.

Figure 1.8: Time variation of the degree of polarization, p, at H_β line of the zenith sky. [Taken from Clarke and Basurah 1989]

from day to day and lacks coherent trends during a single day. To the contrary, Harrison's (1975) study of the zenith sky revealed smooth changes in the degree of the line filling with a minimum at local noon. Harrison (1976) observed time variations in the Ring effect at selected wavelengths. Figure 1.7 shows the pronounced diurnal variation with the minimum around midday. Proposed mechanisms for explaining the phenomena are numerous including fluoresence from aerosols, producing a bland spectrum across the monitored Fraunhofer line, and the non linear effects of vibrational/rotational Raman scattering from air molecules (see Birnkmann, 1968).

Polarization variations across the Fraunhofer lines have also been recorded and associated with the filling-in effect. Pavlov et al. (1973) reported from the polarimetric observations that the degree of polarization is always 2 – 6 per cent lower at the line centre of the H and K lines than in the continuous spectrum while, for the L and N lines, the depolarization effect is considerably less and occasionally zero. This suggests that the intensity filling-in is much stronger to shorter wavelength. According to line profiles recorded with orthogonal polarization, it was suggested by Noxon and Goody (1965) that the added light is essentially unpolarized.

Clarke and McLean (1975) obtained polarization measurements of the zenith column at the line bottom of H_β and in the adjacent continuum and showed that the recorded reduction of p at the line centre was commensurate with an added unpolarized intensity. Further polarimetry by Clarke and Basurah (1989) revealed a more complicated behaviour with enhancements of p occurring around local noon when the scattering angle formed by the Sun and the zenith column was small, with reductions of p occurring only when the scattering angle is large. Both these latter polarimetric studies were undertaken using a technique which provided basic measurements at the line bottom and at two continuum wavelength values on either side of the line, with the chosen spectral positions being monitored sequentially in a cycle. Figure 1.8 shows the degree of polarization at the three wavelength positions around $H\beta$.

In fact the majority of the previous investigation of the Ring effect, both photometric and polarimetric, have been performed using some form of single channel scanning spectrometer. Also, in most cases, the deductions made about the phenomena have been based on

comparisons of incomplete spectral line profiles, at subjectively selected points within it. This may be part of the cause of the lack of consensus as to its observed behaviour and interpreted nature.

Summary

Clearly there is scope for using CCD's to improve the accuracy of polarimetry for stellar objects and also to perform high quality spectropolarimetry. In this thesis the development and sucess of two prototype instruments will be described.

The first is a novel aperture image stellar polarimeter and the second a spectropolarimeter for investigation of the Ring effect. Before the description of these, it is first necessary to describe the general techniques of polarimetry and this is done in the following Chapter.

Chapter 2

Techniques in Observational Polarimetry

2.1 Introduction

Current polarimetric techniques revolve around either the photomultiplier detectors or a two dimensional system such as a Charge Coupled Devices (hereafter CCDs). Instruments involving the former system are capable of achieving the best accuracies so far, while the latter systems, although having the obvious capabilities of recording many spectral channels simultaneously have not yet been proved out to a large degree. As it turns out, one of the limitations to accuracy of basic photoelectric systems is related to photon counting dead-time and was unearthed by a study of some catalogued data. A discussion of the problem has already been published (see Clarke and Naghizadeh-Khouei, 1994), but for completeness it will be covered again here.

Photoelectric polarimetry dates back to the late 1940s, through the advent of the photomultipliers, whereas CCDs are comparatively new devices and are currently gaining ground in modern polarimetry. As we will see there are several advantages and disadvantages to both of these detectors. Most of the advantages/disadvantages arise either because of the polarimetric technique used or are inherent to the detector itself. Table 2.1 summarizes

some of the advantages of imaging array detectors (e.g. CCDs), where the charge is stored until it is readout by the electronics, over a single channel real-time detectors, where the photon counts are read instantaneously (e.g. Photomultipliers).

As the interest in application of polarimetry grows and the new panoramic detectors become available, it becomes necessary to push the limits of polarization techniques and detectivity further. In the past few decades polarimetry has increasingly become a standard astrophysical technique. The polarimetric technique has been slow to come out of age, the main factor being the generally low levels of astronomical polarization which can be detected.

It is expected that for a polarimetric measurement of a bright star with a modern polarimeter an accuracy in the range of 0.01% should be possible with repeated measurements. In obtaining high polarimetric accuracy one also has to be aware of possible variable systematic errors in the data (see section 2.3.1 of this chapter). If these systematic errors are not accounted for correctly, then one may under/over-estimate their contribution to the measurements.

Ideally, one would like to measure the brightness and polarization state simultaneously. Unfortunately, obtaining polarization spectra and images with high accuracy has been virtually impossible until recently. For optical polarimeters with only one detector channel or only a few channels, the most common choice of sensor is a photomultiplier tube (single element). Photomultipliers are good for individual stellar work. They have been used for spectropolarimetry, but being a single pixel device, sequential scanning is required, making the observations very time consuming, CCDs address this problem.

In astronomical polarimetry and spectropolarimetry and direct imaging systems several forms of multi-element detectors are possible. For example, the photographic plate (Röser, 1981) and electronograph (Warren-Smith et al., 1979), linear arrays of silicon diodes (for spectrographs) (Scholiers and Wieher, 1985), TV cameras such as SIT (Silicon Intensified Target) or SEC (Secondary Electron Conducting) Vidicon (Boksenberg and Burgess, 1973), Digicon (McLean et al., 1979), Reticon (Schectman and Hiltner, 1976), image intensifiers and image dissector scanners (Miller et al., 1980) and, most recently, charge

Real-time Detector (e.g. Photomultipliers)	**Digital Detectors (e.g. CCDs)**
Medium quantum efficiency (typical value of 20% or less)	High quantum efficiency (> 90%)
Cannot have local and simultaneous background measurement	Local and simultaneous background measurements easy to determine
Detector surface response non-uniformity	Response non-uniformity information is easy to obtain; i.e. flatfielding
Glitches (cosmic rays etc.) are hard to remove	Glitches are easily isolated and removed
No spatial information available (1 pixel only)	Spatial information typically $\sim 10^5$ pixels; source easy to isolate
One object measured at a time (different atmospheric conditions for different objects)	Many objects measured at the same time (same atmospheric conditions for all objects in the field)
Seeing excursions make small field of view stop hard to use accurately	Resolution is limited by pixel size
Excellent linearity (at low count rates; but see discussion on dead-time)	Excellent up to saturation level
	Image reduction packages required

Table 2.1: Comparison of the application of photomultipliers and CCDs to stellar photometry and polarimetry.

Detector	Polarimetric Precision
Visual(Planets, Moon)	0.1%
Photographic	$\approx$ 0.5%
Photomultipliers(Stars & Planets)	0.001%
Photomultipliers(Solar)	0.0001%
Charge Coupled Devices(CCDs)	$<$ 0.01% ?

Table 2.2: Polarimetric precision at Optical Wavelengths

coupled devices (CCDs). All of these detectors have in fact been used to varying degrees in astronomical polarimeters to obtain that much sought after multichannel advantage. Digicon was for a time an excellent detector(multichannel) but unfortunately due to its short working life it could not be used effectively. Two polarimetric systems based on Digicon yielded some excellent results (see McLean et al., 1979 and Stockman et al., 1979) and these remain as the paragon of quality.

The greatest problem arises when we try to establish the commensurability between the polarimetric technique and the detectors. The choice of detector also depends on particular astronomical research, thus, we need to be able to match our astronomical requirements with the polarimetric technique and detector. For example, if one wanted to perform polarization measurements on 100 to 200 stars to map the magnetic field in a small interstellar cloud, using a photomultiplier would require 20 nights of observing - whereas use of a 2D detector would allow one to image 10 to 100 stars simultaneously, thus, improving the speed in which the observed data can be recovered.

The major consideration of any astronomical project is the accuracy in which polarimetry is achieved. As already stated in the previous chapter most astronomical sources show small levels of polarization and, therefore, the precision which can be achieved becomes very important, thus, the choice of detectors is crucial. Table 2.2 shows the accuracy we can reach with different detectors.

The reason why polarimetric observations are often rather delicate is that the measurement

is differential (difference between the two orthogonal polarizations). The two intensities are either measured one after another by one detector (single channel), in which case all time-varying attenuation (e.g. the effect of the $\sec\zeta$ law) cause errors, or simultaneously by two different detectors (double channel), in which time-varying attenuation and scintillation are eliminated, but all differences between the two channels (e.g. filters and detectors) cause errors. In practice, with sufficient calibration, the latter solution performs best, because the first method is completely dominated by the very large effects of scintillation. However, if we can only alternate between the two intensities faster than any of the time-varying attenuation (atmospheric), the first method is in principle (and in practice) superior.

Thus, accurate polarimetry demands either the use of rapid optical modulation to switch polarization states on the same detector element or the use of a ratio measurement between orthogonally polarized images of the same source (or a part of source) collected on different detector elements. Clearly, even on the largest telescope, photon arrival rates from faint sources or those observed at high spectral resolution will lead to un-manageably long integration times (see section 2.4, Table 2.3) unless all resolution elements (whether spectral or spatial) are observed simultaneously.

Polarimetric techniques can be classified according to two basic purposes, *viz.*,

- Imaging polarimetry
- Modulation polarimetry

Imaging polarimetry (Photographic plate, Electronographs, CCDs etc.) operates with low precision typically in order of 1%, whereas Modulation (Photomultiplier, CCDs) polarimetry is capable of very high precision (better than 0.01%) mainly in broadband. A detector which can be used in both of these techniques is the CCD, whereas a photomultiplier can only be used in a modulation polarimetry.

2.2 Basic Methods and Options in Polarimetric Measurements

Conceptually, all polarimeters fall into the same basic design structure and can generally be divided into two parts; the optical part, which converts the state of polarization into ratios of intensities and the electronic part, which measures those intensities and is insensitive to the state of polarization. The light from the telescope must in general pass through a polarimetric device (modulator) and then a spectrometric/imaging device to arrive at the detector. Almost always, the last element in the polarimeter is a perfect polarizer, it is either a single beam device (e.g. a polariod or a Glan prism) or a double beam device (such as Savart plate). The emerging light from the polarizer is a beam of completely polarized light whose intensity varies according to the setting of the modulator and, thus, the state of polarization of the incoming light is detected.

A modulator produces variations of the intensity bearing a known relation to the incoming polarization. Following the last element (polarizer) of the modulation, then one may with impunity allow the radiation to be transmitted by filters, gratings, prisms, grisms, etc. There are at present three types of modulators;

- rotating superachromatic half-wave plate which sinusidullay varies the polarized intensity at 4 times the frequency of the mechanical rotation.
- electro-optic devices such as pockel cell, whose phase may be altered by voltages.
- photo-elastic birefringent crystals with fast axis aligned to the application of vibrating stress.

A half-wave plate has a fixed retardance and modulation is achieved by its rotation which is slow, whereas electro-optic (controlled by varying the voltage) and photo-elastic (controlled by vibrations) devices have high modulation frequencies and, therefore, are able to remove scintillation noise in a single channel instrument. These also have drawbacks, since their retardance must be calibrated at different wavelengths. There are several methods available whereby measurements of the intensity at known settings of the modulator can

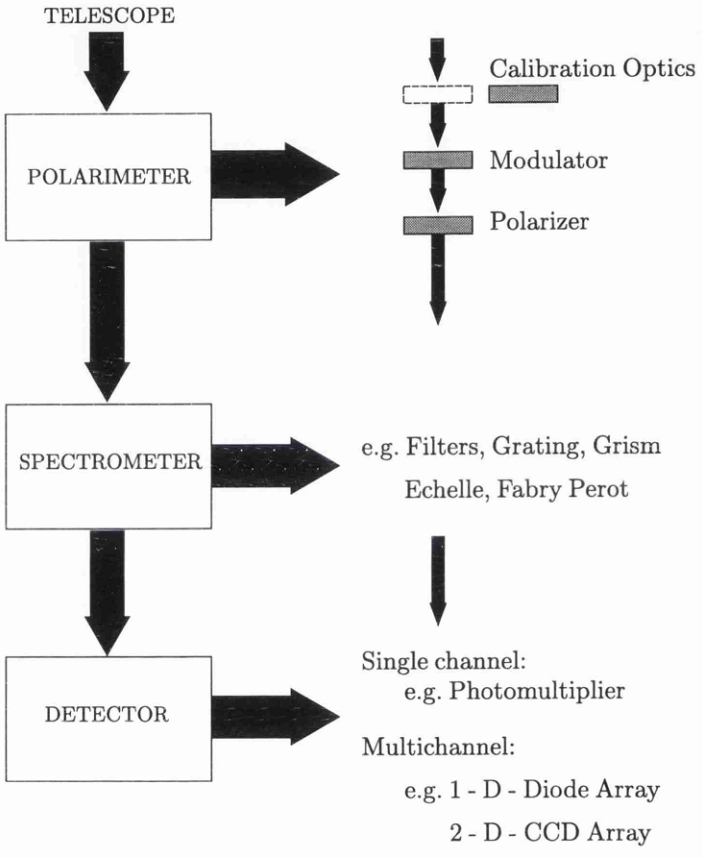

Figure 2.1: Schematic outline of a typical polarimeter indicating the major elements and examples of what these can be in practice

be used to describe the Stokes' parameters Q, U and V (Clarke and Grainger, 1971). Figure 2.1 shows a general layout of a polarimeter. In the design of the two prototype instruments described in later Chapters the modulation comprised a rotatable half-wave plate.

The operation of any modulator can be described in terms of the Mueller calculus with its elements corresponding to 4 × 4 matrices.

$$I_{out} = \begin{pmatrix} I \\ Q \\ U \\ V \end{pmatrix}_{out} = [M] \cdot I_{in} = \begin{pmatrix} \Im_{11} & \Im_{12} & \Im_{13} & \Im_{14} \\ \Im_{21} & \Im_{22} & \Im_{23} & \Im_{24} \\ \Im_{31} & \Im_{32} & \Im_{33} & \Im_{34} \\ \Im_{41} & \Im_{42} & \Im_{43} & \Im_{44} \end{pmatrix} \begin{pmatrix} I \\ Q \\ U \\ V \end{pmatrix}_{in} . \quad (2.1)$$

Since the Stokes' parameters are real quantities, the elements of the matrix are all real numbers. It can be seen that the first element $\Im_{11}$ is always positive since it controls the total light intensity (I). The other parameters can be positive or negative. The first optical component of any polarimeter is a modulator (retarder).

We can calculate the form of the light emerging from the various components of a simple polarimeter by using the appropriate Mueller matrix. The matrix of a component changes when the orientation of that component is changed. If the position angle of the component of Equation 2.1 is increased by $+\psi$, we evaluate its action by first rotating the coordinate system through the same angle $+\psi$ (a natural Cartesian co-ordinate system is chosen whose z-axis is in the direction of the incoming light and where the angle ψ is measured anticlockwise from the x-axis of the frame), then applying the component matrix [M] and finally rotating the coordinate system back to its original position;

$$I_{out} = [\Re(-\psi)] \cdot [M] \cdot [\Re(+\psi)] \cdot I_{in} \quad (2.2)$$

The Mueller matrix [M] for an ideal half-wave plate is given by;

$$[M] = \begin{pmatrix} 1 & 0 & 0 & 0 \\ 0 & 1 & 0 & 0 \\ 0 & 0 & -1 & 0 \\ 0 & 0 & 0 & -1 \end{pmatrix} . \tag{2.3}$$

The $\Re(\psi)$ is the rotation of the coordinate system through an angle ψ;

$$[\Re(\psi)] = \begin{pmatrix} 1 & 0 & 0 & 0 \\ 0 & \cos 2\psi & \sin 2\psi & 0 \\ 0 & -\sin 2\psi & \cos 2\psi & 0 \\ 0 & 0 & 0 & 1 \end{pmatrix} . \tag{2.4}$$

The last element of a polarimeter must be a polarization prism or filter. The linear polarizer is set at fixed orientation, so that the output state of polarization is constant. The matrix of a linear polarizer [P] is;

$$[P] = \frac{1}{2} \begin{pmatrix} 1 & \pm 1 & 0 & 0 \\ \pm 1 & 1 & 0 & 0 \\ 0 & 0 & 0 & 0 \\ 0 & 0 & 0 & 0 \end{pmatrix} . \tag{2.5}$$

This matrix [P] is also applied to the preceding matrix (Equation 2.2) and, therefore, from the output we can deduce the Stokes' parameters, Q, U. The final form of the light emerging can thus be represented by,

$$I_{out} = [P] \cdot [\Re(-\psi)] \cdot [M] \cdot [\Re(+\psi)] \cdot I_{in} \tag{2.6}$$

The resultant light will now depend on the chosen components. For the basic modulating component, the most likely choice is a half-wave plate retarder, since this is simplest to construct and implement as a modulator in polarimeters. The final output matrix is as follows;

$$\begin{pmatrix} I \\ Q \\ U \\ V \end{pmatrix}_{out} = \frac{1}{2} \begin{pmatrix} I \pm Q\cos 4\psi \pm U \sin 4\psi \\ I \pm Q\cos 4\psi \pm U \sin 4\psi \\ 0 \\ 0 \end{pmatrix} \tag{2.7}$$

The above equation is a general form of a double beam polarimeter (from equation 2.5) whereby + refers to Beam 1 (Ordinary ray) and – refers to Beam 2 (Extraordinary ray). In terms of measured intensity signal the final expression is;

$$I(\psi) = \frac{1}{2}(I \pm Q\cos 4\psi \pm U \sin 4\psi) \tag{2.8}$$

Although there are only two unknowns of polarimetric interest in the above equation, at least three measurements must be made in order to eliminate the instrumental response to unpolarized light (see Chapter 3 and 4). Various possible values of ψ can be combined to deduce the Q and U parameters. In fact, for the work presented in this thesis two methods have been tried, viz., Fessenkov's (1935) method and the Pickering (1874) method.

2.3 Photoelectric Polarimetry

Since the discovery of interstellar polarization by (Hiltner, 1949) and (Hall, 1949), photomultipliers have been dominant in polarimetric instrumentation. As they use the photoelectric effect, there is no detector threshold (it can detect a single photon) and it is perfectly linear up to large fluxes $\sim 10^5$ photons s^{-1}. The first planetary photoelectric polarimetry was performed by Lyot (1948ab). This was followed by Öhman (1949) who described several devices for astronomical photoelectric polarimetry. During the early 1950s, the photoelectric techniques reached a point where the design of a very sensitive polarimeter could be applied to wide range of sources.

There are many designs for a photoelectric polarimeters both single and double channel. These can generally be divided into discrete or continuous systems. By this, it is meant

Accuracy (from Photon–Statistics)	Magnitude (60-minute integration)
0.01%	7
0.1%	12
0.5%	16

Table 2.3: Limiting magnitude with a 1-meter telescope with a V filter according to the achievable polarimetric accuracy.

that the polarimetric element is moved to a fixed positions in steps or rotated continuously, respectively again, the former case requires brightness measurements to be made at the chosen angles of the modulator, where as for the continuously rotating modulator, the signal processor corresponds more to being a phase sensitive detection system.

Photoelectric devices have been used in stellar polarimetry for a number of years (see Serkowski, 1974a). Some of these stellar polarimeters (in broad-band) are capable of an accuracy of $\pm 0.01\%$, when used with care and may be used with filters to define wavelength passbands. Highest polarimetric precision was achieved in solar work where Dollfus (1953) obtained an accuracy of 0.001%. Table 2.3 lists typical magnitude limits (from photon statistics) for different values of desired accuracy with a photomultiplier tube (see Breger (1986)).

A major problem with photomultipliers is that they are single element detectors. Consequently, spectropolarimetry can only be achieved by sequential observations. For example, if we wish to obtain a resolution of say, 10Å, with 1000Å coverage then, obviously, measurements must be conducted one hundred times with sequential movement of the passband. Similarly, measuring the polarization of a spatially resolved object such as a planet, comet, nebulae or galaxy by sequentially placing a small aperture at one point after another is obviously a slow process, and one which is prone to positional errors.

There are several different methods with which the output from a photomultipliers can be measured, but the most common technique is the pulse–counting (or photon–counting)

method (the other method being DC amplification, see Clarke, 1965). In this method the individual electron avalanches (pulses) arriving at the anode are amplified and converted to a voltage pulses which can be counted electronically. The number of pulses counted in a given time interval is a measure of the number of photons that strike the photocathode in the same time interval. The only drawback for this technique is that at high light levels, pulse overlap occurs and the recorded signal becomes non-linear to the brightness level.

2.3.1 Effect of Dead–Time in Photoelectric Polarimetry

Most modern photoelectric polarimeters now use a photon–counting technique (this also applies to photometry). The technique's greatest drawback is its inability to handle high counting rates when measuring bright sources. Pulse overlap may quantitatively be referred to as the dead-time problem, and is generally controlled by components in the amplifier and counting circuits. The overall electronic circuits of the amplifier units and photomultiplier, which have a finite ability to resolve closely spaced pluses. For a count to be triggered in a detector, pulses must be separated by at least τ seconds, where τ is the dead-time constant, otherwise two close pluses will be counted as one pulse. Consequently, when performing accurate photometry it becomes essential to determine the value of the dead-time for the electronic system and allow for it in the data reduction.

The dead-time correction must be determined individually for each polarimeter. If correction is not removed, then the polarization values will be biased and therefore meaningless. Although such corrections have been mentioned (e.g. see Hsu and Breger, 1982) in relation to the accuracy of polarimetry, it is generally not appreciated how lack of attention to them can introduce systematic errors, significantly larger than the standard error of measurement. There are several techniques allowing the dead-time for a particular photometer (polarimeter) to be measured (see Poretti, 1992, Cooper and Walker, 1989 and Fernie, 1976). A recent paper by Clarke et al. (1996) describes how polarimetry itself can be used to ascertain the dead-time for a photon counting system.

Once τ is known, correction is usually made by using a formula in which the observed counts, n, are converted to the true counts, N;

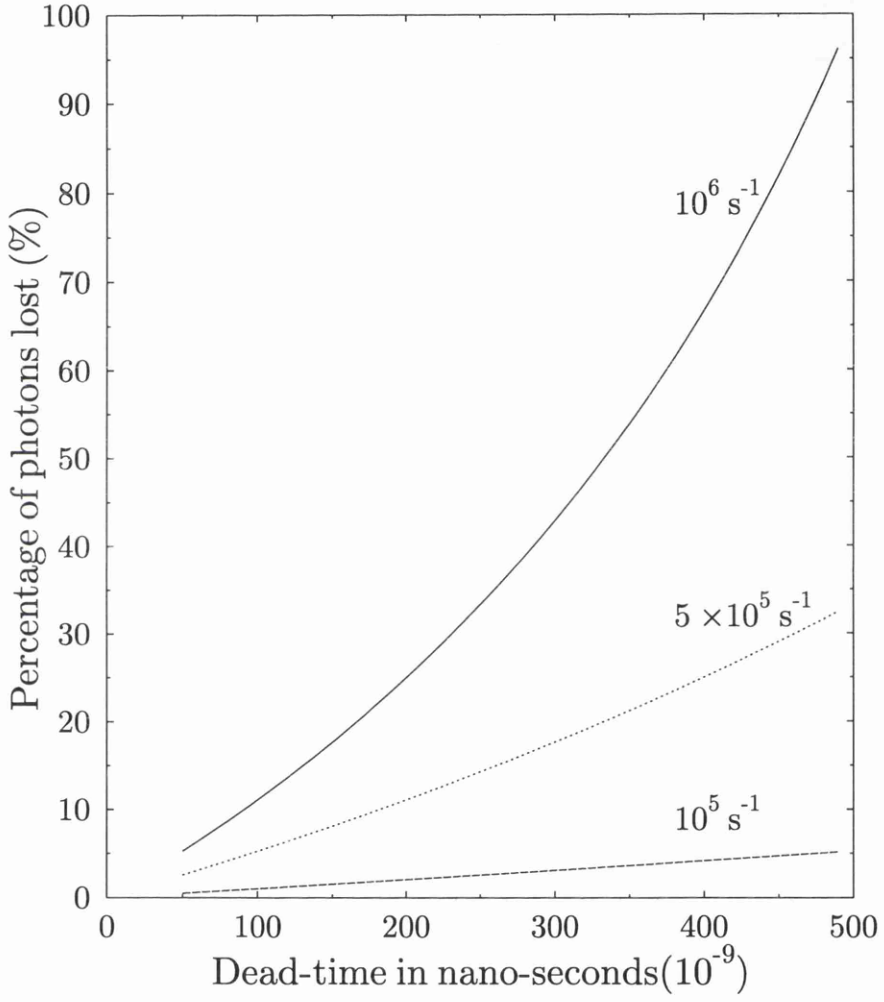

Figure 2.2: Plot of percentage of photons lost against the varying dead-time (in nano-seconds) at three count rates of $10^5 s^{-1}$, $5 \times 10^5 s^{-1}$ and $10^6 s^{-1}$.

$$n = N\, e^{-\tau N} \quad , \tag{2.9}$$

The above formula is usually represented by using an approximation for the term $e^{-\tau N}$ with a McLaurin expansion which stops at the first order, obtaining

$$n = N\,(1 - N\tau) \tag{2.10}$$

The above equation is rather cumbersome to apply and thus a further approximation is usually made where $(1 - N\tau)$ is replaced by $(1 - n\tau)$. The final equation is thus given by;

$$N = \frac{n}{(1 - n\tau)} \tag{2.11}$$

The above equation is only applicable to low count rates and would be invalid at higher counts. However, the best method is to determine N by applying an iteration to Equation 2.10.

Generally, the effects of dead-time are severe at high count rates and this is illustrated in Figure 2.2. The figure shows the proportion of counts lost (in percentage) with varying dead-time at different count rates. It is seen that at high count rates ($10^6 s^{-1}$) the percentage of losses are large. From figure 2.2, if we assume a dead-time of 100 nanoseconds, then at count rate of $10^6 s^{-1}$, $5 \times 10^5 s^{-1}$ and $10^5 s^{-1}$ the losses are 11.1%, 5.3% and 1% respectively.

Hsu and Breger (1982) have stated that the effect of dead-time on the observed value of polarization is large for bright stars. They derived an equation where the observed polarization is converted into the true polarization. The form of the equation is of $P_{true} = P_{obs}(1 + \tau C)$, where C is the count rate. Thus correction can be made if τ is known. However if τ is itself uncertain, then this is carried through into the correction and the systematic error introduced may still be large. If, for example, a bright star is measured at a count rate of $10^6\ s^{-1}$ and P_{obs} of 3%, any uncertainty of $\approx$100 nanosecond in dead-time value will cause an error in P_{true} of 0.03%. However, in most polarimeters the real

quantities measured are the Stokes' parameters, q and u. The analysis of the problem is couched in terms of Stokes' parameters rather than the polarization values.

To assess quantitatively the effects of dead-time on polarimetry, consider that the true value of a Stokes' parameter q_t is determined from true photon counting rates N_1, N_2 corresponding to the strengths of orthogonal polarizations so that,

$$q_t = \frac{N_1 - N_2}{N_1 + N_2} \,. \tag{2.12}$$

The counting rates are, however, affected by dead-time losses such that the directly measured parameter, q_m, is determined from;

$$q_m = \frac{n_1 - n_2}{n_1 + n_2} \,, \tag{2.13}$$

where n_1, n_2 are the recorded photon count rates. For any true counting rate, N, the observed rate, n, will depend on the dead-time constant, τ, and by using equation 2.10, it may be readily demonstrated that

$$q_m = \frac{N_1 - N_2 - \tau(N_1^2 - N_2^2)}{N_1 + N_2 - \tau(N_1^2 + N_2^2)} \tag{2.14}$$

By rearranging equation 2.10 so that N_2 is expressed as

$$N_2 = \frac{N_1(1 - q_t)}{(1 + q_t)} \tag{2.15}$$

Equation 2.12 can be explored for combinations of N_1 and q_t, according to the value of τ for the equipment. Figure 2.2 displays the systematic error $\varepsilon = q_t - q_m$ for true photon count rates of 10^5 s^{-1}, 5×10^5 s^{-1} and 10^6 s^{-1} operating with a value of τ = 70ns, typical of a good photon counting system as used by Hsu and Breger (1982). It is evident from Figure 2.3 that having high photon (e.g. 10^6) counts, the accurate correction of the dead-time becomes very important.

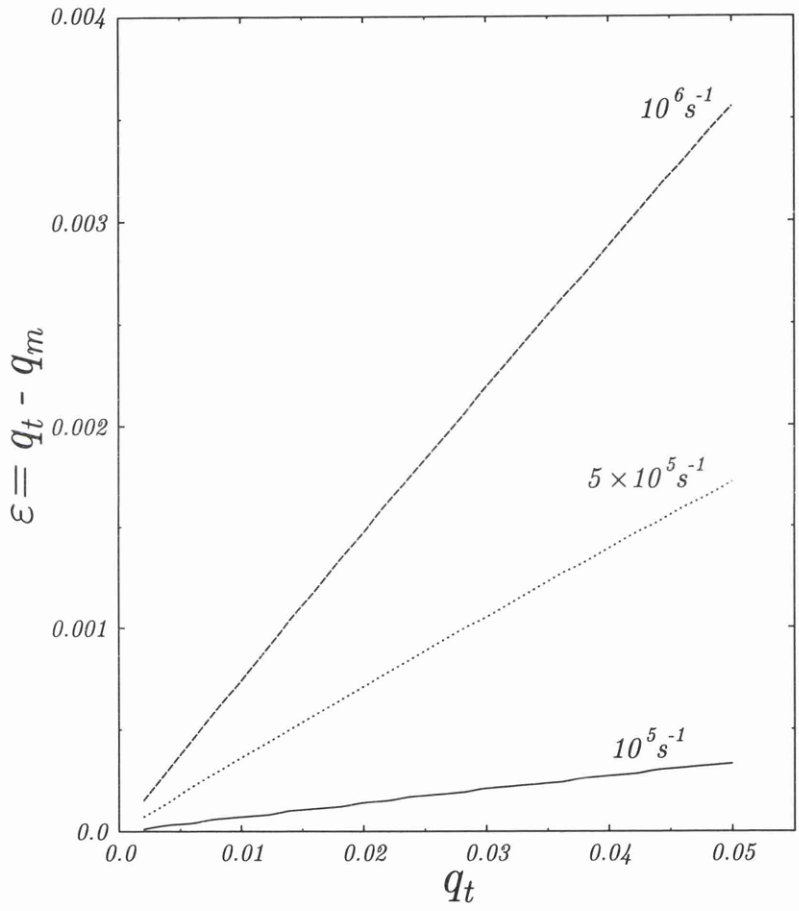

Figure 2.3: Plot of the systematic error ε, caused by not applying dead–time correction for three different photon counting rates as labelled against the underlying true Stokes' parameter q_t

Similar formulae are applicable to the u parameter and the overall effect on p could be determined according to the relative contributions of q_t and u_t. For the simple case with $q_t > 0.01$ and $u_t = 0$ (equivalent to a polarization of 1%), the systematic errors are substantial. It is also apparent that any large systematic error in determination of the dead-time (τ) will result in further complicating the situation.

A good example of the problem associated with dead-time on polarimetry can be illustrated by analysing the work of Bastien et al. (1988). His work was centred around observing polarization standard stars. Most of the stars observed by Bastien et al. (1988) where sufficiently bright to achieve very high photon counts. In fact he used a variable neutral density filter to reduce the photon counting rate.

The data were scrutinized to see, if the dead-time correction was adequately applied. For the levels of p associated with a supposed polarization standard star such as o Sco (p $\sim$ 0.04 or 4%) it can be seen from Figure 2.3 just how sensitive is the systematic error to the count rate; for count rates between 10^5 s^{-1} and 10^6 s^{-1} the systematic error changes from $\sim$ 0.0002 to $\sim$ 0.0030, while the typical quoted standard errors found in the catalogue of measurements of Bastien et al. (1988) range from $\pm$ 0.00005 to $\pm$ 0.00019 with the average error being $\sim \pm$ 0.00009, these based on accumulated photon counts numbers. As the photon counting rate is sensitive to night-to-night variations in transparency, the zenith distance and arbitrary adjustment of the neutral density filter, allowance for dead-time is difficult to apply. The data obtained by Bastien et al. (1988) came from different telescopes with different polarimeters; deeper investigation proved that for some measurements dead-time correction had been attempted, whereas for others it had been neglected.

It was demonstrated by Clarke and Naghizadeh-Khouei (1994) that the magnitude of the effect due to inadequate allowance for τ would readily account for the scale of the departures of Cumulative Frequency Distribution of P_{ui} from that of the Rayleigh distribution (see Clarke et al., 1993). It is perhaps significant that the magnitude of the systematic errors is very sensitive to the underlying value of p as well as dependent on the stellar brightness, for example, the star HD84810(L Car) with its relatively low level of polarization is noted to behave best in terms of polarization constancy.

Increasing or decreasing the high voltage supply to the photomultiplier may also influence the value of τ, only some workers control signal counts by adjusting the EHT, effects on the dead-time constant have not been investigated. Also, if the dead-time has not been determined accurately we may over/under-estimate the noise level. Although the neglect of dead-time corrections would seem to invalidate any meaningful discussion on the observed polarization, p, its effect on the values of position angle involving ratios $\frac{u}{q}$ is less significant.

2.4 CCD Polarimetry and Spectropolarimetry

CCDs with high quantum efficiency, low read-out noise and small pixel size (10 - 22 μ) are beginning to dominate an ever increasing variety of imaging and spectroscopic studies. There are many advantages (and some disadvantages relative to a single element detector such as photomultiplier) of using a CCD array (see Table 2.1). Optical CCD technology now allows both 2D polarimetry and spectropolarimetry observations to be made.

It would be beyond the scope of this thesis to discuss the techniques of CCDs and the way in which they operate. Basically, a CCD is an array of MOS (Metal-Oxide-Semiconductor) capacitors which can collect photons and store charge packets by absorption of incident light, each element being regarded as a pixel.

There are at present two techniques employed in CCD polarimetry. The first technique is the simplest to use, where several separate image frames (usually four) are taken and read out for different states of the modulator. These images are then combined to produce polarization maps and spectra. Such a technique is developed by the author and will be described in Chapters 3 and 4. The second technique uses the 3-phase structure of the CCD which permits bi-directional charge transfer, called on-chip charge storage. This allows the stored charge to be moved about on the chip without actually reading it out until the end of the exposure. These have been successfully used by Tyson and Lee (1981), Scarrott et al. (1983) and Clemens and Leach (1987) and is currently the most used technique. Another scheme is called differential imaging and was invented by Stockman (1982). Figure 2.4 illustrates the technique used by Stockman (1982). In this way one

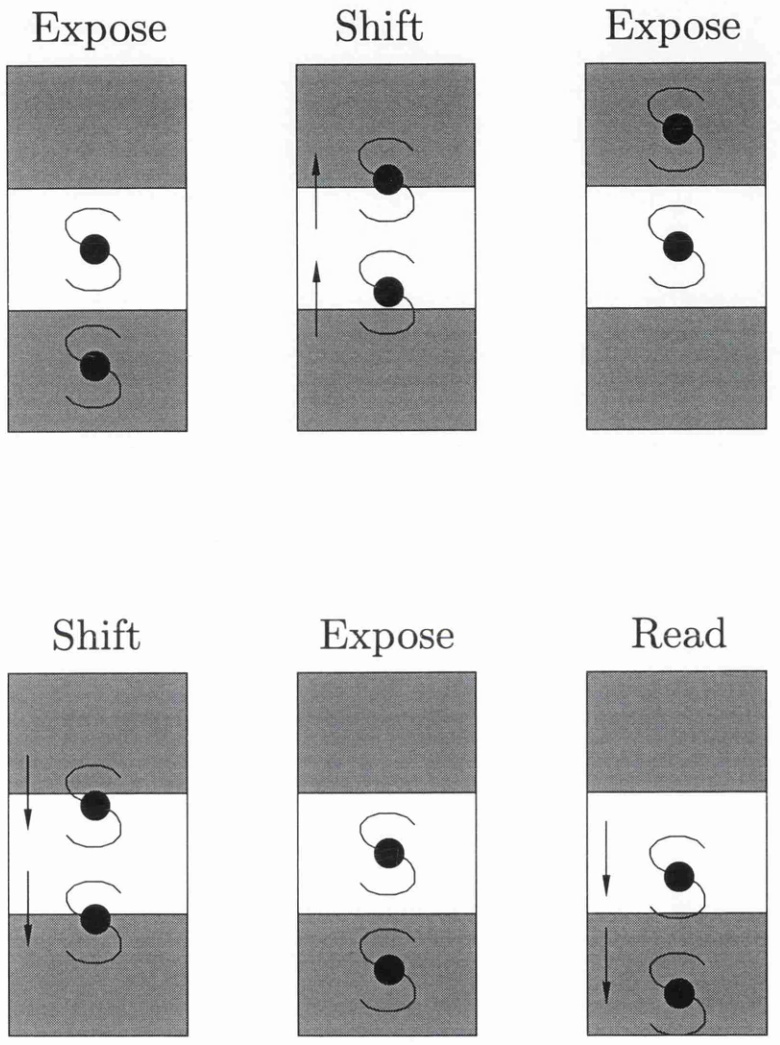

Figure 2.4: The Stockman method of differential imaging using on-chip charge storage. Each rectangle represents the CCD in the middle of an exposure state or a vertical transfer state. Shaded areas are masked pixels (photosites). After a number of shifts ($\approx$ 20) and expose cycles, the CCD is shuttered and read in the normal way. The two images represented in this figure may be described by either states of polarization; e.g. $\updownarrow$ and $\leftrightarrow$.

can chop between two polarization states and build up the signal. Many variations to Stockman's method are possible and these have been adopted by McLean et al. (1981), Boyer et al. (1981), Stenflo and Povel (1985) and Povel et al. (1990). The method is that a fast polarimetric modulation can be adopted (see Povel et al., 1990) to help defeat atmospheric generated noises. Unfortunately, they are more vunerable to charge-transfer effects that limit the accuracy of their measurements and also the whole of the CCD chip cannot be used effectively. A list of recent advances in polarimetric precision can be found in Appendix A.

2.5 Polarimetric precision

One question which one might ask is 'Do we need higher polarimetric accuracies?' The answer is an emphatic **"Yes"** (see Chapter 1). This is simply because many astronomical objects have small polarization values of 1% or less, and these in turn may exhibit small amount of variability.

Theoretically, precision of p on the order of $\pm 0.001\%$ should be easy to achieve for bright stars. It is therefore essential to find an observing technique which would improve the present achievable precision. Polarization can be measured with high precision, simply by maximizing the photon collection and minimizing the sources of noise. The degree of precision is then indicated by the repeatability of measurement on a given source. The absolute accuracy, however, is much harder to estimate and to control because of systematic errors in the instrument.

The origins of noise are many, and these can be divided into three different basic categories;

- Photon noise due to the source (e.g. a star).
- Atmospheric variability problem including scintillation noise and sky background subtraction.
- Instrumental noise (e.g. dead-time).

The first noise represents an absolute fundamental limit to accuracy. The other sources of errors such as scintillation can be removed or minimized by instrumental design and by implementing a suitable diagnostic routine. For example, scintillation and seeing are the main sources of atmospheric noise. Since air is not birefringent, scintillation is the same for both perpendicular polarized component of light from an astronomical object.

The precision of polarimetric measurements (like photometry) are theoretically governed by quantum noise, i.e. by randomness in the number of photons arriving at the telescope. In order to work out how one can improve photometric/polarimetric accuracies, it is important to understand how the total number of photons counted will limit the maximum possible accuracy. One has to be aware that there is a statistical rule (Poisson distribution) which applies to all counting processes. This can be expressed mathematically as,

$$P(N_i) = \frac{(\overline{N})^{N_i}\ e^{-(\overline{N})}}{N_i\ !}\quad , \tag{2.16}$$

$P(N_i)$ is the probability of observing a count N_i and $\overline{N}$ is the mean of the counts from all measurements. For large values of N the Poissonian becomes a Normal distribution to all intents and purposes with the property that the standard deviation $\sigma = \pm\sqrt{\overline{N}}$.

The Poissonian statistic is the basic noise source, of an irreducible nature which applies to the number of detected counts (photons). If, for example, repeated photometric observations are made of a non-variable star with μ as the mean number of detected photons counts per observations, the expected root mean square(rms) noise level is $\mu^{1/2}$. Now, we can assume the fluctuations over the individual measures (repeated M times), x_i, to be:

$$rms(x_i) = \sqrt{\frac{1}{M}\sum_{i=1}^{M}(x_i - \mu)^2} \tag{2.17}$$

It can be illustrated that at a signal level of $\mu = 10000$ detected photons the associated poisson fluctuations are $\mu^{1/2} = 100$; for this case the signal-to-noise, S/N, is $\frac{\mu}{\mu^{1/2}} = \frac{10000}{100}$ $= 100$. No amount of clever reduction can result in a final photometric precision being better than the Poisson limit. Therefore, in theory the more photons one detects, the

better accuracy is attainable assuming perfect equipment.

The Stokes' parameters Q, U and V are directly deducible from the signals produced by polarimeters. In fact, Q, U, and V can be given by the difference of a pair of intensities corresponding to two appropriate settings of a retarder (e.g. a $\lambda/2$ plate). For instance,

$$Q = \frac{I_{\updownarrow} - I_{\leftrightarrow}}{I_{\updownarrow} + I_{\leftrightarrow}}\,, \tag{2.18}$$

where $I_{\updownarrow}$ and $I_{\leftrightarrow}$ are the intensity signals at the two position of the retarder allowing transmission of the polarization states corresponding to $\updownarrow$ and $\leftrightarrow$. For polarization $I_{\updownarrow} = n_{\updownarrow}$ and $I_{\leftrightarrow} = n_{\leftrightarrow}$ converts the signal to photon counts ($n_{\updownarrow}$, $n_{\leftrightarrow}$).

The modified form of Equation 2.18 allows an error analysis to be undertaken - by differentiation,

$$\frac{\delta q}{\delta n_{\updownarrow}} = \frac{2n_{\leftrightarrow}}{(n_{\updownarrow} + n_{\leftrightarrow})^2} \qquad \text{and} \qquad \frac{\delta q}{\delta n_{\leftrightarrow}} = \frac{-2n_{\updownarrow}}{(n_{\updownarrow} + n_{\leftrightarrow})^2} \tag{2.19}$$

The variance of q is then given by,

$$(\Delta q)^2 = \left(\frac{\delta q}{\delta n_{\updownarrow}}\right)^2 (\Delta n_{\updownarrow})^2 + \left(\frac{\delta q}{\delta n_{\leftrightarrow}}\right)^2 (\Delta n_{\leftrightarrow})^2 \tag{2.20}$$

with $\Delta n_{\updownarrow} = \sqrt{n_{\updownarrow}}$ and $\Delta n_{\leftrightarrow} = \sqrt{n_{\leftrightarrow}}$, therefore

$$(\Delta q)^2 = \frac{4n_{\updownarrow}n_{\leftrightarrow}}{(n_{\updownarrow} + n_{\leftrightarrow})^3}. \tag{2.21}$$

A double beam polarimeter simultaneously measures orthogonal polarization intensities. Therefore defining the photon count as $n = n_{\updownarrow} + n_{\leftrightarrow}$ and at low p with $n_{\updownarrow} = n_{\leftrightarrow}$ yields

$$\sigma_q = \sqrt{\frac{1}{n}} \tag{2.22}$$

for a double beam polarimeter. Similar treatment may be applied to the u Stokes parameter with

$$\sigma_u = \sqrt{\frac{1}{n}}. \tag{2.23}$$

Consequently as the number of detected photons increases the polarimetric precision will improve as illustrated in Figure 2.5. Effects of photon noise may be only be reduced by increasing the integration time of an observation.

It is readily apparent from our second definition that we can improve the accuracies by $\sqrt{2}$ in our precision if $I_{\updownarrow}$ and $I_{\leftrightarrow}$ are measured simultaneously. From the above analysis it is seen, that the only method with which one can reduce the errors resulting from the photon statistics, is to collect more photons by using a large telescope or increase the integration times. The former is demonstrated in solar polarimetry where one can count large number of photons (since the Sun is the brightest star in the sky) where polarization noise as low as 0.01% to 0.001% can be achieved (see Baur, 1981). Clarke (1991) has reported that from studies of the polarization of the whole Solar disk a precision of the order of 0.003% was achieved from the internal distribution of the repeated measurements. To achieve $\Delta p \approx \pm 0.0001$ (0.01%), an integration time of 1 hour at the maximum photon counting rate of $10^5 s^{-1}$ is required. For increased counting rates, accurate account of counting losses needs to be made (see Section 2.3.1). Inordinate integration times are required to achieve ultimate precision.

When dealing with bright sources, if one is limited by the photon counting system of the photomultipliers, then one needs to find an alternative detector. We can consider CCDs as photon counting devices but in a different sense as regard of the real time system such as the photomultipliers. CCDs do provide a direct estimate of the number of photons counted (see Chapter 3, Section 3.2.1).

If CCDs are considered as a solution to the bright star problem then one must investigate their properties. One problem with CCDs is that the output signal is expressed as a grey level scale with discrete values in photoelectron numbers. The total signal in electrons (saturation limit) can be related by,

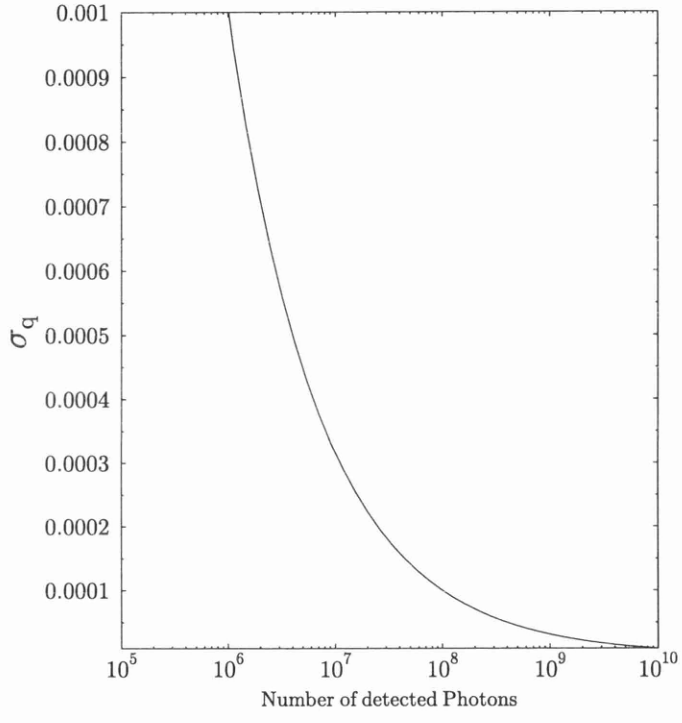

Figure 2.5: The expected polarimetric precision as a function of the number of detected photons.

$$S_{max} = \mathcal{Q}\ 2^{N_b}\ , \tag{2.24}$$

At saturation the grey level scale is given by, 2^{N_b}, where N_b is the number of bits associated with the analogue to digital (A–D) converter within the CCD system. N_b ranges from 8 to 16 bits. Thus, the maxium grey level is 255 to 65535 according to the value of N_b. It is obvious that better differences in terms of assessing photon counts is achieved using chips with larger values of N_b

One now needs to look at the full-well capacity of the CCD. In modern CCDs the full-well capacity is usually $> 5 \times 10^5$ electrons (some as high as 10^6 electrons). However, the A–D converter cannot output a signal that is greater than 65535 (16 bit). Thus, to make full use of the dynamic range of the gain factor($\mathcal{Q}$), one should choose an appropriate setting (this is not be possible in some commercial CCDs) according to a type of observation one is making.

One way to take a full advantage of a two dimensional detectors such as CCDs, is to illuminate as many pixels of the CCD chip as possible (e.g. making the CCD act like a collection of light buckets). If we assume theoretically that $100 \times 100 = 10^4$ pixels are illuminated, with a full-well capacity of 10^5, one can see that the total number of photons counted is $10^4 \times 10^5 = 10^9$. From the Equation 2.9 we can see that the precision on the Stokes' parameters would increase to $\sigma \approx \pm 0.00003$ (0.003%) all within a single measurement. This is an improvement of $\approx$5 times on the present accuracy available via the photomultipliers. Such a scheme has been explored and will be described in Chapter 3.

Chapter 3

An Aperture Imaging Polarimeter

3.1 Introduction

This chapter describes the calibration and construction of a double-beam CCD stellar polarimeter. There were two main objectives set in its design and investigation of its potential. The first was to pursue the possibility of improving the accuracy of the polarimetric data relative to standard instruments and the second was to investigate the instrumental polarization emanating from the telescope optics. The premise behind the former notion was shown in Chapter 2, where it was seen that it may be possible to push the polarimetric accuracy beyond the existing polarimeters capability of 0.01% with new solid state detectors such as CCDs. The latter notion was centred around the fact that all polarimeters suffer from instrumental polarization. Consequently, there is a need to reduce or eliminate this unwanted distortion and potential noise source.

Previous CCD imaging polarimetry has been confined to low precision work. It has mostly been applied to obtaining 2D area polarization maps of faint stars or nebulosities which usually possess a large percentage of polarization, in some cases in excess of 50% (see Meisenheimer and Röser, 1986, Dekker and D'Odorico, 1986, Fosbury et al., 1989, Fosbury et al., 1993 and Scarrott et al., 1983). The polarimetric uncertainties associated with these observations are usually large, typically 0.4% to 2% per pixel. The main reason for this

large uncertainty is that the polarization values for the individual CCD pixels depend on the number of photons accumulated during the exposure. A typical pixel may hold $\geq 500000e^-$ before saturation. This translates into a uncertainty in polarization of 0.15%.

The accuracy may be further degraded by observing faint stars with long integration times with the necessity to subtract the background of the detector or of the sky which may itself have a polarized component. However, for bright stars the sky background is unimportant. Even if the stellar image covers a few pixels (say 5 to 10) the improvement on the total photon count will not be large enough to produce the required uncertainty on the detection of low level polarization variations.

To improve the possible polarimetric detectivity a double-beam polarimeter was designed such that the light from a single star was spread onto as many CCD pixels as possible, and approaching close to saturation so reducing the overall photon noise. The most suitable technique was to image the telescope aperture (de-focusing the star image) onto the CCD chip. With this method it may be possible to collect a sufficient number of photons to reach the desired photometric noise level in any one frame, and if combined, it may produce a high polarimetric precision. This type of technique is already being applied to photometry of bright stars, primarily to avoid saturating the CCD with added advantage of increasing number of photons detected (see Kjeldsen and Frandsen, 1992 and Baldiali et al., 1996). De-focusing may also reveal some of the instrumental polarization effects at different patches of the telescope mirror. The reader may have concern about throwing away the advantages of a 2D detector by limiting its use so that;

- only one single star at a time can be measured.
- area imaging polarimetry with spatial resolution is not achieved.

However, the system allows the possibility of accurate bright star polarimetry with short integration times. This would be prohibited by dead-time losses in a conventional photon counting instrument.

The real precision that most polarimeters achieve depends also on the ability of removing any instrumental polarization. To prevent systematic errors, the instrumental polarization

must be known better than the accuracy required of the polarimetric measurements, so that the observed polarization can be corrected. This parasitic effect must always be removed so that astrophysical interpretations of the polarimetric data are not distorted. The instrumental polarization produced by a telescope is usually described by a single representative Mueller matrix which relates the Stokes' parameters to the incoming and outgoing beams (see Miller, 1963). However, if precision of say 10^{-4} or better is pursued then a single Mueller matrix description would not be appropriate because of seeing effects. An in-depth theoretical description of instrumental polarization is given by Sánchez-Almeida et al. (1991) and Sánchez-Almeida and Martinez-Pillet (1992) at the focal plane of several different telescopes.

In a schematic picture, a telescope collects all the rays coming from the same direction and concentrates them into a small image region in the focal plane. The light from the stars arrive at Earth as planer wavefronts. The inhomogenities in the atmosphere and associated varying index of refraction distorts the plane wavefronts, thus, crinkling the plane wave. These distorted wavefronts will then produce fluctuating instrumental polarization when reflected off various parts of telescope mirror. Consequently, there are two important effects that should be considered when modelling the instrumental polarization.

- Different rays suffer different instrumental polarization in the path through the system.
- Different rays contribute to the polarimetric signal so the net instrumental polarization corresponds to none of the individual rays, but to their summation. Since the resulting polarization depends on the phase relationship between rays, they have to be added up coherently.

There are several considerations which must investigated before an experimental arrangment as above is explored. In considering the potential, it is of utmost importance to have knowledge of the numbers of photons incident on the CCD chip. For statistical studies of noise levels etc., the CCD detector employed must be calibrated so that the output digital data can be converted to photon counts.

3.2 CCD Detector and its Calibration

The CCD detector used was a SBIG (Santa Barbara Instrument Group) ST-6 with 375 × 242 pixels. The pixel size is $23\mu m \times 27\mu m$ and the total area $8.6mm \times 6.5mm$, for further details consult the Table 3.1.

The precise calibration of the CCD signals is important before any interpretation in absolute terms can be carried out. There are two main calibrations which must be performed in order to ascertain a) readout noise (system noise), and, b) the conversion factor from the output digital number (ADUs) into photoelectrons (system gain). The latter part will be important in determining the number of photons striking the CCD chip. Also, ADUs cannot be used in the determination of noise levels associated with photon shot noise. With knowledge of the conversion factor signals recorded in ADUs can be converted to number of electrons and proper statistical theory associated with photon counts can be applied.

For any CCD system there are several different noise regimes which must be considered as the signal level varies (see Mackay, 1986). At the lowest light level, the readout noise will dominate. However, as the signal increases its shot noise is added in quadrature with the intrinsic readout noise. Eventually, the readout noise becomes negligible, and the signal-to-noise ratio of the measurements are in proportion to the square root of the signal in electrons. At the highest light levels, the signal-to-noise ratio will rise more slowly with signal and this is attributed to the onset of nonlinearity near saturation.

3.2.1 Conversion of Analog to Digital Unit (ADU) into Electrons

The strength of CCD images are recorded initially in digital numbers (ADU) with values depending on the number of electrons or detected photons accumulated in each pixel. The ADU values are represented digitally either in 8 bit, 12 bit or 16 bit, giving dynamic ranges of 1 to 255, 4096 and 65535 units respectively. Consequently, the number of electrons represented in one ADU is unknown until the chip has been calibrated.

Parameters	Details
CCD Make	TC-241
CCD Chip Size	375(H) × 242(V)
Pixel Size	23μm by 27μm
Active Area	8.6mm by 6.5mm
No. of Amplifiers	1
Quantum Efficiency	blue 25%
	red 65%
Readout Speed	22μs per pixel
Acquisition and Display Time	20s for a full frame
Readout Noise	40e^- RMS
Gain	10e^-/ADU
Full-Well Capacity	$\sim 5 \times 10^5$ electrons

Table 3.1: The parameters of the SBIG ST-6 CCD Camera

There are several methods available to determine the system gain and system noise (see Gudehus and Hegyi, 1985 and Buil, 1991). It is desirable to perform the system gain calibration and investigate the system noise concurrently. The most powerful method is the variance method, or photon transfer scheme described by Janesick et al. (1985).

The calibration procedure is performed by using a technique outlined below:

3.2.2 Photon Transfer Technique

A transfer equation can be written in terms of the signal measured in ADU at the output of the converter, and the number of accumulated electrons as:

$$S(ADU) = \mathcal{G}N \tag{3.1}$$

where N is the signal in number of electrons and $\mathcal{G}$ is the gain of the whole amplifier expressed in ADUs per electron. The signal noise expressed in ADU is thus,

$$\sigma_s(ADU) = \mathcal{G}\sqrt{N}, \tag{3.2}$$

and the variance is

$$\sigma_s^2(ADU) = \mathcal{G}^2 N. \tag{3.3}$$

By taking the ratio of the variance to the measured signal one obtains,

$$\frac{\sigma_s^2(ADU)}{S(ADU)} = \frac{\mathcal{G}^2 N}{\mathcal{G} N} = \mathcal{G} \tag{3.4}$$

The above equation can also be expressed as,

$$\sigma_s^2(ADU) = \mathcal{G} S(ADU). \tag{3.5}$$

An expression for the *rms* system noise can be obtained by a similar argument. If the noise is equated as being due to shot noise of photoelectrons,

$$\sigma_{noise}^2 = \mathcal{G}^2 variance(N). \tag{3.6}$$

Thus,

$$\sigma_{noise}^2 = \mathcal{G}^2 N^2. \tag{3.7}$$

Providing that the shot noise and system noise are not coherent the variances add,

$$\sigma_s^2 = \mathcal{G} S(ADU) + \sigma_{noise}^2, \tag{3.8}$$

where σ_{noise}^2 is replaced by $G^2 N^2$,

$$\sigma_s^2(ADU) = \mathcal{G} S(ADU) + \mathcal{G}^2 N^2. \tag{3.9}$$

The above equation is the standard form corresponding to a straight line with the inverse of the gradient $(1/\mathcal{G})$ giving the calibration of electrons per ADU and the intercept of the line gives the it RMS noise of the system.

3.2.3 Experimental Determination of system Gain and Noise

A simple experiment was set up to obtain the conversion factor from ADUs into electrons. The ST6 CCD was illuminated by a flat illumination source. The source was connected to a well regulated power supply and a variable resistor to adjust the illumination falling onto the CCD chip.

Fifty frames were taken at each of several illumination levels, usually increasing by factor of two, with a dark frame also recorded for each level. A test area of 10 by 10 pixels on the CCD was selected for the evaluation.

More specifically the following procedure was followed:

Let $\mathcal{X}_{i,j,k}$ be the measured signal value for row i, column j and frame k, and $\mathcal{D}_{i,j}$ be the corresponding dark value. Then, if M is the number of exposures and P is the number of pixels in the sub-area, the mean signal value is given by:

$$\overline{\mathcal{X}}_{i,j} = \frac{\sum_k \mathcal{X}_{i,j,k}}{M}. \tag{3.10}$$

The pixel deviation from the mean,

$$d_{i,j,k} = \mathcal{X}_{i,j,k} - \overline{\mathcal{X}}_{i,j}. \tag{3.11}$$

The variance of the signal,

$$\sigma^2_{signal} = \frac{\sum_{i,j,k} d^2_{i,j,k}}{(M-1)P}. \tag{3.12}$$

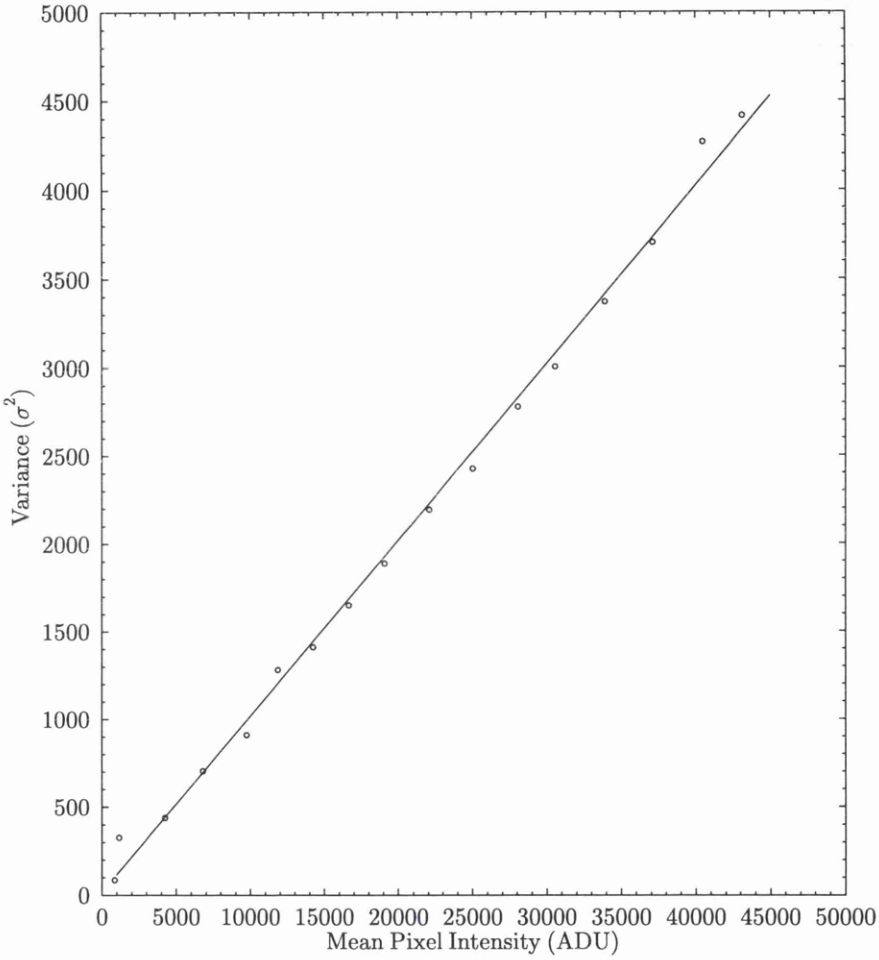

Figure 3.1: plot of the variance, $\sigma_s^2(ADU)$ against the mean signal for a selected 10 by 10 pixel area of the CCD chip. The straight line is the calculated least square fit of the data.

The mean signal level,

$$\overline{S}_{signal} = \frac{\sum_{i,j}(\overline{\mathcal{X}}_{i,j} - \mathcal{D}_{i,j})}{P}. \tag{3.13}$$

The factor (M-1) appears because it is a sample variance. This procedure was followed for each exposure level to obtain the set of signal means and variance to provide values fitting Equation 3.9 by a least square procedure. Figure 3.1 shows the transfer curve for such an experiment. From the experiment the gradient was calculated to be 0.1, so giving a value of the gain equal to 10 electrons per ADU, and from the intercept the *rms* noise of the system was 40 electrons. The maximum number of electrons given in a single pixel before saturation ≈600,000 electrons (see equation 3.1). This translates to an anticipated uncertainty of ≈0.15% in the determination of the normalized Stokes' parameters.

3.3 Techniques and Construction of the Double-beam Stellar Polarimeter

There are several approaches to designing a polarimeter. Essentially the design of a polarimeter is very much detector dependent. The CCD detector used in our system required a minimum integration time of several seconds before an image could be read, so that the fast modulation techniques were beyond consideration. The method employed was to step rotate a waveplate/analyzer with separate integration at each selected position angle

A basic double-beam system was applied with a sequence of four exposures required to calculate the Stokes' parameters Q and U. Each exposure yields two simultaneous images of orthogonal polarization. The advantage of this method is that the noise contribution from scintillation and other atmospheric variations would effect both beams equally and may be cancelled by taking ratios of the two images. Also, with this technique there is no need to perform flat-fielding.

3.3.1 Initial Set-up of the double-beam Polarimeter

The initial design was to step rotate a polarizer in front of the CCD detector. This technique requires a device such as a Calcite plate to be placed directly in front of the CCD camera in a simple mechanical arrangement.

Unfortunately, using a single Calcite plate introduces different light paths for ordinary and extraordinary beams, resulting in slightly different focal planes. This would introduce dissimilar intensity distributions of the two images and could degrade the accuracy of the relative photometry (Röser, 1981), and hence provide inaccurate polarimetry. A double Calcite plate was used consisting of two identical plates cemented together with their principal crystal axis exactly crossed (Bartl, 1959). Such a device is called a Savart plate. Placed in front of an imaging detector it produces two images containing perpendicular linear polarizations. Both images are simultaneously recorded on the CCD chip.

The Savart plate was placed in a rotatable tube controlled by gear system. For such a system, the output intensities from which the Stokes parameters are calculated, may be represented by;

$$I(\psi) = \frac{1}{2}(I \pm Q\cos 2\psi \pm U \sin 2\psi) \tag{3.14}$$

with $\pm$ sign relating to the resolved orthogonal components. Rotating the Savart plate so that ψ is set at 0° and 90°, and later at 45° and 135° gives Q and U respectively.

The optical arrangements were such that the two images were needed to be separated into ordinary ($\mathcal{O}$) and extraordinary ($\mathcal{E}$) rays on the CCD chip without the beams overlapping. Therefore, the size of the image of the telescope aperture on Savart Plate had to be calculated. In order to have clear separation between the $\mathcal{E}$ and $\mathcal{O}$ images from the Savart plate, the focal length of the collimating lens was calculated from the equation,

$$\frac{d}{\mathcal{D}} = \frac{\mathcal{F}_c}{\mathcal{F}_t}, \tag{3.15}$$

where $\mathcal{D}$ is the telescope aperture, $\mathcal{F}_c$ and $\mathcal{F}_t$ are the focal length of the desired lens and

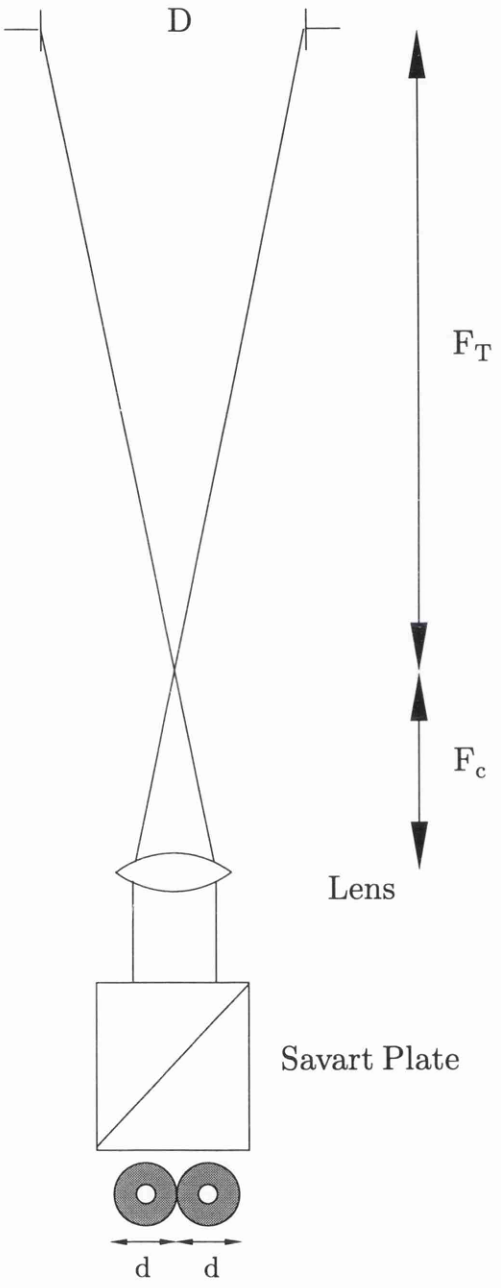

Figure 3.2: A diagram of the basic design of the double beam polarimeter.

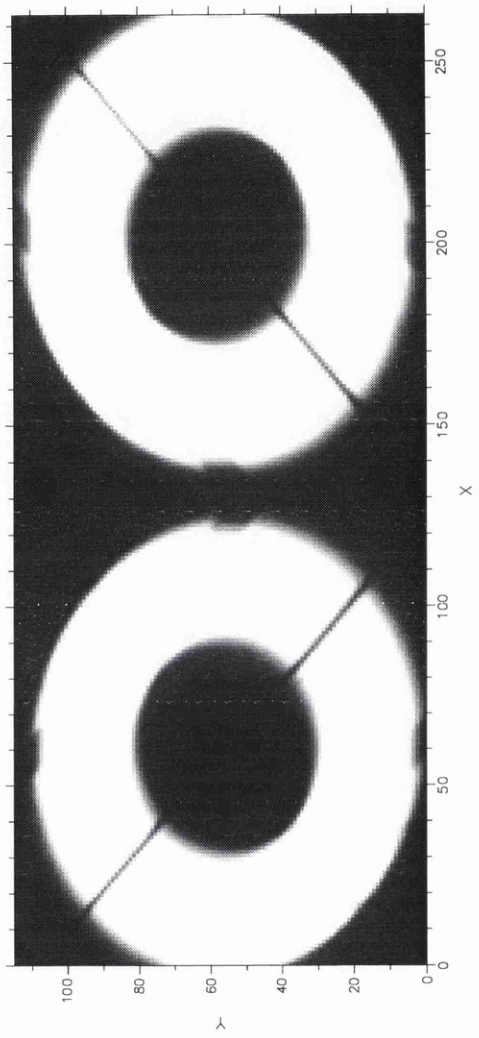

Figure 3.3: CCD images of the telescope aperture in the orthogonal polarizations obtained by the Savart plate. It can be seen that there are intensity differences in spider diffraction pattern strength. However this is solely due to the reproduction quality rather than polarization dependency.

focal length of the telescope respectively. Figure 3.2 shows the optical layout of such a system. By rearranging the above equation where,

$$d = \frac{\mathcal{D}\mathcal{F}_c}{\mathcal{F}_t} = \frac{\mathcal{F}_c}{8}, \tag{3.16}$$

the telescope aperture($\mathcal{D}$) being of 510mm with a beam of $f/8$, hence, the focal length of the telescope $\mathcal{F}_t$ is calculated to be 4080mm. The focal length ($\mathcal{F}_c$) of the collimating lens is derived from,

$$\mathcal{F}_c = 8 \cdot d \tag{3.17}$$

The available Savart plate gave a 3mm separation between ordinary ($\mathcal{O}$) and extraordinary ($\mathcal{E}$) rays. It is assumed that, [Image size] $\equiv$ [Beam separation by the Savart plate], hence, d $\leq$ 3mm to produce a clear separation between the $\mathcal{O}$ and $\mathcal{E}$. Consequently, the focal length of the collimating lens need to be $\leq$ 25mm.

A polarimeter was built with the above configuration and was tested on the telescope. A lens of 25mm focal length was used to achieve the separation. These two orthogonal images are shown in Figure 3.3. However, a severe problem was encountered as the Savart plate could not be aligned perfectly with the optical axis of the instrument. Consequently, the image wandered over the CCD chip when the Savart plate was step rotated. Several attempts were made to correct this, but unfortunately the problem stemmed from the factory fitted cylindrical metallic housing in which the Savart plate was located and this could not be removed. It was evident that the optical axis of the factory fitted cylindrical housing had not been aligned perfectly with the Savart plate.

The above method was consequently abandoned in favour of using a rotating half-wave plate with the Savart plate at a fixed position.

3.3.2 Final design of the Double-beam Stellar polarimeter with a rotating Half-wave plate

A new version of the double-beam polarimeter was designed with a rotatable half-wave plate. Like its predecessor it also employs a Savart plate. Figure 3.4 shows the final design of the instrument.

Due to the introduction of the rotating half-wave plate, the whole optical arrangement had to be redesigned. The lens system as described in section 3.3.1 could not be used because the rotatable half-wave plate gear mechanism could not be placed in between the diaphragm and the 25mm lens. Any increases in the focal length of the lens would allow the ordinary ($\mathcal{O}$) and extraordinary ($\mathcal{E}$) beams to overlap. However, this could not be avoided and a lens of 75mm focal length was used for this purpose. Figure 3.5 show the two overlapped images.

3.3.3 Instrumental Set-up (optical and mechanical)

As a general rule, the polarimetric element, the half-wave plate, was placed closest to the Cassegrain focus. This prevents and minimizes the instrumental polarization and also reduces the image wobble due to prismatic effects in the rotating half-wave plate (see Serkowski, 1974b).

In this prototype instrument there was no wavelength discrimination, the observations being carried out in white stellar light.

Previewer

The previewer system consisted of a Bronika camera body with a flip mirror type. The mirror was wound manually from outside the polarimeter box to allow previewing. Thereafter the mirror was flipped electronically, allowing the light to pass into the polarimeter.

The light from the camera mirror was directed to a lens system and a cross-hair eyepiece.

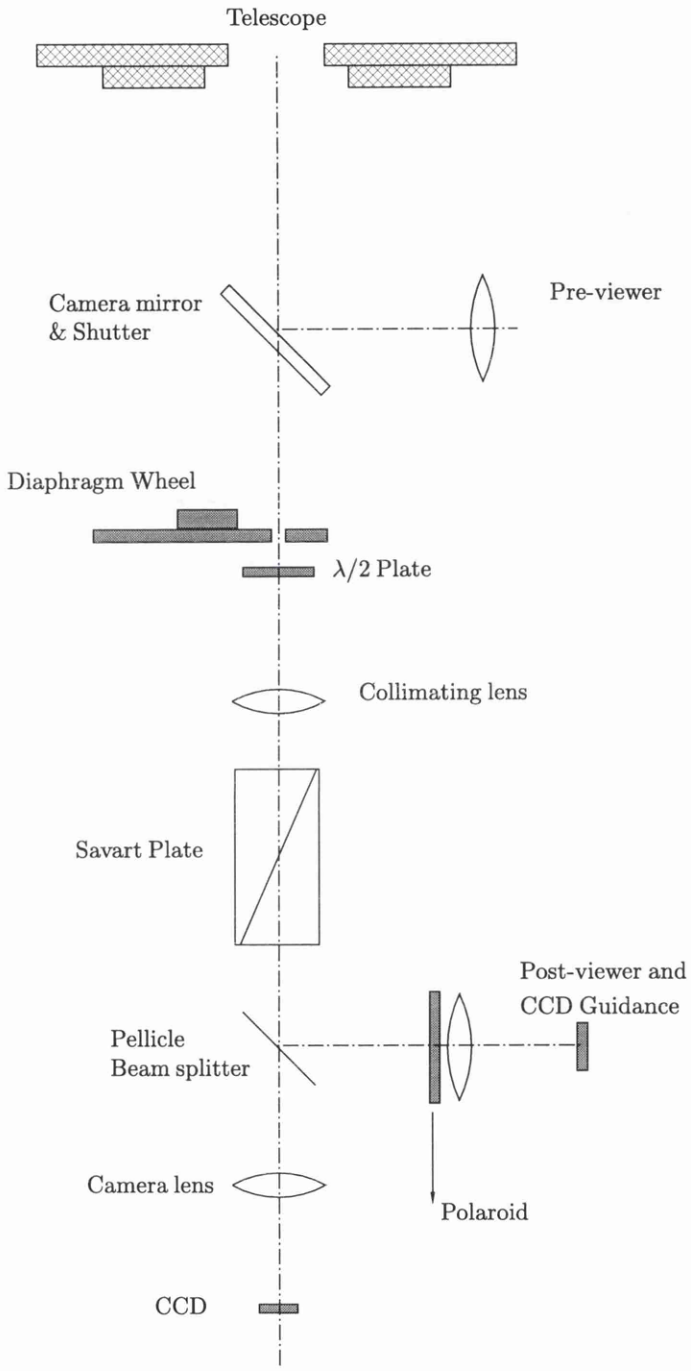

Figure 3.4: Schematic diagram of the Stellar imaging polarimeter with a rotatable Half-wave plate.

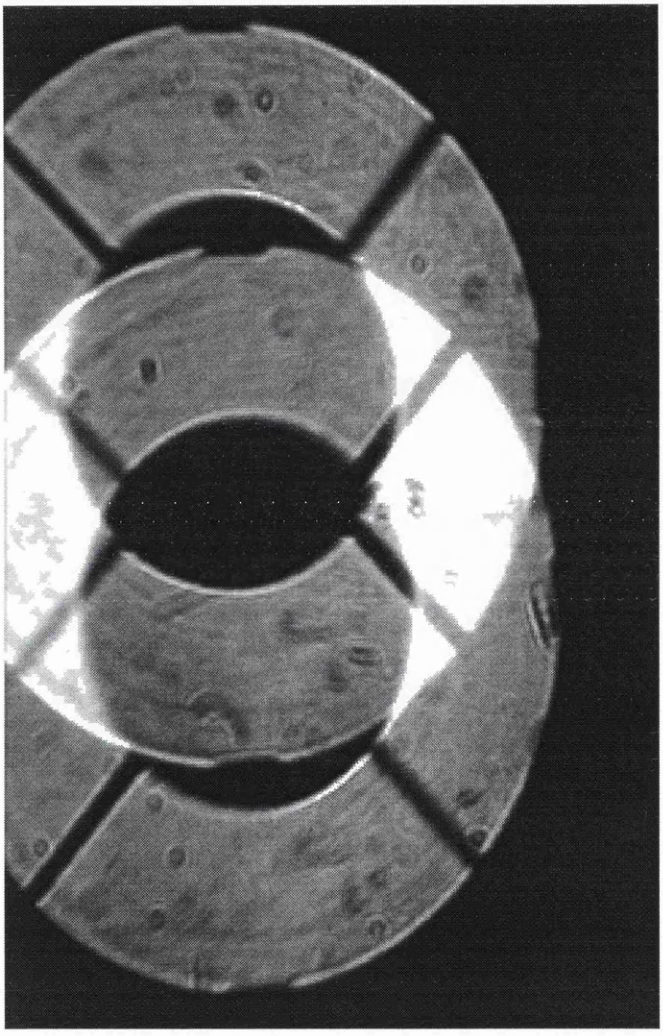

Figure 3.5: Overlapped CCD images of the telescope aperture with the orthogonal polarizations.

The cross-hair of the eyepiece was centred to match the optical axis of the main beam. Hence, any stellar source appearing on the cross-hair in the previewer would be on the optical axis of the instrument.

Diaphragm Wheel

The wheel held five different sizes of diaphragm. The size of diaphragms ranged from 0.2mm, 0.3mm, 0.6mm, 2.0mm, and empty. The diaphragms were made of non-metallic material because metallic diaphragms polarize light. The wheel was rotated via a gear system from the outside of the polarimeter box.

Half-wave plate

The half-wave plate was a superachromatic type. This was placed immediately after the diaphragm. The half-wave plate was set strictly in the plane perpendicular to the optical axis so that during rotation it did not deviate the path of the light off the axis by prismatic effects. Image wobble effects were thus kept to the minimum. Also, the effect was reduced by:

- setting the image of the telescope aperture in the detector surface.
- half-wave plate remained stationary during an exposure.

The half-wave plate was placed in a cylindrical housing within a ball race. Two cogs with the same ratio were used to rotate the half-wave plate. Discrete rotation of the half-wave plate was set, such that in every rotation of 22.5° it would locate a mechanical stop. In this way the half-wave plate could be rotated from its initial point (0°) to 67.5° (in steps of 22.5°) and back again to the same positions.

Collimating Lens

The incident beam emerging from the diaphragm wheel and the half-wave plate had to be collimated. The collimation was achieved by using a 75mm focal length with a diameter of 30mm.

Polarizer (Savart plate)

The Savart plate measured 20mm square by 40mm long and was held by a rubber compound inside a surrounding metal cylinder of 30mm diameter and length 40mm. This was placed immediately after the collimating lens at a distance of 75mm. The Savart plate was centred along the optical axis, and was held firmly by a metal tube. The Savart plate was oriented such that the emerging beams were approximately in the plane parallel to the plane of the equatorial mount of the telescope. Thus the two emerging polarized beams have their direction of vibration parallel to the equatorial and polar axes respectively.

Pellicle Beam Splitter (post-viewer)

A beam splitter was used to redirect some of the light to a post-viewing system. The pellicle transmission was such that 10% of the incoming light was reflected to the viewer or the tracking system.

Telescope Tracking System

The tracking of the telescope itself was inadequate for long exposures and therefore it was necessary to incorporate a CCD guidance system in our prototype polarimeter. The telescope tracking system was achieved by using a commercially available CCD (the SBIG ST–4 CCD). The camera has a controller unit which executes specific tasks and was connected directly to the telescope drive motor. Therefore any movement in the stars position on the CCD chip was immediately corrected by sending commands to the drive units's right ascension and declination motors.

For tracking purposes one of the polarized beams from the pellicle had to be extinguished and this was done using a sheet of polaroid between the pellicle and the focusing lens system of the post-viewer. The remaining beam was then used to place the star image at the centre of the tracking CCD chip.

Camera lens

The camera lens was a commmercial 50mm photographic lens. The image of the telescope aperture had to be de-magnified by a factor of 2.5 so that it could fit within the area of the CCD chip. The camera lens was placed at 175mm from the image of the telescope aperture. The data recording CCD chip was located at 70mm from the camera lens to produce the right de-magnification.

3.3.4 Determination of the Stokes' Parameters (two beam method)

This method consists of using a two beam set-up and successively interchanging the polarization states of the beams. Only two measurements are required to determine each Stokes' parameter. These are achieved by altering the half-wave plate settings. From section 2.3 it was seen that the output from a simple double-beam polarimeter is represented by;

$$I(\psi) = \frac{1}{2}(I \pm Q\cos 4\psi \pm U\sin 4\psi) \tag{3.18}$$

The above equation is a general form of a double beam polarimeter where a rotatable half-wave plate is used. The signs, + ($\|$) refers to Beam 1 (Ordinary ray) and – ($\perp$) refers to Beam 2 (Extraordinary ray). The above equation must include the effects of variable atmospheric transmission, detector gain etc. Thus, for the two beams;

$$I_{\|}(\psi) = \frac{1}{2}\, T(t)\; G_{\|}\; (I + Q\cos 4\psi + U\sin 4\psi) \tag{3.19}$$

$$I_{\perp}(\psi) = \frac{1}{2}\, T(t)\; G_{\perp}\; (I - Q\cos 4\psi - U\sin 4\psi) \tag{3.20}$$

where, $T(t)$ is the atmospheric effects at time t, and $G_{\|}, G_{\perp}$ refer to the CCD pixel sensitivity to the polarized light for ordinary ($\|$) and extra-ordinary ($\perp$) beams respectively. By combining both of the above equations with the appropriate setting of the half-wave plate it is possible to determine the normalized Stokes' parameters. In order to achieve this, we require at least four intensity measurements at half-wave plate settings of 0°, 22.5°, 45° and 67.5°. Initially the half-wave plate will be orientated with its fast axis parallel to the direction of vibration of the ordinary beam ($\|$) in the stationary polarizer (such as a Calcite plate), thus $\psi = 0°$ (set in the north-south direction), so that the ordinary beam contains the $+Q$ component and the extraordinary beam, $-Q$. Let the measured intensities be denoted by $I_{\|}(0°)$ and $I_{\perp}(0°)$ for the two beams, where,

$$I_{\|}(0°) = \frac{1}{2}\, T_{0°}(t)\; G_{\|}\; (I + Q) \tag{3.21}$$

$$I_{\perp}(0°) = \frac{1}{2}\, T_{0°}(t)\; G_{\perp}\; (I - Q) \tag{3.22}$$

Now the half-wave plate is rotated by 45° and the intensity measured such that,

$$I_{\|}(45°) = \frac{1}{2}\, T_{45°}(t)\; G_{\|}\; (I - Q) \tag{3.23}$$

$$I_{\perp}(45°) = \frac{1}{2}\, T_{45°}(t)\; G_{\perp}\; (I + Q) \tag{3.24}$$

The above four intensities are required to measure the Stokes' parameter Q, in order to measure the Stokes' parameter U, the half-wave plate is first set at 22.5°, where

$$I_{\|}(22.5°) = \frac{1}{2}\, T_{22.5°}(t)\; G_{\|}\; (I + U) \tag{3.25}$$

$$I_{\perp}(22.5°) = \frac{1}{2}\, T_{22.5°}(t)\; G_{\perp}\; (I - U) \tag{3.26}$$

and then rotated by 45° to 67.5°, where,

$$I_{\parallel}(67.5°) = \frac{1}{2}\, T_{67.5°}(t)\; G_{\parallel}\; (I - U) \tag{3.27}$$

$$I_{\perp}(67.5°) = \frac{1}{2}\, T_{67.5°}(t)\; G_{\perp}\; (I + U) \tag{3.28}$$

To cancel out the atmospheric effect ($T(t)$) and the CCD pixel sensitivity ($G_{\parallel}, G_{\perp}$), the ratio of the two intensity measurements at $I(0°)$ (equation 3.17 and 3.18) and $I(45°)$ (equation 3.19 and 3.20) are taken, giving;

$$R(0°) = \frac{\frac{1}{2}\, T_{0°}(t)\; G_{\parallel}\; (I + Q)}{\frac{1}{2}\, T_{0°}(t)\; G_{\perp}\; (I - Q)} = \frac{G_{\parallel}\; (I + Q)}{G_{\perp}\; (I - Q)} \tag{3.29}$$

and

$$R(45°) = \frac{\frac{1}{2}\, T_{45°}(t)\; G_{\parallel}\; (I - Q)}{\frac{1}{2}\, T_{45°}(t)\; G_{\perp}\; (I + Q)} = \frac{G_{\parallel}\; (I - Q)}{G_{\perp}\; (I + Q)} \tag{3.30}$$

where $T_{0°}(t)$ and $T_{45°}(t)$ have been cancelled. By taking a further ratios $\frac{R(0°)}{R(45°)}$ the CCD pixel sensitivity ($G_{\parallel}, G_{\perp}$) is also eliminated.

$$\mathcal{R} = \frac{R(0°)}{R(45°)} = \frac{\frac{G_{\parallel}\; (I+Q)}{G_{\perp}\; (I-Q)}}{\frac{G_{\parallel}\; (I-Q)}{G_{\perp}\; (I+Q)}} \tag{3.31}$$

giving,

$$\mathcal{R} = \left(\frac{I + Q}{I - Q}\right)^2 \tag{3.32}$$

This can be further manipulated so that:

$$\mathcal{R}^{\frac{1}{2}} = \frac{I+Q}{I-Q} \tag{3.33}$$

dividing the numerator and denominator by I, where $q = \frac{Q}{I}$,

$$\mathcal{R}^{\frac{1}{2}} = \frac{1+q}{1-q} \tag{3.34}$$

and thus,

$$q = \frac{\mathcal{R}^{\frac{1}{2}} - 1}{\mathcal{R}^{\frac{1}{2}} + 1} \tag{3.35}$$

Similarly this treatment is extended to the Stokes' U parameter by using equations from 3.21 to 3.34. Hence, the Normalized Stokes' parameters q and u are derived from the four positions of the half-wave plate.

The Stokes' parameters can be converted into degree of polarization by;

$$p = \sqrt{(q^2 + u^2)}\ , \tag{3.36}$$

and position angle, θ, by,

$$\psi = \frac{1}{2}\ \arctan(\frac{u}{q})\ . \tag{3.37}$$

3.3.5 Photon Noise Calculation

As seen, we require two exposures with the half-wave plate rotated by 45 degrees between them to calculate one Stokes' parameter. In order to be able to calculate the limiting noise of the determination, the signals must be expressed in terms of photon counts and

Poisson statistics must be applied. From each exposure $N_{0||}$, $N_{0\perp}$ and $N_{45||}$, $N_{45\perp}$ photons are detected. A similar treatment as in the previous section can be applied. Equation 3.31 may be represented as;

$$\frac{(I+Q)^2}{(I-Q)^2} = \frac{N_{0||}N_{45\perp}}{N_{45||}N_{0\perp}} \tag{3.38}$$

manipulation of the above gives,

$$q = \frac{(N_{0||}N_{45\perp})^{\frac{1}{2}} - 1}{(N_{45||}N_{0\perp})^{\frac{1}{2}} + 1} \tag{3.39}$$

For small polarizations, where $N_{0||} = N_{0\perp} = N_{45||} = N_{45\perp} = N$. Hence, it can be demonstrated from using fractional errors that the photon noise is given by;

$$\Delta q = \frac{1}{2}\sqrt{\frac{1}{N}} \tag{3.40}$$

A similar expression also applies to the u parameter.

3.3.6 Data Acquisition

An IBM-compatible laptop computer was used for CCD control and data acquisition. The CCD CPU (Central Processing Unit) box was connected to the laptop via a RS232 port. The software provided by the SBIG group was used to capture the images. The information regarding the status of the CCD is handled by the link to the laptop computer.

The PC and the CCD electronics were switched on and then shuttered and the image was readout. This is to clean the CCD chip. The temperature of the CCD was then set to $-45°$ below the ambient temperature. The above was done 30 minutes prior to the observations, so that the temperature is brought to the input target and stabilized.

The observational procedure used to test the proto-type instrument was as follows;

1. The chosen star was located on the previewer system.
2. The source was viewed by the post-viewer system and placed at the centre of the diaphragm.
3. A suitable diaphragm was chosen.
4. Test photometric brightness with the half-wave plate 0°.
5. Select the required integration time, so that the image does not saturate.
6. The second CCD attached to the post-viewer and programmed to track the star.
7. Take dark exposure.
8. Take CCD image at half-wave plate setting of 0^o.
9. Off-set the star and record sky background.
10. Re-centre star.
11. Re–start the tracking system.
12. Repeat from 8 to 11 at half-wave settings at 22.5^o, 45^o and 67.5^o

At the end of each run there were four stellar images and four sky background images. Each image was subsequently transferred to the CCD memory and were saved automatically by the CCD software.

The image data was initially saved as a compressed format of the SBIG. These image files were archived and were later converted to the FITS format.

3.4 Method of Data Reduction and Analysis

Reducing the four frames, with four images and sky background is a fairly simple procedure. The basic data analysis programs were written on the STARLINK system. Combination of STARLINK packages were utilized in the analysis, such as FIGARO and

KAPPA. Several C–Shell scripts were written to incorporate and automate the reduction procedures.

The initial procedure was to convert the image data from ST6 format to FITS, this was done within the ST6 package. The FITS format images were then transferred to the STARLINK UNIX system. These FITS files were converted to the NDF format (see STARLINK Guide) of the STARLINK. The analysis of the data is as follows;

- Subtract the sky dark exposure from the four polarized images
- Remove bad pixels
- Apply the gain factor for the system
- Choose a region free from over-lapping (see Fig. 3.5)
- Calculate the Normalized Stokes parameters q and u (see section 3.3.3)

3.4.1 Polarization Calibration

One of the first tests to be carried out on any new polarimeter before installation on the telescope is a check on its performance in analysing light which is completely polarized (i.e. 100%). The calibration was done by introducing a piece of polaroid into the system. Light coming from a tungsten lamp was focused on to the diaphragm and the half-wave plate of the polarimeter was removed, the polaroid was adjusted until it was accurately crossed with one of the beams of the Savart plate. The half-wave plate was replaced and rotated until the minimum signal was again obtained, indicating that the retarder's axes were parallel to those of the polarizer. The retarder was then clamped into the rotatable gear system of the instrument.

The automatic system already described was then employed to measure the Stokes' parameters. In all cases, the measured degree of polarization, p, fell in the range of 99 percent to 101 percent. Having obtained a satisfactory performance of 100 percent polarization the polarimeter was used on stellar sources known to have low linear polarizations.

3.4.2 Observational Results

The instrument was attached to the 51cm telescope at Cochno station of the University of Glasgow. The data were collected on several moonless nights in April 1994. The initial test (after obtaining the satisfactory calibration) involved was to observe an un-polarized stellar source to determine the instrumental polarization. This will also allow for the accurate determination of the noise level of the polarization.

A brief measurement of the star θ Boo (m_v=4.05), which has no reported intrinsic or interstellar polarization (as this has been frequently used as a zero polarization standard). This star was observed to check the consistency of the data. Two regions (hereafter region A and region B) of 40×80 (= 3200) pixels within the aperture image were chosen (see Fig. 3.6). A repetitive measurement of this star was made. The Normalized Stokes' parameters q and u with their standard errors for the two regions are shown in Table 3.2 and Table 3.3. It is seen from the tables that, from a single observation (30 second exposure time) the achievable uncertainty on the values are in order of ± 0.0001 for 3200 pixels. The observed counts per pixel were in order of 10^5 photons.

As expected the instrumental polarization varies across the telescope mirror. Figure 3.6 show the $q - u$ diagram of the two areas of the telescope aperture. The degree of polarization is in the same order, however the position angle of the polarization changes from region A to region B. These regions were at the opposite sides of the telescope primary mirror. The differences in the polarization can be explained by the angle of incident of the light rays reflected from the primary mirror which changes the direction of the polarization. However, this effect should average out over the whole of the telescope mirror.

Unfortunately, due to time constraints it was not possible to extend the observations further by observing the standard polarized stars. This would have allowed investigation to see how well the instrumental polarization could have been subtracted from the polarized source and check on the consistency of measuring stellar polarization.

Number of Observations	$\overline{q} \pm \sigma_q$	$\overline{u} \pm \sigma_u$
Data Set 1	$+0.000906 \pm 0.000096$	-0.000357 ± 0.000080
Data Set 2	$+0.000139 \pm 0.000093$	-0.000100 ± 0.000097
Data Set 3	$+0.000872 \pm 0.000103$	-0.000432 ± 0.000112
Data Set 4	$+0.000044 \pm 0.000051$	-0.000864 ± 0.000110
Data Set 5	$+0.000233 \pm 0.000089$	-0.000135 ± 0.000089
Data Set 6	$+0.000249 \pm 0.000091$	$+0.000013 \pm 0.000138$
Data Set 7	-0.000087 ± 0.000076	-0.000346 ± 0.000086
Data Set 8	$+0.000857 \pm 0.000092$	-0.000067 ± 0.000142
Data Set 9	$+0.000408 \pm 0.000096$	-0.000549 ± 0.000088
Data Set 10	$+0.000949 \pm 0.000131$	-0.000190 ± 0.000074
Data Set 11	$+0.000757 \pm 0.000057$	-0.000120 ± 0.000081
Data Set 12	$+0.000917 \pm 0.000048$	$+0.000175 \pm 0.000094$
Data Set 13	$+0.000624 \pm 0.000149$	-0.000049 ± 0.000126
Data Set 14	$+0.000565 \pm 0.000072$	-0.000293 ± 0.000057
Data Set 15	$+0.000333 \pm 0.000100$	-0.000134 ± 0.000047
Data Set 16	$+0.000418 \pm 0.000086$	-0.000804 ± 0.000129
Data Set 17	$+0.000432 \pm 0.000122$	-0.000325 ± 0.000117
Data Set 18	$+0.000783 \pm 0.000102$	-0.000131 ± 0.000108
Data Set 19	-0.000041 ± 0.000127	$+0.000035 \pm 0.000126$
Data Set 20	$+0.000537 \pm 0.000098$	-0.000287 ± 0.000092
Data Set 21	$+0.000439 \pm 0.000134$	$+0.000085 \pm 0.000052$

Table 3.2: Data for the region A of the CCD chip

Number of Observations	$\overline{q} \pm \sigma_q$	$\overline{u} \pm \sigma_u$
Data Set 1	-0.000921 ± 0.000096	-0.000872 ± 0.000101
Data Set 2	-0.000806 ± 0.000065	-0.000528 ± 0.000117
Data Set 3	-0.000018 ± 0.000063	-0.000177 ± 0.000140
Data Set 4	-0.000005 ± 0.000076	-0.000362 ± 0.000103
Data Set 5	$+0.000007 \pm 0.000103$	-0.000133 ± 0.000062
Data Set 6	-0.000191 ± 0.000087	-0.000655 ± 0.000118
Data Set 7	-0.000624 ± 0.000122	-0.000142 ± 0.000087
Data Set 8	-0.000953 ± 0.000053	-0.000610 ± 0.000063
Data Set 9	-0.000961 ± 0.000147	-0.001375 ± 0.000060
Data Set 10	-0.000107 ± 0.000135	-0.000287 ± 0.000053
Data Set 11	-0.000903 ± 0.000079	-0.001405 ± 0.000103
Data Set 12	-0.000421 ± 0.000079	-0.000823 ± 0.000074
Data Set 13	-0.000342 ± 0.000046	-0.001069 ± 0.000080
Data Set 14	-0.000897 ± 0.000086	-0.001265 ± 0.000057
Data Set 15	-0.000510 ± 0.000121	-0.000588 ± 0.000059
Data Set 16	-0.000954 ± 0.000102	-0.000240 ± 0.000124
Data Set 17	$+0.000013 \pm 0.000058$	-0.000097 ± 0.000049
Data Set 18	$+0.000249 \pm 0.000067$	-0.000588 ± 0.000064
Data Set 19	-0.000374 ± 0.000081	-0.000160 ± 0.000054
Data Set 20	-0.000281 ± 0.000101	-0.000364 ± 0.000049
Data Set 21	-0.000082 ± 0.000094	-0.000216 ± 0.000050

Table 3.3: Data for the region B of the CCD chip

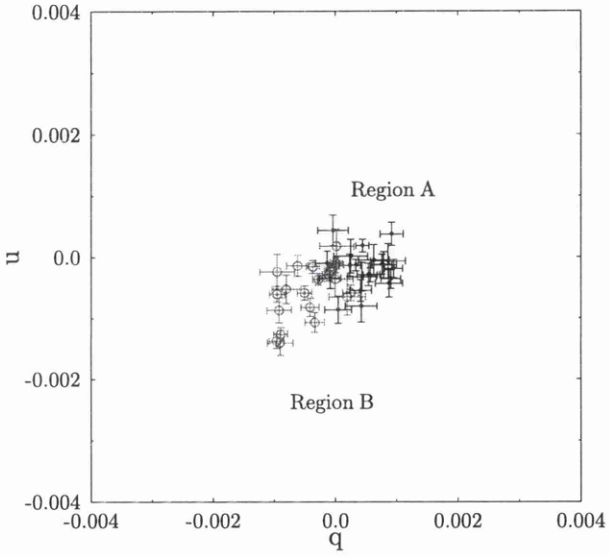

Figure 3.6: A $q - u$ plot of the complete set of 21 data points for region A and B.

3.4.3 Statistical Properties of the Data

It is expected that repeated measures of Stokes' parameters q and u come from a Normal distributions (see Clarke et al., 1983). To check the experimental behaviour, Normality tests were performed on q and u. One simple way of investigating the data is to take the moments about the mean of the distribution. A Normal distribution is completely characterized once the mean ($\mu = \frac{1}{N}\sum_i^N x_i$) and σ^2 are known. However, for any distribution, it is possible to take moments defined by;

$$\mu_n = \frac{1}{N}\sum_i^N (x_i - \mu)^n \tag{3.41}$$

where μ_n is the n$^{\text{th}}$ moment of the distribution. Note that $\mu_2 = \sigma^2$ provides a measure of the variance, and values n = 3 and n = 4 allow investigation of skewness and kurtosis respectively (see Brooks et al., 1994).

$$Skewness = \frac{\mu_3^2}{\mu_2^3} = 0 \tag{3.42}$$

and

$$Kurtosis = \frac{\mu^4}{\mu_2^2} = 3 \tag{3.43}$$

It should be noted that the above values are only valid for a large data sample. It is expected that with 3200 points, the values of skewness and kurtosis to be close to 0 and 3 respectively. Therefore, confidence limit can be ascribed to the calculated values.

The above test demonstrated that the distribution for both regions A and B did indeed come from Normal distributions. The general skewness and kurtosis for region A were centred around 0.003 and 3.056, and for region B around 0.024 and 2.973 respectively. Frequency distributions of individual measured Stokes' parameters for a data sample which consist of 3200 pixels are shown in Figures 3.7 and 3.9.

As the data relate to an unpolarized star, it is expected that the probability distribution of polarization be of a Rician form (see Simmons and Stewart, 1985). As polarization

is very close to zero, there is a need to consider Rician statistics for p. The form of the probability distribution for p is;

$$F(P, P_o) = P\, e^{\frac{-(P^2+P_o^2)}{2}}\, I_o(iPP_o) \tag{3.44}$$

where I_o is the zero order Bessel function, P is the ratio of observed degree of polarization to the noise ($\frac{P}{\sigma}$) and P_o is the ratio of true polarization to the noise ($\frac{P_o}{\sigma}$). If the source is unpolarized then $P_o = 0$ and the distribution function reduces to;

$$F(P, 0) = P\, e^{\frac{-P^2}{2}} \tag{3.45}$$

Illustrations in Figures 3.8 and 3.10 show the observed polarization data with the theoretical Rician curve. It can be seen that the observed data reveal polarization to be present. Since the match between the theoretical curve ($P_o = 0$) and data is not exact. This mismatch can be attributed to the instrumental polarization.

3.4.4 Instrumental precision

The initial test was to see if the observed data noise arises purely from the theoretical Poissonian statistics or whether other experimental noise are present. Figures 3.11 and 3.12 show the standard errors for the mean values of the Stokes' parameter q and u, according to increasing the number of contributing pixels. Where,

$$\overline{q}_N = \frac{\sum_{i=1}^{N} q_{ij}}{N} \; ; \quad \overline{u}_N = \frac{\sum_{i=1}^{N} u_{ij}}{N} \tag{3.46}$$

$$\sigma_q = \sqrt{\frac{1}{(N-1)} \sum_{i=1}^{N} (q_{ij} - \overline{q}_N)^2} \tag{3.47}$$

In the exercise, the number of pixels (N) are varied from 100 to 3200 in steps of $\approx$ 200 pixels and the associated standard errors are calculated as above. These figures also show

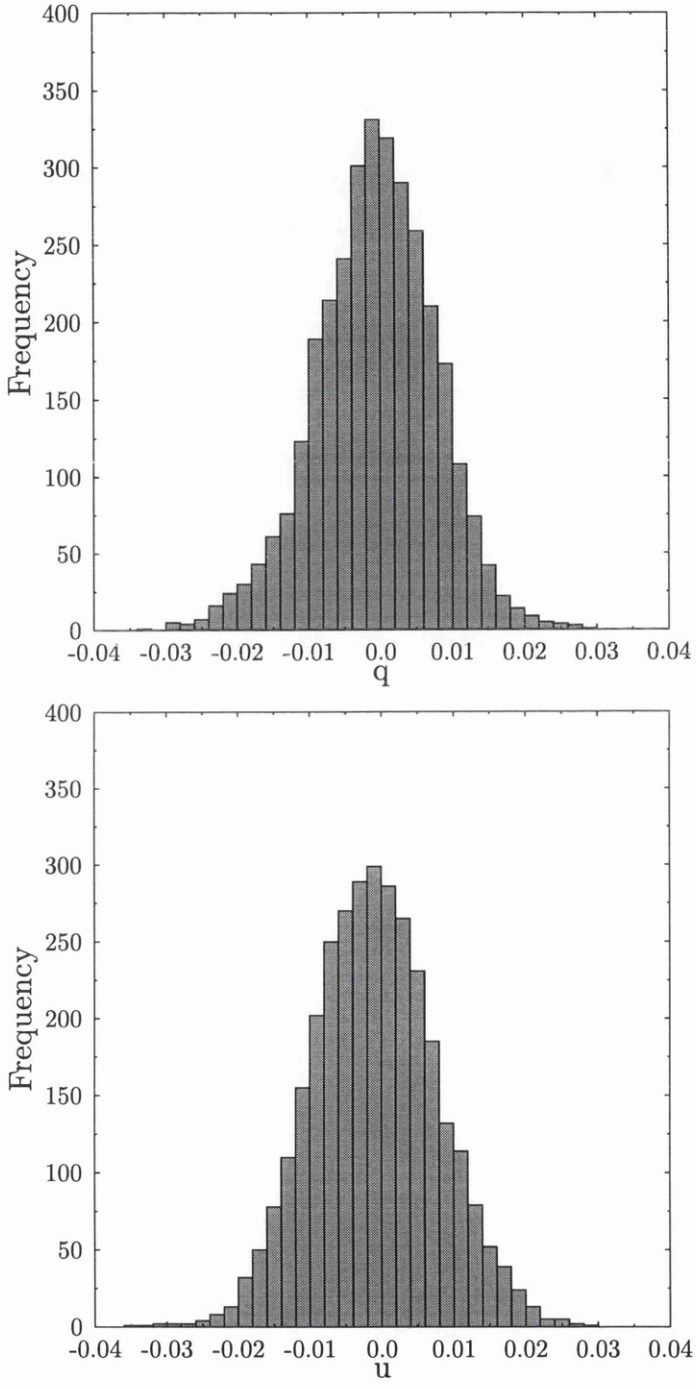

Figure 3.7: Frequency histogram of the Stokes' parameters q and u for area A, with mean values of $\overline{q}$ being -0.000408 and $\overline{u}$ being -0.000549.

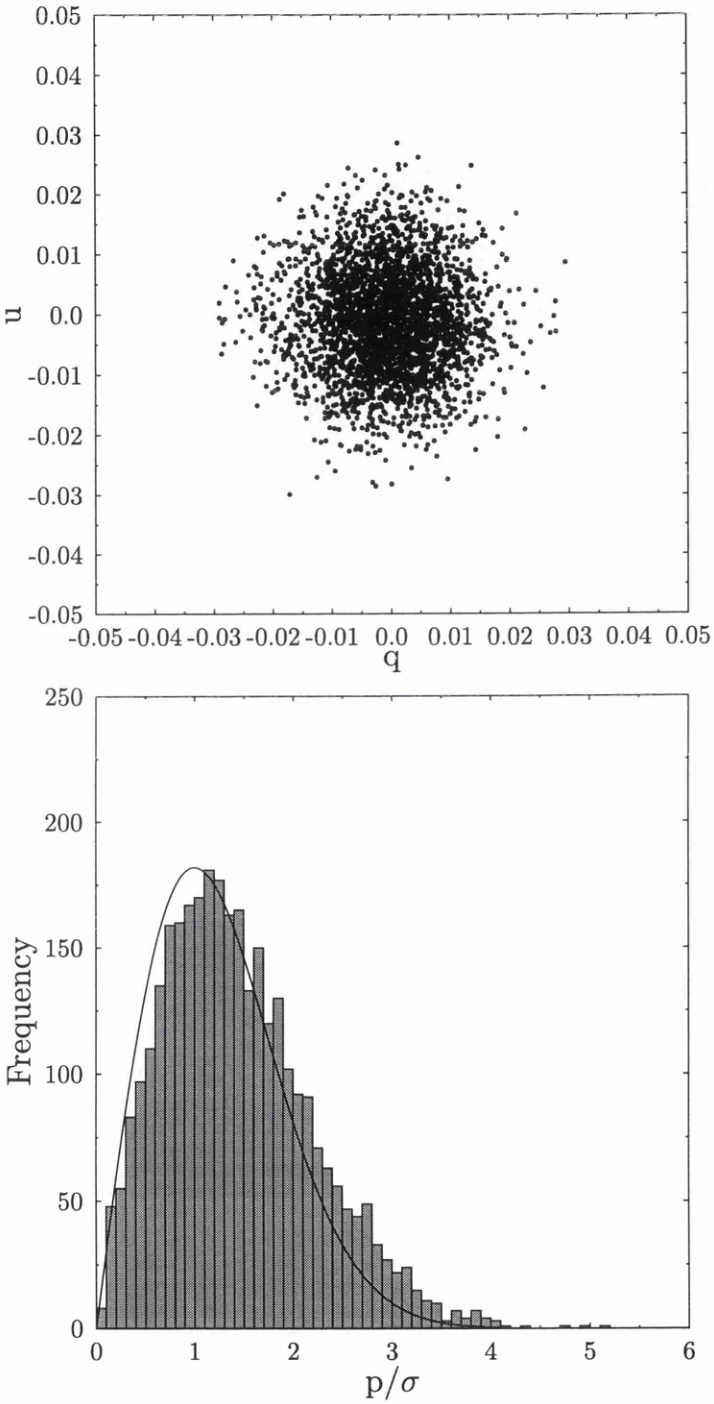

Figure 3.8: Frequency histogram of $\frac{p}{\sigma}$ and q, u plot for area A; continuous curve is the theoretical distribution (Rician distribution) expected if the data showed zero polarization. The histogram indicates that there is an apparent polarization of 0.0026%.

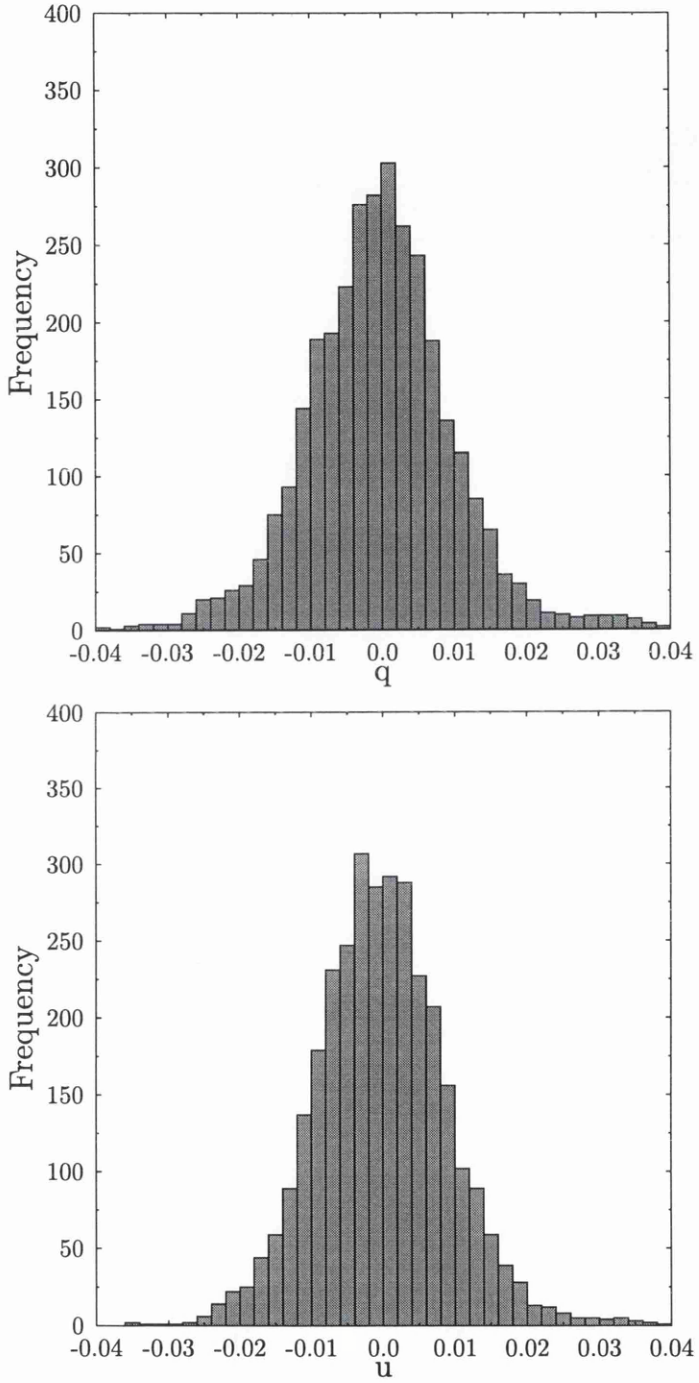

Figure 3.9: Frequency histogram of the Stokes' parameters q and u for area B, with mean values of $\overline{q}$ being -0.000903 and $\overline{u}$ being -0.001405.

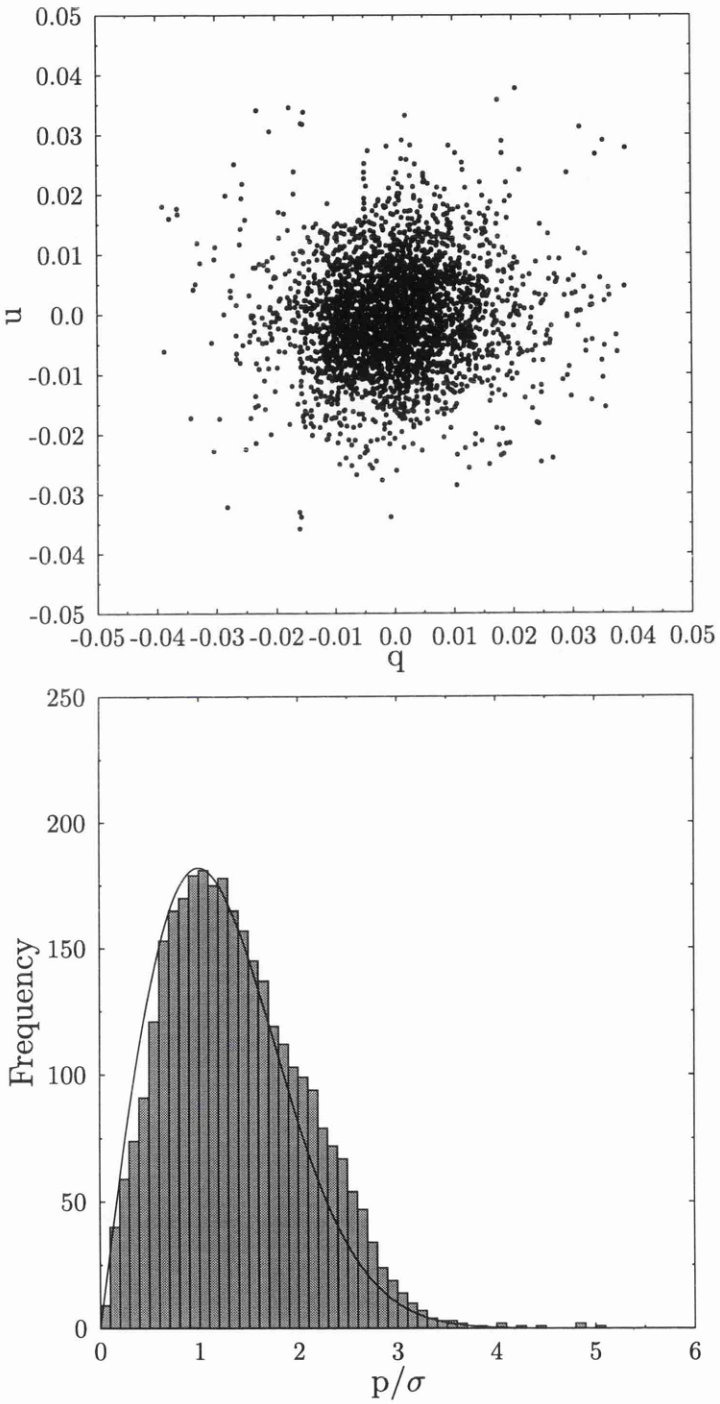

Figure 3.10: Frequency histogram of $\frac{p}{\sigma}$ and q, u plot for area B; continuous curve is the theoretical distribution (Rician distribution) expected if the data showed zero polarization. The histogram indicates that there is an apparent polarization of 0.0019%.

the expected theoretical errors, σ_{ϵ_q}, σ_{ϵ_u}, based on Poissonian statistics for the N number of pixels.

It is evident from Figures 3.11ab and 3.12ab that the standard errors from the theoretical curves do not completely match the errors calculated from q and u, even at 3200 data points. The experimental standard error for q and u of 200 pixels are 0.000534 and 0.000416 respectively, this can be compared with the theoretical estimation of 0.000370 for q and u. There is overestimation of the errors by 30% and this ratio does not reduce with increasing number of pixels.

The most likely explanation may lie in the readout noise of the CCD detector. The readout noise is usually thought to be:

- independent of position on the CCD.
- representable as a simple Gaussian error distribution.

In Section 3.2.1 the *rms* readout noise of the CCD detector was calculated to be 40 electrons. From a simple statistical analysis, the signal-to-noise ratio of a single pixel with X number of ADU and subject to ROe^- is

$$\frac{S}{N} = \frac{\mathcal{G}X}{\sqrt{\mathcal{G}X + RO^2}} \tag{3.48}$$

For example, if $X = 1000$, $\mathcal{G} = 10$ and $RO = 40$ then $\frac{S}{N} = 92.8$ nearly the Poisson limit (true Poisson $= 100$). Figure 3.13a shows the $\frac{S}{N}$ with different readout noise levels.

However, if N_{pix} individual pixels are summed over to yield the same signal, $\mathcal{G}X$, then:

$$\frac{S}{N} = \frac{\mathcal{G}X}{\sqrt{\mathcal{G}X + N_{pix}RO^2}} \tag{3.49}$$

Now with same situation as above and with $N_{pix} = 3200$ the $\frac{S}{N} = 4.41$. Therefore, for this case the data is very read noise dominated. It is useful to note that co-adding many

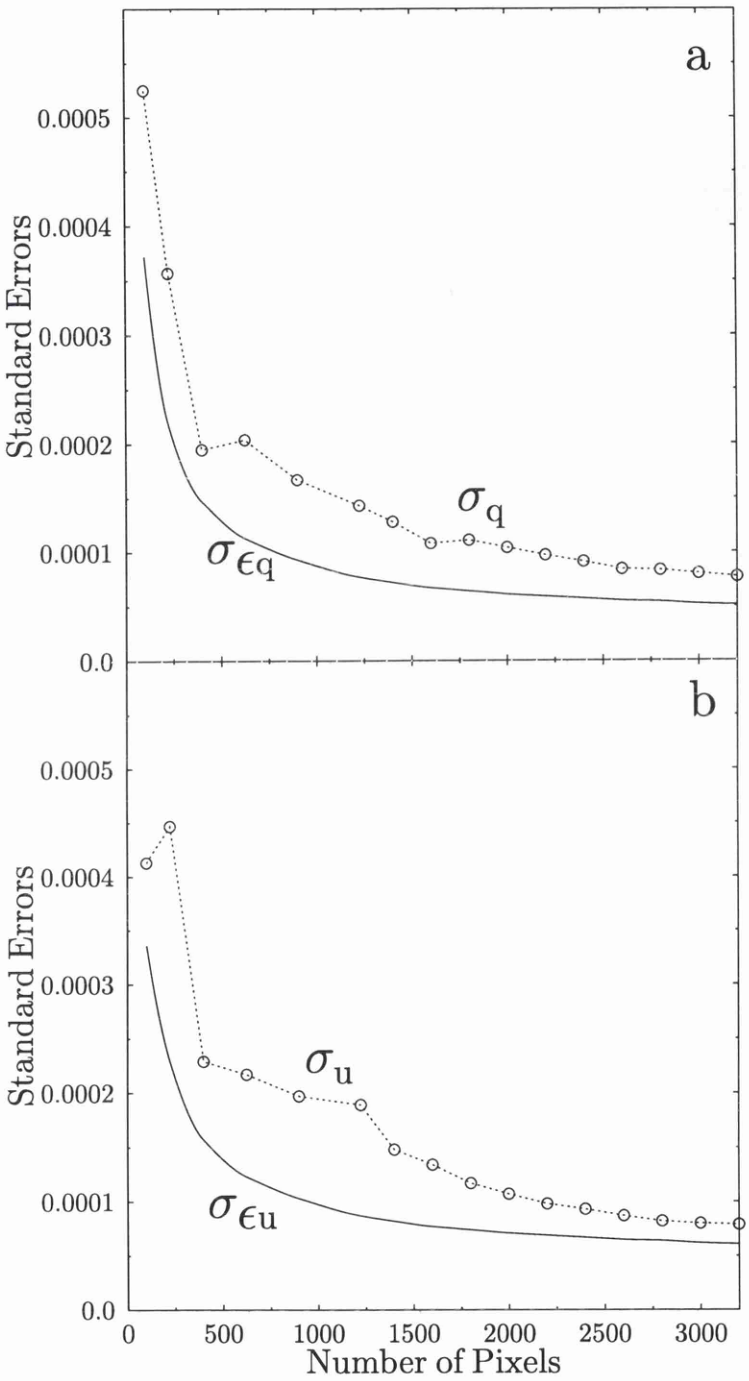

Figure 3.11: Plot of the standard errors against the number of pixels in the region A for the Stokes parameters q(a) and u(b). The solid line is the theoretical Poissonian statistics σ_{ϵ_q} and σ_{ϵ_u}.

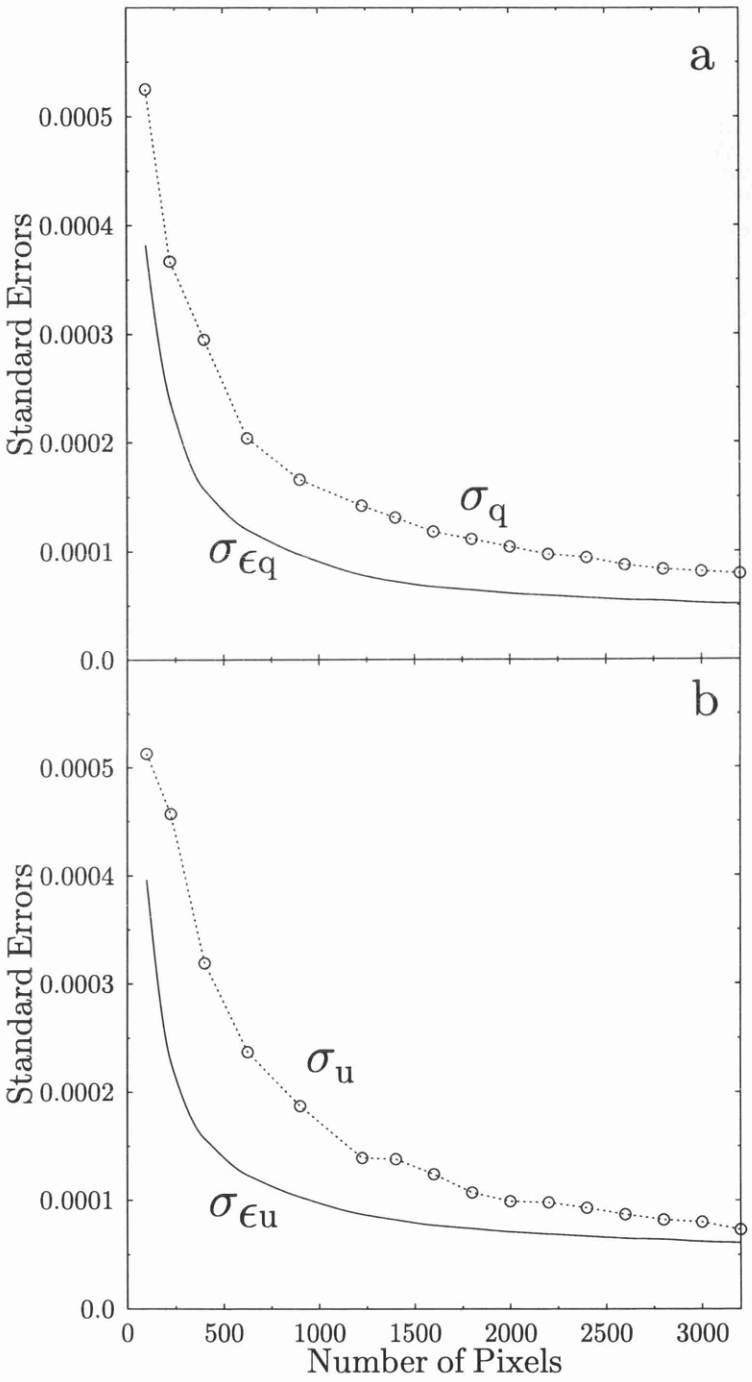

Figure 3.12: Plot of the standard errors against the number of pixels in the region B for the Stokes parameters q(a) and u(b). The solid line is the theoretical Poissonian statistics σ_{ϵ_q} and σ_{ϵ_u}.

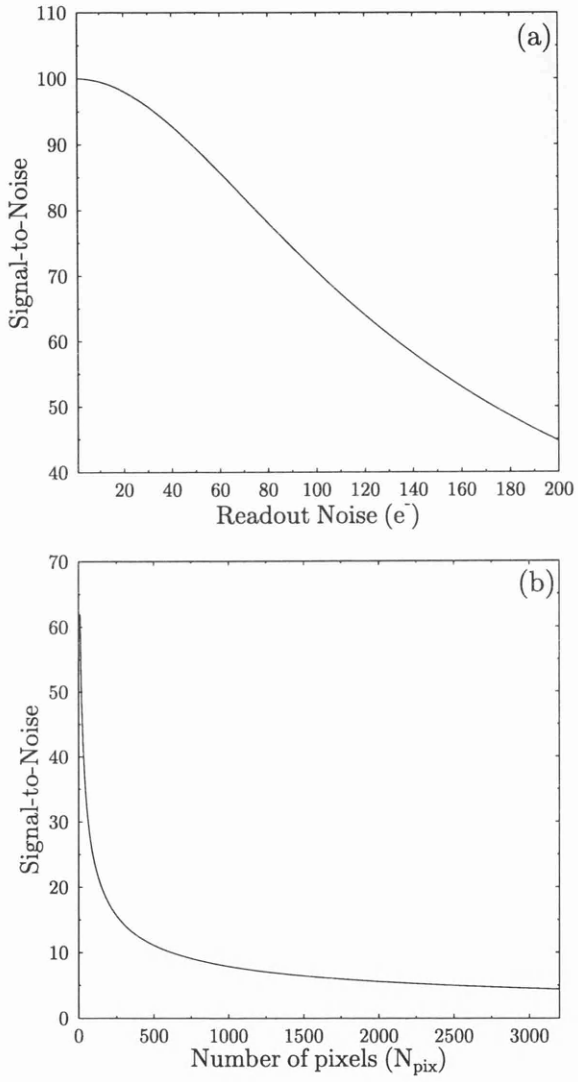

Figure 3.13: Graph **(a)** shows the Signal-to-Noise ratio according to the values of readout noise (Equation 3.48), **(b)** shows that for a given flux the Signal-to-Noise ratio degrades according to the number of pixels used to assess that flux (Equation 3.49).

N_{read} data frames can be done to reduce the uncertainty of the mean for each pixel value to $\frac{RO}{N_{read}^{\frac{1}{2}}}$. However, multiple readouts (to accumulate the same total signal) degrade $\frac{S}{N}$. This is shown in Figure 3.13b.

In order to discover the disparity between the theoretical poissonian values and the experimental curves in Figures 3.11 and 3.12 are further investigated.

The theoretical curve was obtained by summing up the pixels so that;

$$\sigma_{\epsilon_q} \text{ or } \sigma_{\epsilon_u} = \sqrt{\sum_{i=1}^{3200} \frac{1}{N_i}} \tag{3.50}$$

where N_i is the number of photons accumalted in pixel i. In considering the readout noise, the effect of readout noise was shown in equations 3.48 and 3.49. By including this noise into the equation 3.50 a new form of the theoretical curve is obtained.

$$\sigma_{\epsilon_q} \text{ or } \sigma_{\epsilon_u} = \sqrt{\sum_{i=1}^{3200} \frac{1}{N_i}} + \sqrt{\sum_{i=1}^{3200} \frac{1}{RO^2}} \tag{3.51}$$

It can be seen that the effect of this addition is to move the theoretical curves in Figures 3.11 and 3.12 towards the experimental curve. However, the value of the readout noise which was determined to be 40 electrons. Figure 3.13 shows the experimental curves and the two theoretical curves - one without the readout noise (σ_ϵ) and the other with the readout noise (R_{σ_ϵ}). It is concluded that the 40 electrons obtained in section 3.2.2 was an underestimation and the true value may be higher.

Hence, the readout noise becomes an irreducible contribution to the degrading of the results. Its effect can be minimized by selection of a CCD with small readout noise, by keeping the number of pixels small that contribute to the signal area, and by minimizing the number of readouts contributing to the signal determination.

The example given above may only be one of many noise sources within CCD and the instrument itself, such as scattered or stray light and overlap problems.

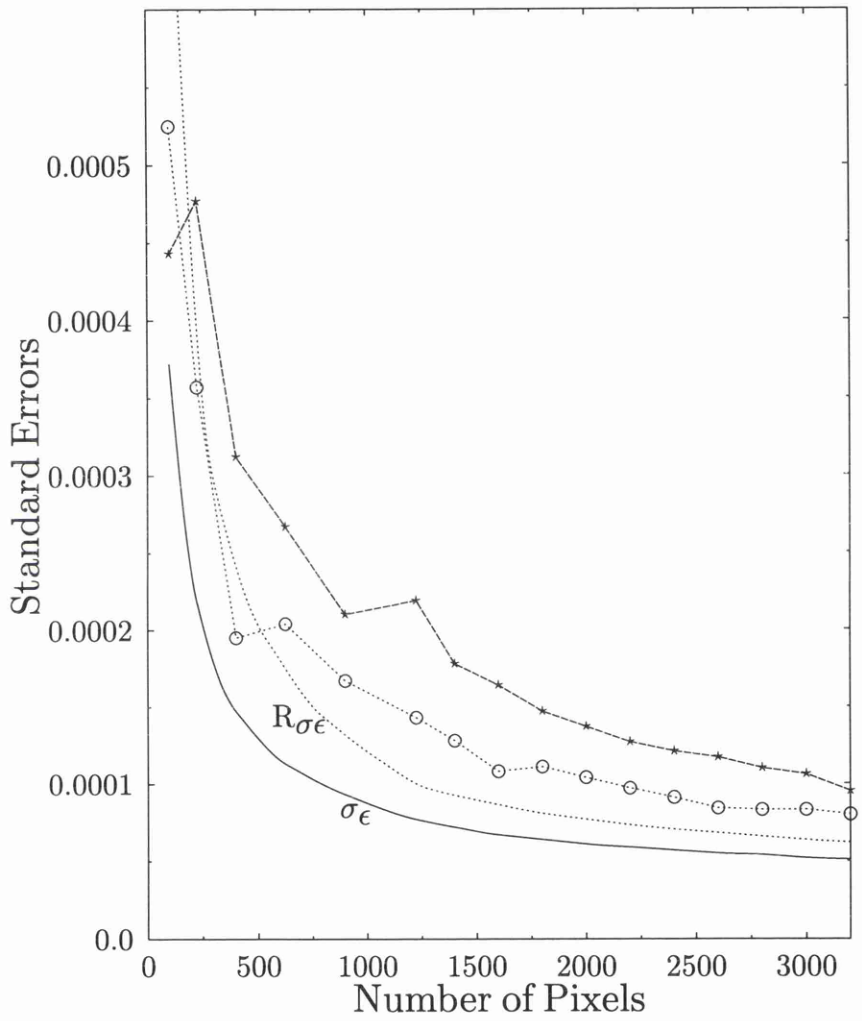

Figure 3.14: Plot of the standard errors against the number of pixels, where ∘ and ⋆ are the experimental σ_q and σ_u respectively. The theoretical curve R_{σ_ϵ} is readout noise corrected (40 electrons) and σ_ϵ is the uncorrected.

Chapter 4

Study of the Terrestrial Blue Sky

4.1 Introduction

It has already been pointed out that the great advantage of a two-dimensional detector is its ability to record the complete stellar spectral line profiles. However, their use are not confined to the spectropolarimetry of stellar objects. One such alternative study to which the two-dimensional detectors has been applied is the investigation of polarization effects within the Fraunhofer line profiles in the spectrum of the terrestrial blue sky light.

The scattering of the Sun's light by various processes in the atmosphere gives, amongst other things, the sky's colour. Also, for a long time it seems to have been widely believed that the spectrum of the sky is identical with that of the solar flux, apart from a few relatively faint dayglow emissions from the upper atmosphere. Grainger and Ring (1962) discovered that the Fraunhofer lines in the spectrum of the blue sky light were less deep than from the direct sun light. This "filling-in" effect also known as the Ring effect was confirmed by Noxon and Goody (1965) and also discovered that there are polarization changes across the Fraunhofer line profiles.

A variety of Fraunhofer lines has been used to explore the Ring effect. All lines display intensity filling-in to some degree with indications of variability during the day. Papers which discuss diurnal changes shows that the behaviour of the Ring effect is not clear cut.

For example, Noxon and Goody (1965) suggest that there is a decrease in the filling-in as the zenith angle increases; Harrison (1976) and Harrison (1975) has presented data that show a smooth increase with zenith angle, the rate of increase steepening towards twilight; Barmore (1975) has shown that the absolute intensity of the added component varies from day to day and lacks coherent trends during a single day.

Line profiles recorded by Noxon and Goody (1965) with orthogonal polarization suggested that the added light is essentially unpolarized. Clarke and McLean (1975) measured the degree of polarization, p, of zenith daytime sky at Hβ and found that the reduction in the line centre was commensurate with the added light being unpolarized. Clarke and Basurah (1989) reported that the Hβ line from the zenith sky reveal that the Ring component is substantially polarized ($\sim$ 25%) particularly at some times of the day.

The majority of the previous investigations of the Ring effect, both photometric and polarimetric, have been performed using some form of single channel scanning spectrometer. Also, in most cases, the deductions made about the effect have been based on comparisons of incomplete spectral line profiles, at subjectively selected points within it. This may be part of the cause of the lack of consensus as to its observed behaviour and interpreted nature.

For example, Clarke and McLean (1975) and Clarke and Basurah (1989) measurements were made using a filter of 2.5Å passband for tilt-scanning. A cyclic sequence of wavelength positions corresponding to the red continuum, line centre and the blue continuum were scanned. Figure 4.1 shows the profile of Hβ line and three wavelength positions in which observations were performed. It is obvious that this technique will be sensitive to spatial movement of the spectral line. Hence any displacement within the spectral line will result the measurement being made of the wing rather than the line bottom in the course of the observation. Therefore, the comparisons with the adjacent wavelength will not always be the same.

Some workers such as Harrison and Kendall (1974) have solely concentrated on the spectrophotometric behaviour of the Ring effect. In performing the spectrophotometric studies

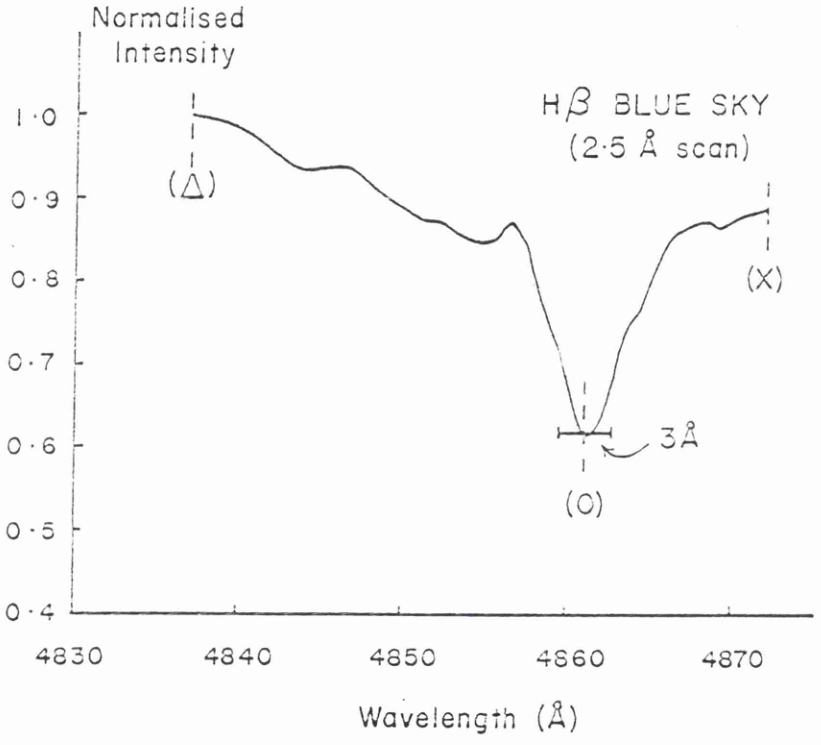

Figure 4.1: An Hβ profile in blue sky light obtained by tilt-scanning a 2.5Å interference filter. Polarimetric measurements were performed at three discrete wavelengths, viz., 4872Å(X), 4861Å(○) and 4837Å(△). [Taken from McLean 1974]

of the blue sky one must also has to be aware of the instrumental effects which could influence the results . As stated previously daytime sky is strongly polarized with the plane of polarization changing from sunrise to sunset. Any spectrophotometric instrument will be sensitive to the state of polarization. It is well known that the grating spectrographs are sensitive to polarized light, this has been demonstrated by Breckinridge (1971). The photometric errors due to the sensitivity of the spectrograph to the changes in polarization and the plane of polarization will invalidate any measurements. One way of dealing with this problem is to place a polarizer prior to the spectrograph. Hence, keeping the plane of the polarization constant with respect to the spectrograph. Harrison and Kendall (1974) do not mention this effect in their paper and one assumes that the effect is uncorrected for.

With the aim of re-investigating the temporal behaviour of the Ring effect more purposefully, a new instrument has been developed and applied to daytime sky photopolarimetric studies, allowing the monitoring of complete line profiles at unique times with the dispersed spectrum falling on a two-dimensional detector. No attempt, however, has been made to determine the absolute strength of the line filling-in by making direct comparisons with recorded solar spectra, such an exercise carrying its own experimental difficulties and associated subtle systematic errors. The experiment described in this Chapter were made solely to investigate the radiation of the daytime sky and to measure the temporal variations of spectral line profiles.

4.2 Design of the Spectropolarimeter

The spectropolarimeter was based on a single channel design. The instrument consists essentially of a half-wave plate, a polarizer and a spectrometer. The modulation of the polarization is achieved by rotation of the half-wave plate before the fixed polarizer and spectrometer. The section below describes the instrument setup and the way in which observations were obtained.

4.2.1 Polarimetric Method

It is readily shown by Clarke and Grainger (1971) that a rotating half-wave plate modulator provides a signal given by:

$$S_\alpha = \frac{\mathcal{G}}{2}\{I + Q\cos 4\alpha + U\sin 4\alpha\} \tag{4.1}$$

where I, Q an U are the Stokes' parameters describing the flux and linear polarization, α in the orientational setting of the axis of the half-wave plate relative to the chosen co-ordinate frame of the principal axis of the polarizer and G is the detector response to unit intensity.

A simple method was adapted to measure the polarization, p, and position angle, Ψ, for any pixel element in the detector. This method is an ideal technique to be used in a single channel detector. A variation of Fessenkov (1935) was employed whereby three frames were recorded at different angular settings of the half-wave plate separated by 30^o (0^o, 30^o and 60^o - the fiduciary angle being arbitrary). The light intensity through the half-wave plate can also be described as follows;

$$S_0 = \mathcal{G}\{1 + pcos4(\Psi)\} \tag{4.2}$$

$$S_{30} = \mathcal{G}\{1 + pcos4(30 + \Psi)\} \tag{4.3}$$

$$S_{60} = \mathcal{G}\{1 + pcos4(60 + \Psi)\} \tag{4.4}$$

With three unknowns ($\mathcal{G}$, p, and Ψ) and three positions of the half-wave plate, one can thus express the three light intensity measurements (S_0, S_{30}, and S_{60}) in terms of polarization and position angle. The degree of polarization is therefore given by;

$$p = \frac{2\{S_0(S_0 - S_{30}) + S_{30}(S_{30} - S_{60}) + S_{60}(S_{60} - S_0)\}^{1/2}}{S_0 + S_{30} + S_{60}} \tag{4.5}$$

and the direction of vibration (position angle),

$$\Psi = \frac{1}{4}\arctan\left\{\frac{\sqrt{3}(S_{60} - S_{30})}{2S_0 - S_{30} - S_{60}}\right\} \tag{4.6}$$

with the quadrant of the polarization vibration angle being determined from the individual signs of the numerator and denominator components of the arctan function.

4.2.2 Optical layout of the Spectropolarimeter

A schematic layout of the spectropolarimeter is shown in Figure 4.2. The spectropolarimeter comprised a collector, a polarimetric module, a spectrometer and a CCD detector.

Telescope system

An $f/4$ photographic camera lens with a focal length of 200mm was used as an objective lens to focus the sky radiation onto the slit of the spectrometer. The plate scale was worked out to be

$$\frac{\delta\theta}{\delta s} = \frac{206265}{F} \ arcseconds\ mm^{-1} ,$$

where F is the focal length of the lens. The plate scale at the focal plane of the lens was 1031 $arcsecs\ mm^{-1}$.

Polarimetric optics

The polarimetric modulator used was a superachromatic quartz-magnesium fluoride half-wave plate. This was followed by a high quality plastic sheet polarizer all placed prior to the entrance slit of the spectrometer. This system, with the direction of vibration of the resolved polarization being constant with respect to the instrument, avoids spurious signals caused by any polarization sensitivity of its subsequent optical elements. The principle axis of the polarizer was set parallel to the slit length so maximizing the transmittance of the optical system, the spectrometer being strongly polarization sensitive.

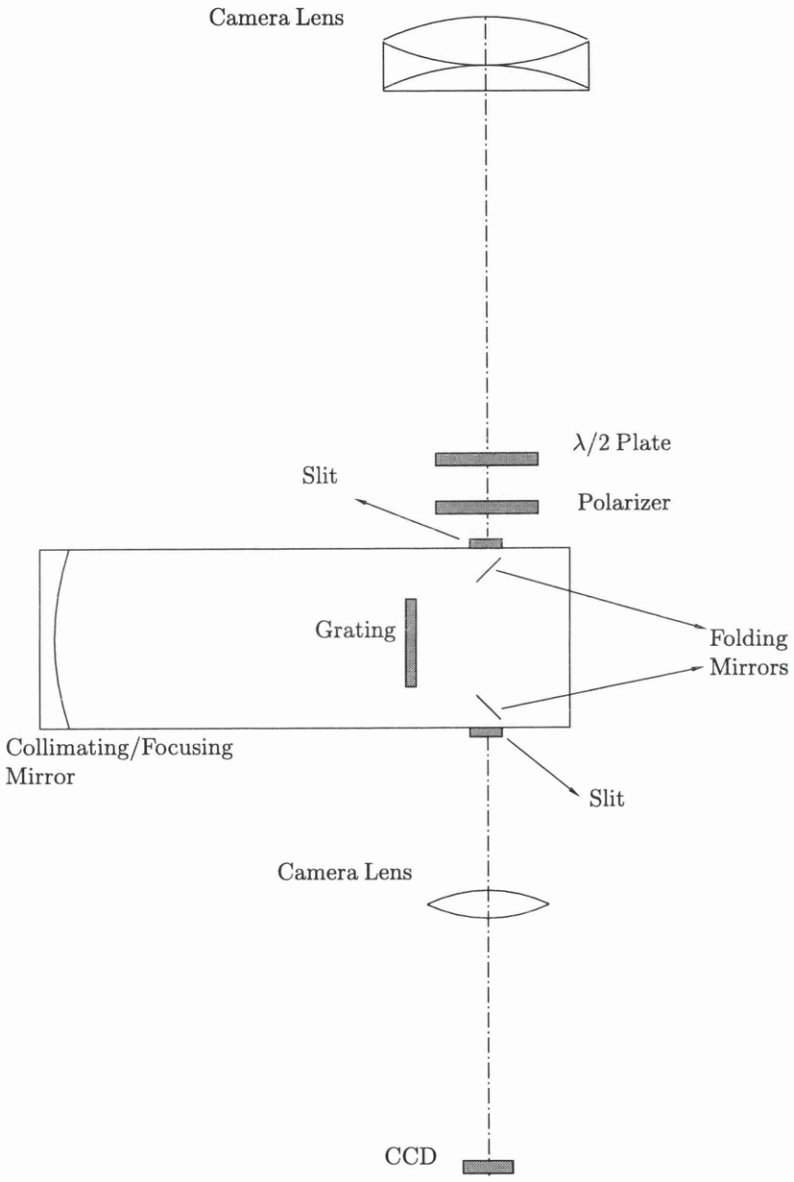

Figure 4.2: Schematic diagram of the Blue sky Spectropolarimeter.

The Spectrometer

The spectrometer was a scanning digital Mini-Chrom (PTR Optics Corporation), with an effective aperture of $f/3.9$ and 74 mm focal length. The spectrometer slit width was 50μ, so limiting the field of view to 51 *arcsecs* (1031×0.05) and maintaining the theoretical spectral resolution to 0.9Å.

The spectral image was transferred onto the CCD chip by a photographic lens of 55mm focal length. Each spectrally resolved element was just slightly oversampled by the pixel structure of the detector chip.

4.2.3 Alignment of the CCD Chip

In the setting up procedure, the CCD chip was aligned parallel to the dispersion. This calibration was accomplished by using a laboratory emission lamp (sodium). The light from the emission lamp was fed into the spectropolarimeter and the CCD was rotated so that the pixel rows coincided with the wavelength. Figure 4.3 shows the image of the sodium D lines for this purpose.

4.3 Method of Observations

The Electronic system of the spectropolarimeter was switched on 30 minutes prior to the observations. The temperature control for the CCD head was set to -40 degrees below the ambient temperature. It was also necessary to use an industrial fan directed towards the CCD head to keep the air circulating and thus reducing the temperature.

Observations were carried out only on cloudless skies. This was to minimize the unwanted light scatter from the clouds, which will degrade the overall intensity and hence false polarization. Two wavelength regions were selected for this study, Hβ(4861Å) and magnesium triplet lines (5183Å). These spectral regions were chosen in order to study whether the polarization variability has any influence on the proximity of the spectral lines.

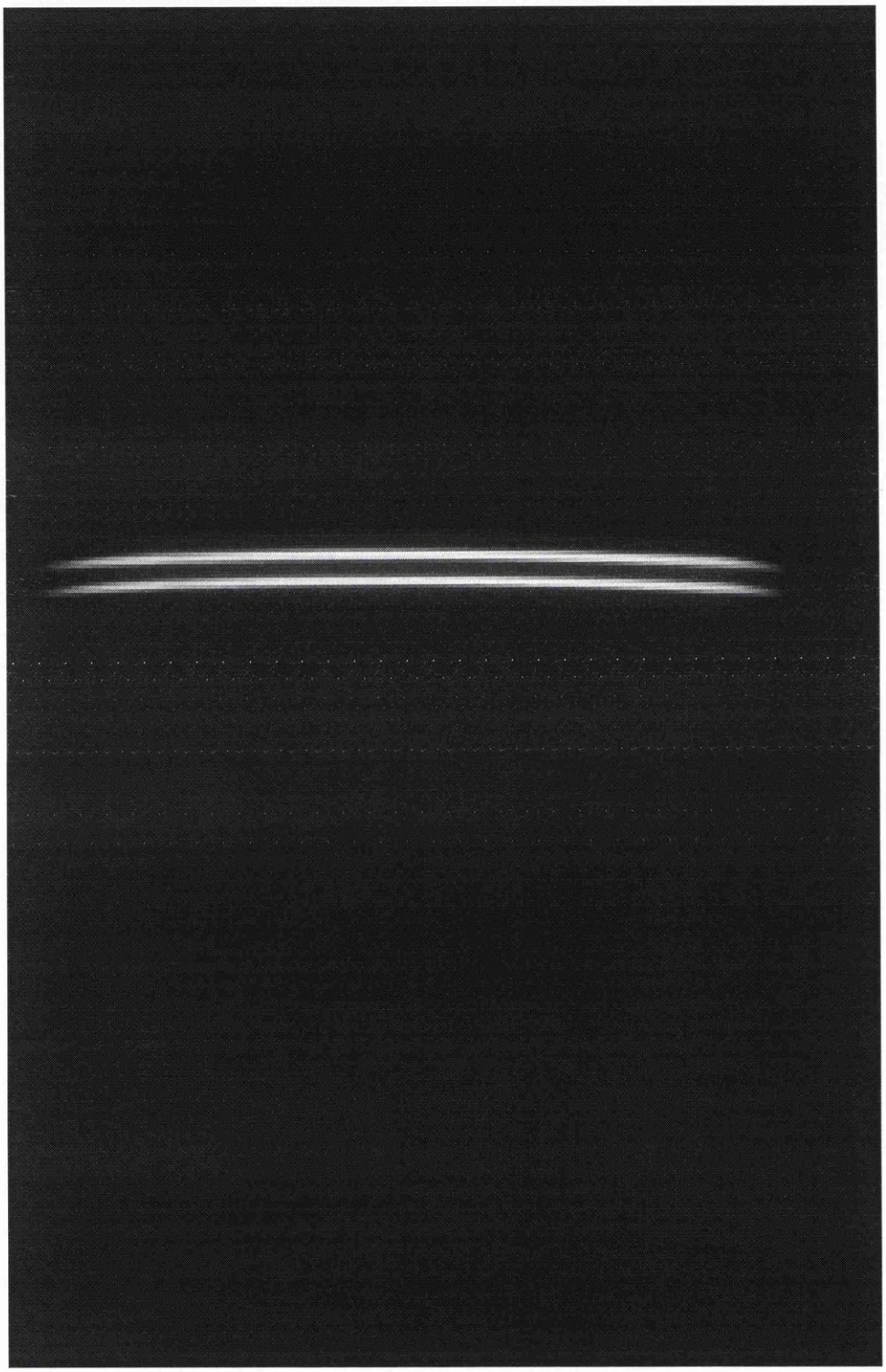

Figure 4.3: CCD image of the Sodium D lines for alignment purposes.

The gear system of the half-wave plate was successively rotated from 0^o (S_0) to 30^o (S_{30}) and 60^o (S_{60}) and images read out. The dark images were also obtained at the beginning and at the end of each set of rotations. A typical exposure times needed to achieve a good signal was 30 seconds. Also added to this, few tens of seconds for reading and downloading the images. Consequently for a single spectropolarimetric map a total of 5-6 minutes were required.

This type of observation introduces a minor problem. Since, the images (S_0, S_{30} and S_{60}) are obtained at several different time intervals (although the exposure times are kept constant all through the experiment), it is not possible to combine these images for polarimetric purposes. For example image S_{30} is always obtained a minute later than S_0 and likewise S_{60} in recorded a minute after S_{30} and etc. Unfortunately, the Sun's position changes (hence intensity) as the successive images are recorded. Therefore an analysis routine had to be developed to take this into account.

4.4 Method of Data Reduction

The data reduction procedure is summarized in Figure 4.4. Each CCD Frame provides pixels which are identifiable by rows, i, corresponding to discrete wavelength positions and columns, j, parallel to the height of the slit. Brightness measurements for each pixel from the polarimetric cycle, may be represented by $S_{ij0}(t_0)_k$, $S_{ij30}(t_{30})_k$ and $S_{ij60}(t_{60})_k$ corresponding to the mean time $(t_0)_k$, $(t_{30})_k$, $(t_{60})_k$, at which the three frames of the k^{th} cycle were taken.

Using STARLINK software collection, specifically FIGARO, KAPPA and SPECDRE, several C-shell scripts were written to analyze these images according to their time (t).

The order in which these scripts operated are as follows;

- Converting the FITS images into NDF.
- Dark image subtracted from each source image.

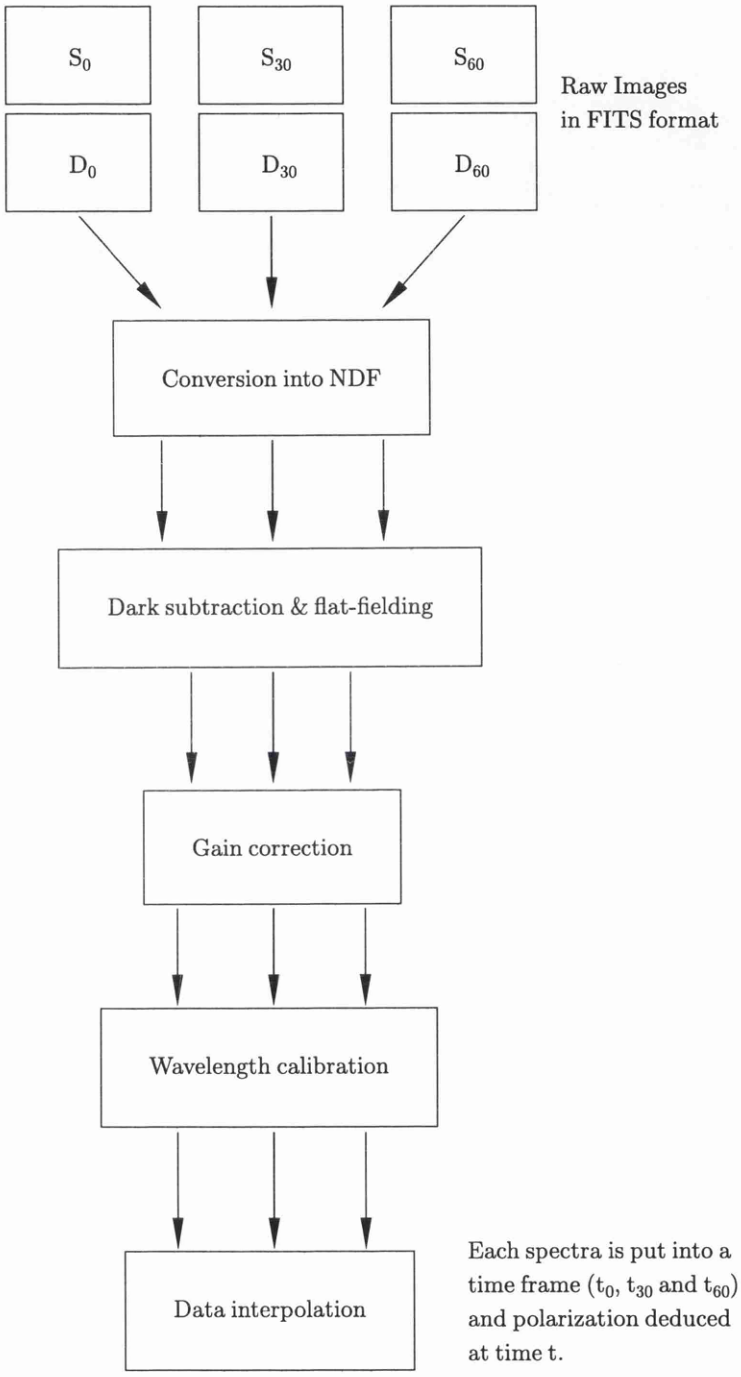

Figure 4.4: Flow chart of the procedure used to analyze the data.

- Each image is flat fielded.
- Pixel columns were added together.
- Each image was calibrated for wavelength.
- The three images are time tagged.

4.4.1 Dark subtraction

Dark images were obtained throughout the observing period. In all cases two dark images per set of half-wave plate rotations. These dark images were added together and a mean value of the pixels were subtracted from the set spectral Images.

4.4.2 Flat-Fielding and Vignetting Correction

It can be seen that by the virtue of p being a normalized parameter, its calculation does not require knowledge of the individual pixel response factor, $\mathcal{G}$. In order to investigate the true photometric behaviour of the Fraunhofer line profiles, however, the relative responses of the pixels do need to be known.

Non-uniformaties on a CCD chip can be as much as few percent for the most modern devices. This multiplicative error is in principle completely removable by division with a picture of uniformly illuminated surface (commonly referred to as flat field), in the process known as flat-fielding. It is possible to do this with very high accuracy. It is common to also incorporate any spatial vignetting (shadowing) from the instrument into the flat-field, although this arises from a source physically distinct from Quantum Efficiency differences.

A sensitivity pattern is wavelength dependent. This is a severe limit on the effectiveness of flatfielding, however, this difficulty does not occur in CCD spectroscopy, since the flat-field exposure is dispersed in the same way as the sky exposure.

The flat-field division should be relatively straightforward, the raw image data is divided pixel for pixel by the flat field image. In practice, this may be acceptable for image data,

but there are additional considerations to be taken into account when the data involved is spectral.

Essentially the main problem with spectral flat fields is that the flat field data will usually vary in X, not because of the instrumental response, but simply because of the spectral response of the fiat field lamp. The usual way of dealing with this is to fit this spectral response (collapsing the fiat field in Y) and then multiplying by the fitted value before dividing by the flat-field. Another way to look at this is to consider the result of dividing the flat field by the fit to the spectral response. The result would be an image which is essentially flat in X, but which is 'humped' in Y (since most flat fields fall off at the edges in Y due to instrumental vignetting. Dividing by this (in a 2D manner) will give us images where the pixel to pixel variations in the detector have been corrected, along with any spatial vignetting of the instrument, but where the overall wavelength response of the instrument is not corrected.

The flat-field image was taken by using a tungston lamp. A defuser was placed in front of the tungston lamp. Image of the defuser was then collimated and placed on the instrument. The image of the defuser was formed on to the spectrometer slit. Figure 4.5 shows the flat-field image over the whole of the CCD chip. We can also see that there is a severe vignetting (when the intensity of the image decreases rapidly away from the centre of the CCD) which has to be corrected for. Care was taken to ensure that the optical geometry of the flat-field exposure was identical to that of the blue sky spectrum. As it was seen only the middle portion of the CCD chip was used for our analysis. The final image size was 120 $\times$ 50 pixels.

The general recipe adapted for the flat-field correction is as follows;

- A mean flat-field frame was derived from several independent exposure (during the observations one flat-field exposure was take at the intervals of 1 hour).

$$\overline{FLAT}_{i,j} = \frac{1}{N}\sum_{K=1}^{M} FLAT_{i,j} \ , \tag{4.7}$$

  where M is number of fiat field images taken.

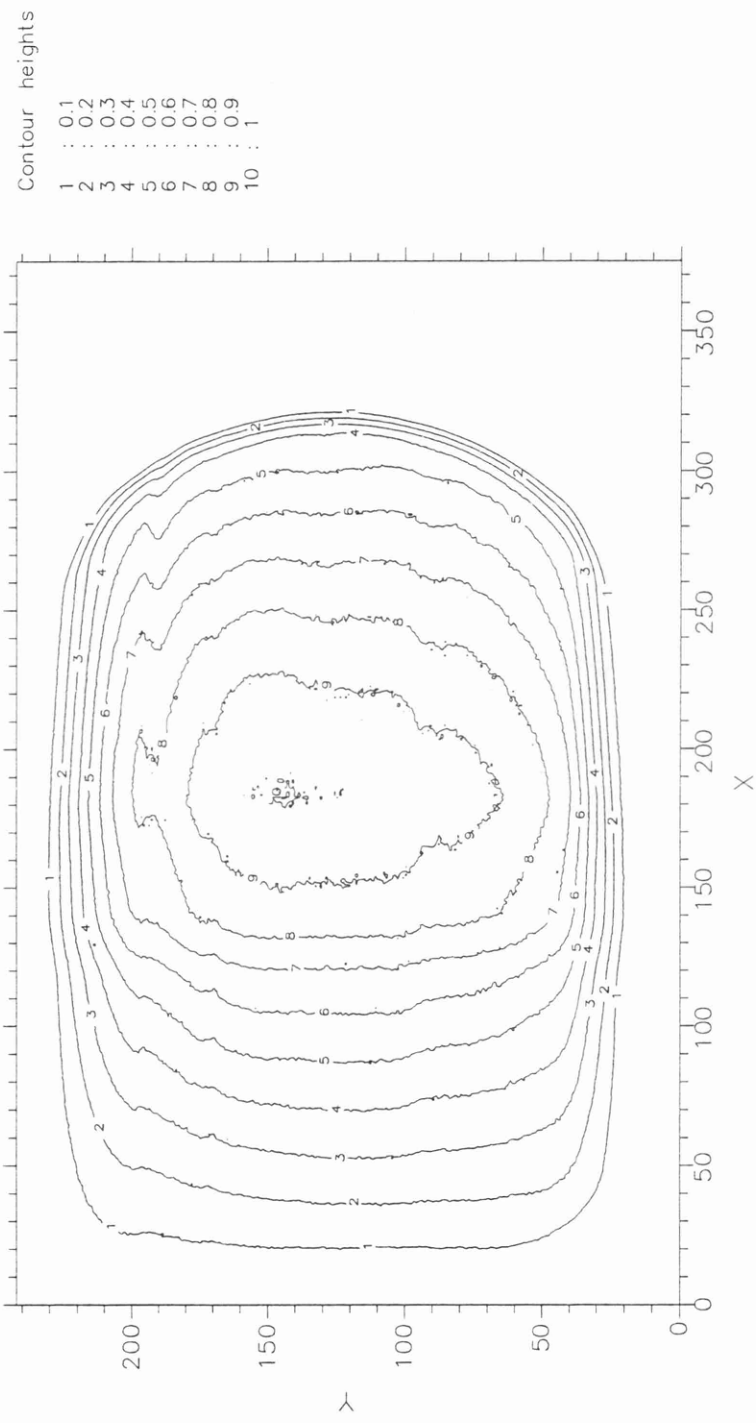

Figure 4.5: The contour map of the Flat-field image and optical vignetting.

- The background exposure was then subtracted from the raw flat field images:

$$FLAT_{i,j} = \overline{FLAT}_{i,j} - DARK_{i,j} \ . \tag{4.8}$$

- The fiat-field frame was then scaled to a mean of unity. Since one doesn't usually want to divide the observed data by the very large numbers found in the flat-field.

- The flat field image was collapse in Y to give a single spectrum. This being the average spectral response of the flat field lamp combined with that of the detector. This is shown in the Figure 4.5.

$$FF_i = \frac{1}{N}\sum_{j=1}^{N} FLAT_{i,j} \ . \tag{4.9}$$

- A two order polynomial was fitted to this collapsed image, this will produce smooth spectrum(SFF_i).

- Each of the cross-section of constant Y value in the flat field was divided by the smoothed spectrum. The result is the corrected flat field calibration image.

$$CALBFF_{i,j} = \frac{FLAT_{i,j}}{SFF_i} \tag{4.10}$$

- The observed image spectra was then divided pixel for pixel by the flat field calibration image.

$$CORRIMAGE_{i,j} = \frac{IMAGE_{i,j}}{CALBFF_{i,j}} \tag{4.11}$$

The program was useful for the correction of the sensitivity response of the CCD pixels and the vignetting due to the optics. The Spectra ($CORRIMAGE_{i,j}$) is now ready for the final reduction.

4.4.3 1-D Spectra

The signal-to-noise ratios of the brightness measurements at the wavelength positions corresponding to each i^{th} value were improved by combining the data along the length of

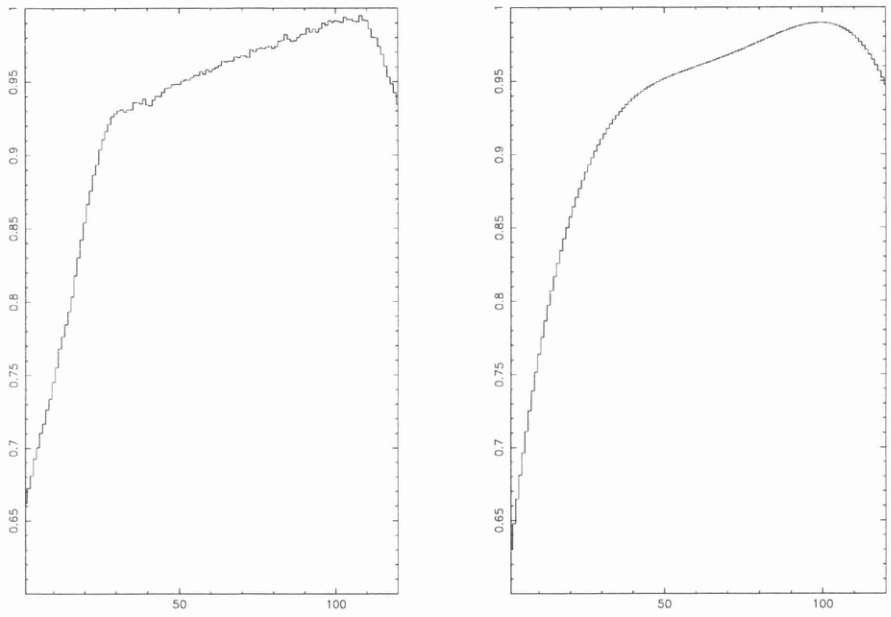

(a) Collapsed in Y

(b) Polynomial Fit

Figure 4.6: a) is the collapsed flat field in Y and b) is the Polynomial fit to this collapsed image(a).

the slit image. For a spectrum height of N pixels, the point wavelength brightness values may therefore be designated by

$$\sum_{j=1}^{N} S_{ij0}(t_0)_k, \sum_{j=1}^{N} S_{ij30}(t_{30})_k \quad and \sum_{j=1}^{N} S_{ij60}(t_{60})_k \; . \tag{4.12}$$

An example of the CCD frame of the spectrum of scattered light from the zenith sky over the region of Magnesium triplet is displayed in Figure 4.7 with a superimposed smoothed intensity record, obtained from the reduction exercise outlined above.

By converting the i values to the calibrated wavelength scale and by applying interpolation within the time series of measurements corresponding to $\alpha = 0^o$, 30^o and 60^o to obtain brightness at singular times, τ, the final values of $S_0(\lambda,\tau)$, $S_{30}(\lambda,\tau)$, $S_{60}(\lambda,\tau)$ ensue, these being used in the calculations of $p(\lambda,\tau)$ and $\psi(\lambda,\tau)$ via Equation 4.3 and 4.4. Photometric profiles $I(\lambda,\tau)$ were produced from the same data by combinations of frames following the scheme summarized by

$$I(\lambda,\tau) \equiv \sum_{j=1}^{N} I_j(\lambda,\tau) \equiv \sum_{j=1}^{N} G_{ij}\{S_{ij0}(t_0)_k + S_{ij30}(t_{30})_k + S_{ij60}(t_{60})_k\} \tag{4.13}$$

where G_{ij} is the flat-fielding correction.

4.4.4 Wavelength Calibration and Polarimetric interpolation

An interpolation program had to be written to handle the spectral data. Several programs were written to obtain the polarization and position angle at a unique time. Figure 4.7 and 4.8 show an example of the magnesium triplet and Hβ spectra at the three position of the half-wave plate. Each set of spectra was ordered with respect to time. The final output image has the time dimension incorporated into the spectra. This program is repeated for each set of observations. Polarization spectra and position angle are obtained by choosing a specific time for each of the intensities $S_0(\lambda,\tau)$, $S_{30}(\lambda,\tau)$ and $S_{60}(\lambda,\tau)$.

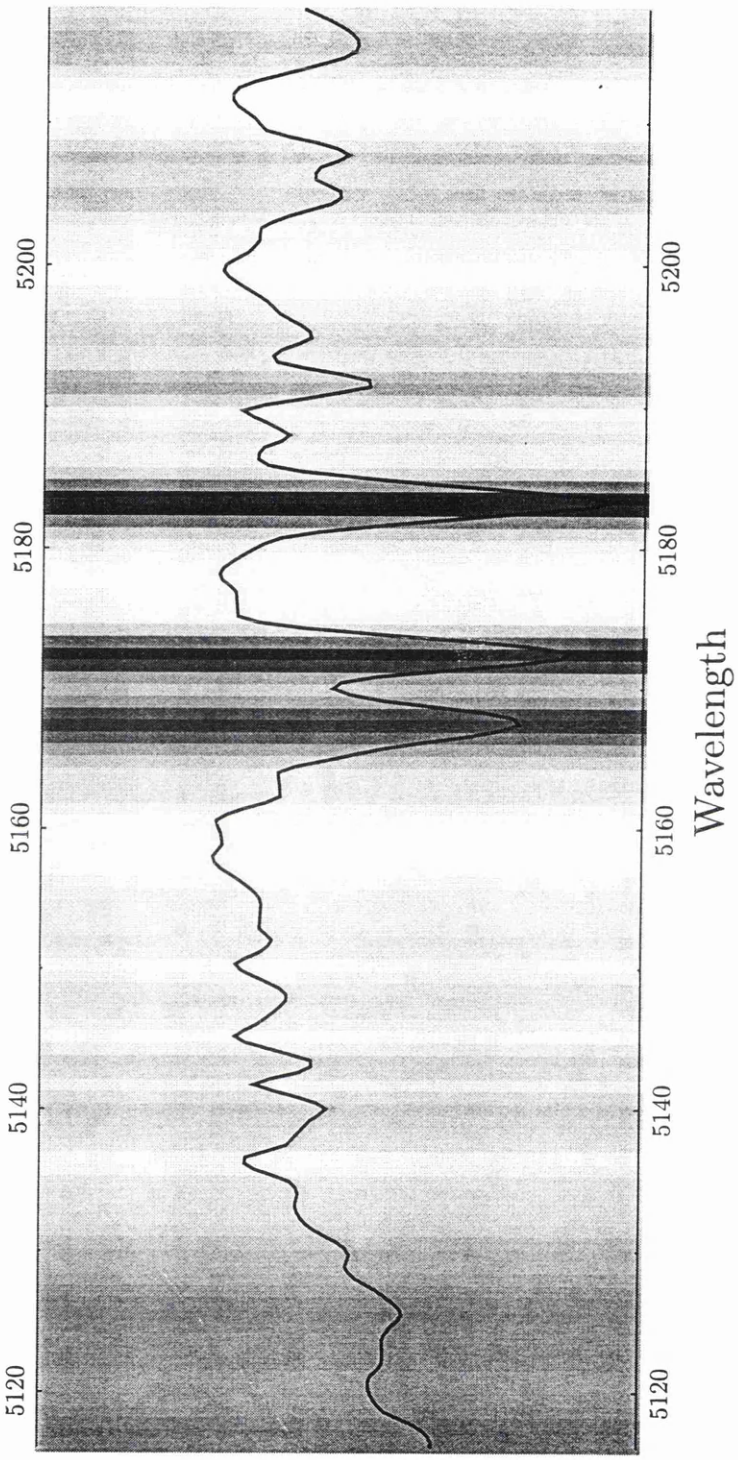

Figure 4.7: This show the 2D image of the spectra of the magnesium lines also superimposed on the image is the profile when the image is collapsed in Y direction.

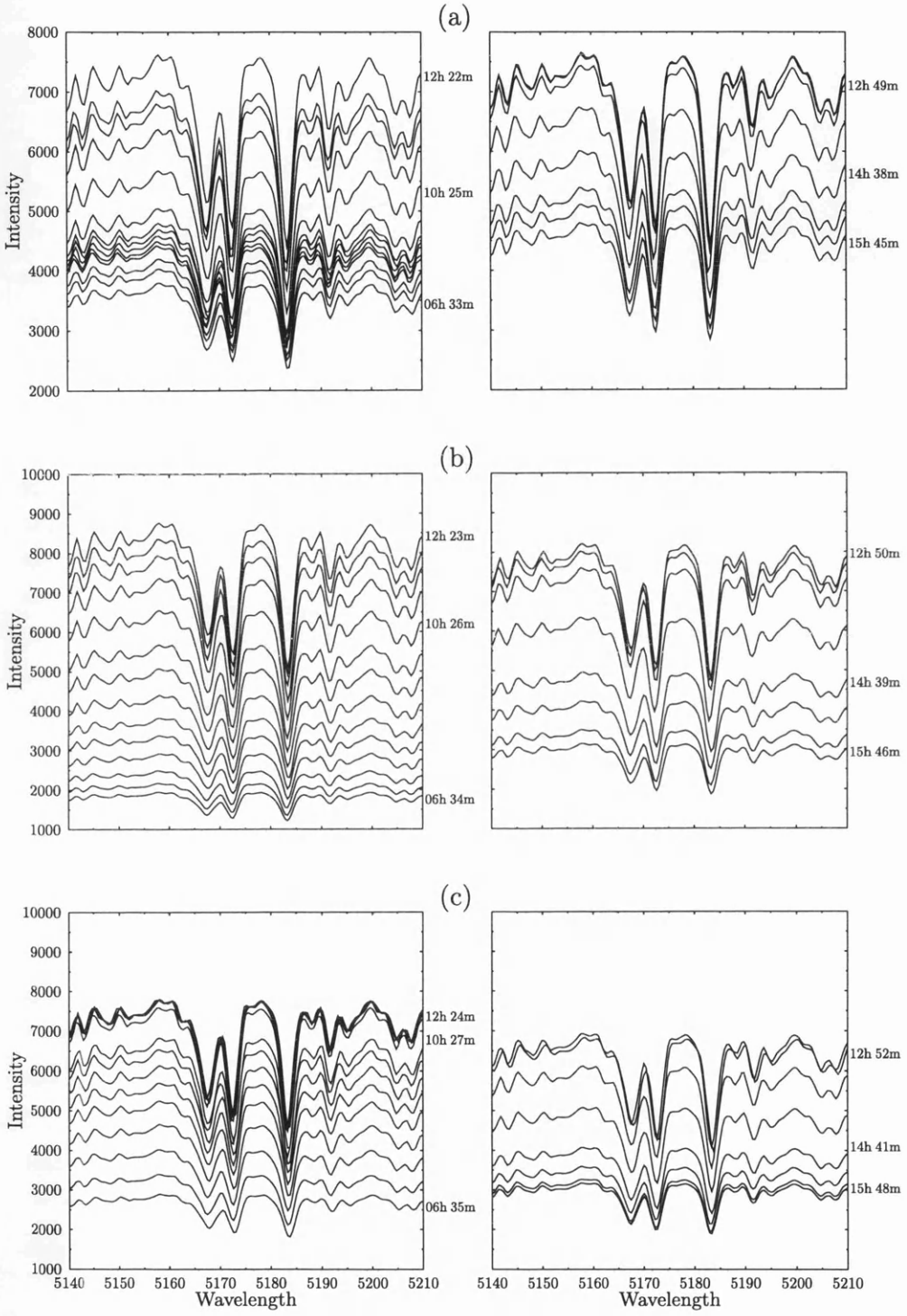

Figure 4.8: Spectra of the magnesium triplet lines at different times of the day at three positions of the $\frac{\lambda}{2}$ plate; **(a)** S_0, **(b)** S_{30} and **(c)** S_{60}.

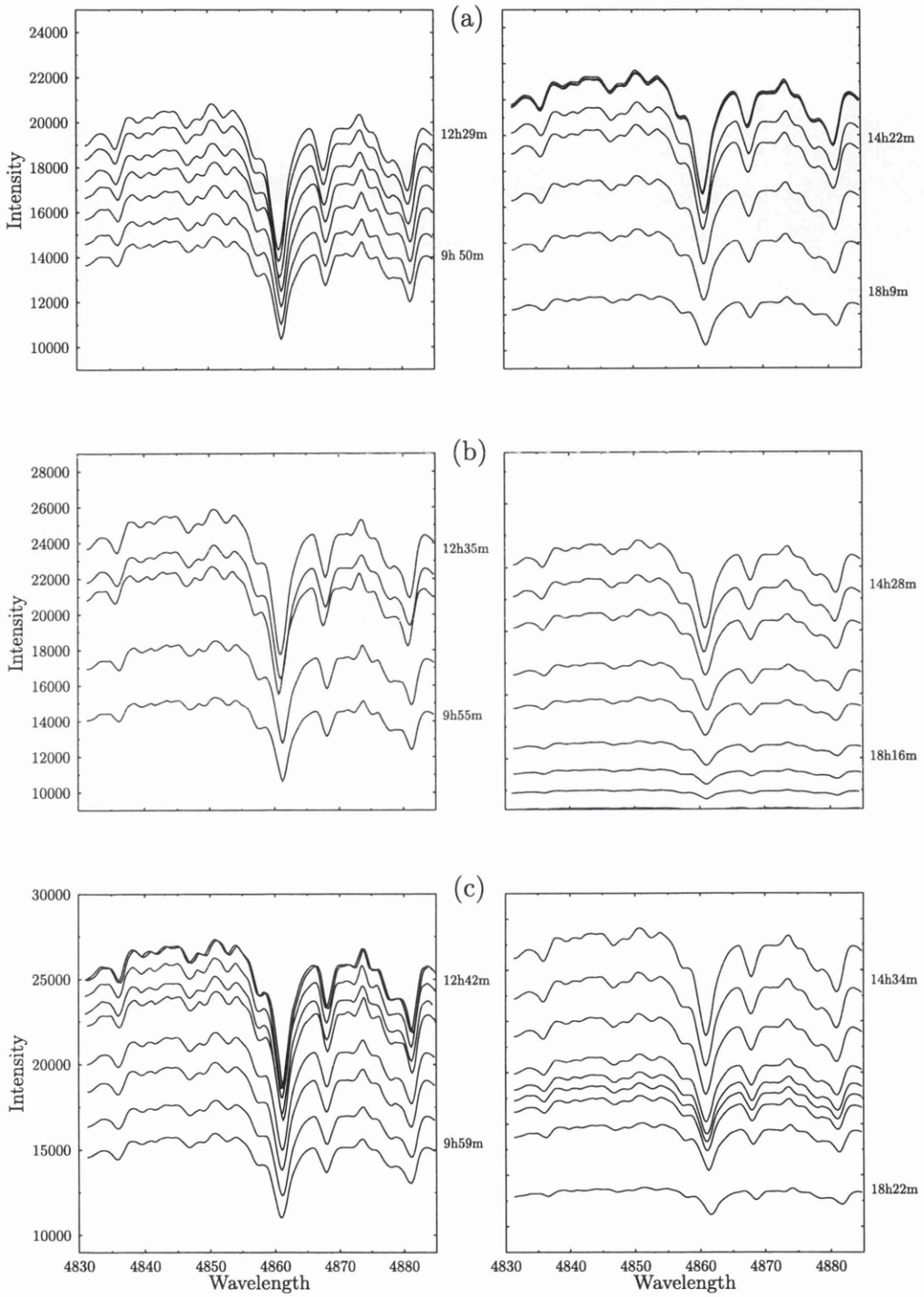

Figure 4.9: Spectra of the Hβ line at different times of the day at three positions of the $\frac{\lambda}{2}$ plate; **(a)** S_0, **(b)** S_{30} and **(c)** S_{60}.

4.4.5 Time Dependent Wavelength Drift

During the analysis of the data, it was noticed that there was a slight drift in the spectrum over the observations. Inspection of the data showed that during the observations the spectrum shifted along the pixel columns. Therefore, the data was scrutinized for any systematic wavelength drifts during the day. A program was written to compare each spectrum with the next and the wavelength displacement was recorded. Figure 4.10 shows the wavelength displacement in Ångstrom for magnesium triplet and the Hβ line. It was also noticed the same spectral drift occurs at the three consecutive images (S_0, S_30 and S_{60}).

There could only be two possibilities for this effect; it could either be an instrumental or diurnal effect. The contribution from diurnal effect will be small, and also the shift in wavelength will be systematic. The shift seems to be random during the day indicating an instrumental effect. The most likely explanation is the CCD head might have moved during the observations. It should be noted that this effect has been calibrated for before the data was analysed.

4.5 Polarimetric Calibration

The spectropolarimeter was tested for its efficiency by using a 100% polarized light. To perform the test a sheet polaroid was placed ahead of the objective lens of the instruments so that only linearly polarized light passed through the entire system. Figure 4.11 shows the result of this calibration. The polarization values ranged from 101.8% to 100.1%, with a mean polarization of 100.2% . This also confirms that the instruments correctly analyzes the polarized light. The polarimetric uncertainty for each resolved spectral point is $\sim \pm 0.005$ and this is sufficient to reveal any time dependent structure affecting the spectra.

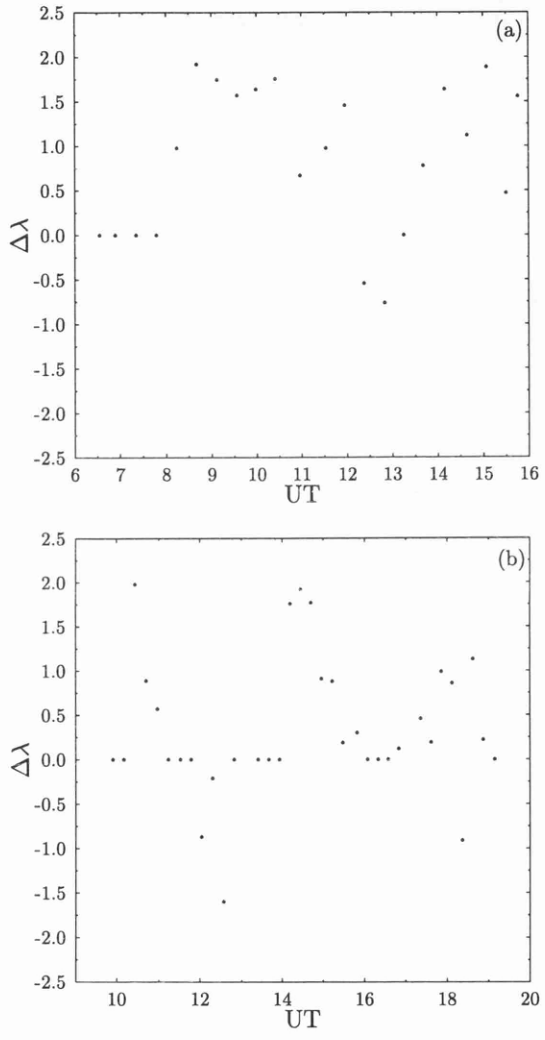

Figure 4.10: Wavelength displacement against time for **(a)** magnesium triplet and **(b)** Hβ. UT is in hours and $\Delta\lambda$ is in Ångstrom.

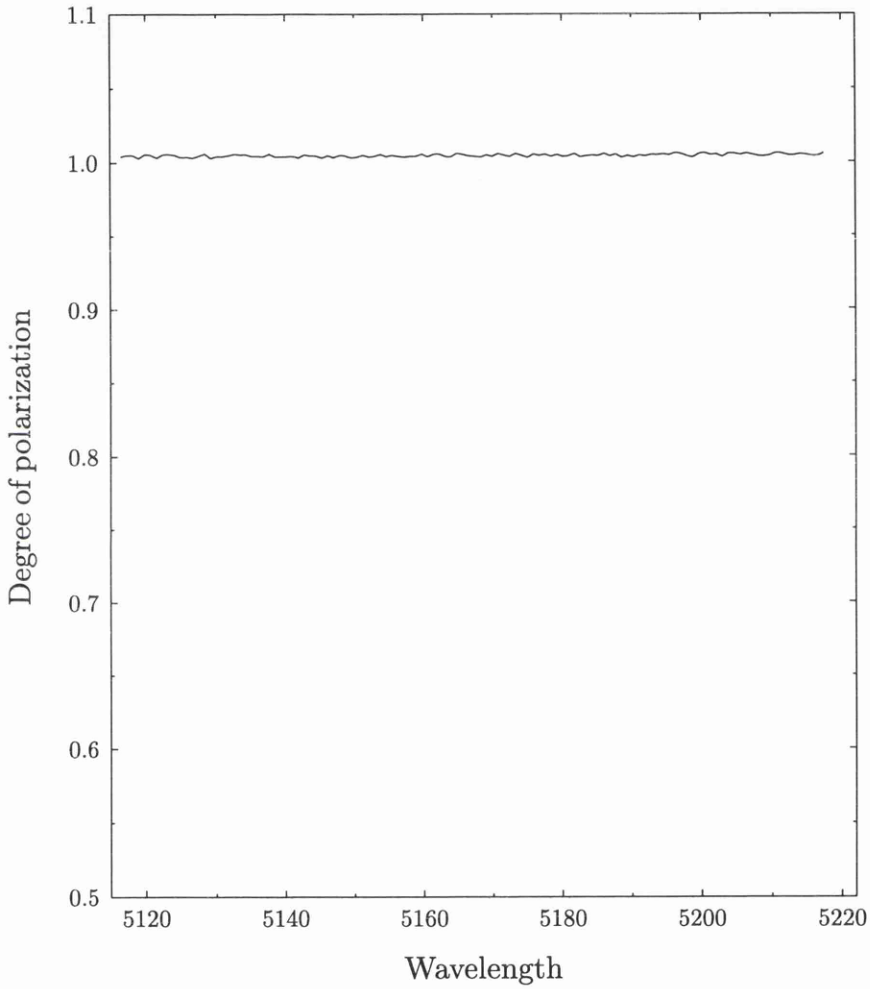

Figure 4.11: Graph of the 100% polarization calibration of the Spectropolarimeter.

4.6 Observational Results

Observations were carried out during 31 August 1993 and 15 May 1994 at the University of Glasgow Observatory. There are two sets of observations presented in this section. The data presented are of two sets of wavelengths, magnesium triplet and Hβ line. Unfortunately, the presented data only covers two days of observations. This was due to adverse weather in Glasgow, since one required absolutely cloudless day for the observations.

4.6.1 Photometric Analysis

Before a polarimetric analysis is carried out, it was deemed necessary to consider the photometric behaviour of the Fraunhofer lines. This analysis would give a valuable insight into the Ring effect.

Initially, each photometric data for S_0, S_{30} and S_{60} were individually scrutinized for any variations of the line depth to the continuum. All the data sets were normalized to the continuum. The ratio of line bottom to continuum were calculated and these are shown in Figures 4.11 and 4.12 From these figures it is apparent that there is no systematic change in the depth of the line to the continuum. This implies that the line depth does not change during the day. Hence in disagreement with the previous observations made by other workers (e.g. Harrison, 1975).

4.6.2 Polarimetric Analysis

A cursory inspection of the data revealed that the polarimetric line measurements, rather than the photometric profiles, were sensitive to the position of the Sun changing markedly through the day. Typical records for the behaviour of $p(\lambda)$ across the spectral region containing the magnesium triplet and Hβ lines are displayed in Figures 4.13 to 4.21 for time intervals of 15 minutes from dawn to sunset. These correspond to a large, to a minimum and to a large phase angle in the scattering plane defined by the position of the Sun, the zenith and the equipment at the base of the zenith column. It can be

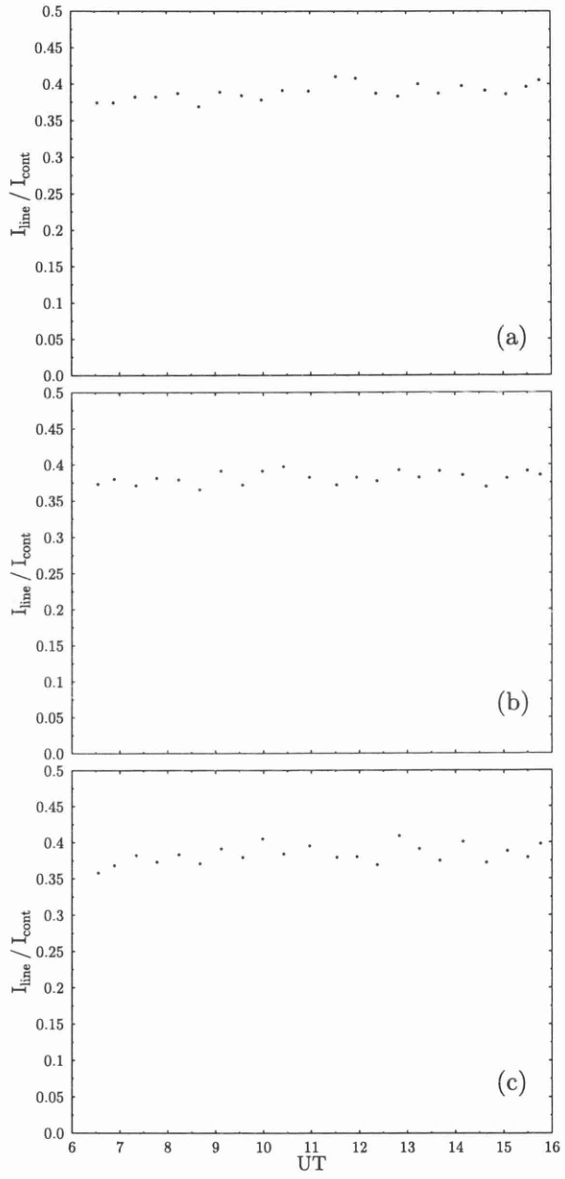

Figure 4.12: Ratio of the continuum to line bottom at three positions of the $\frac{\lambda}{2}$ against time for magnesium triplet lines (5183Å); **(a)** S_0, **(b)** S_{30} and **(c)** S_{60}. UT is in hours.

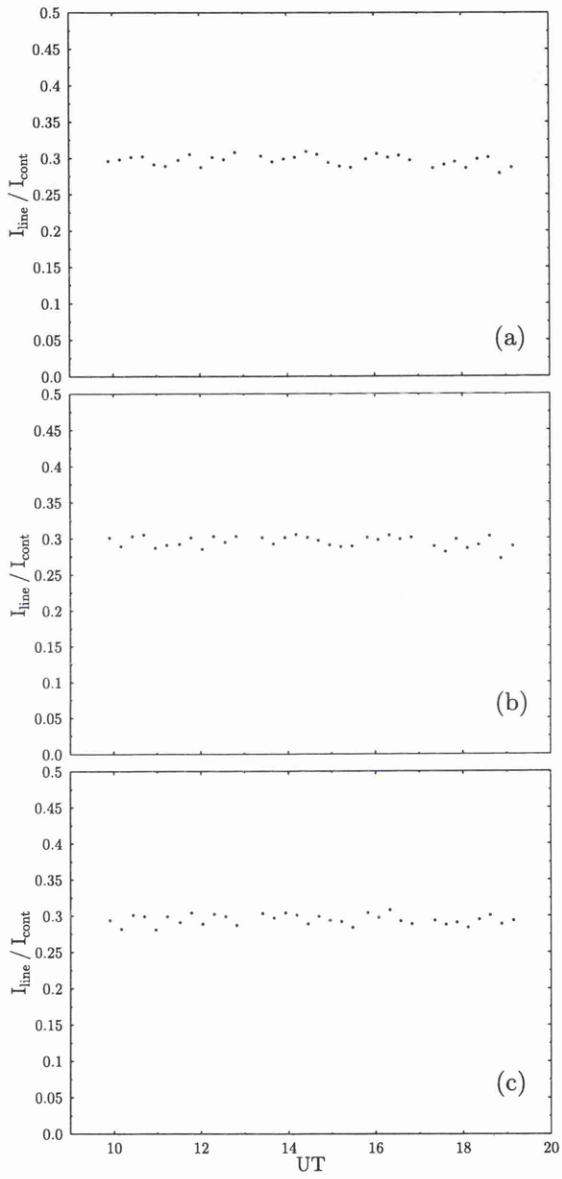

Figure 4.13: Ratio of the continuum to line bottom at three positions of the $\frac{\lambda}{2}$ against time for Hβ lines (4861Å); **(a)** S_0, **(b)** S_{30} and **(c)** S_{60}. UT is in hours.

seen that the "anomalies" of relative polarization between the Fraunhofer lines and the continuum occur most significantly on the blue shoulders of the absorption profiles, and to a lesser extent on the red shoulders for the magnesium triplets. At large scattering angles, the $p(\lambda)$ values first display an enhancement followed by a depression as the line is transversed from shorter to longer wavelengths. At small scattering angles, around noon, the enhancement is more dominant, concentrating more to the centre of the line, followed by a weak depression on the red shoulder. The polarization enhancement at the blue shoulder of the magnesium triplets is $\sim$ 2% larger than the continuum polarization at large scattering angles. When the Sun is at low altitude the continuum polarization is $\sim$0.4(40%) and at higher altitudes the continuum polarization drops to $\sim$0.01(10%).

The diurnal changes of the continuum and an isolated spectral line in the magnesium triplet is shown in Figure 4.23. This clearly shows large variability during low scattering angles.

This kind of behaviour had been noted by Clarke and Basurah (1989) from the monitoring of three wavelength point polarimetry at the line core and embracing continuum positions; the inferior spectral resolution of the equipment used for this previous study would have included a significant amount of radiation from the wings of lines when the monochromator was tuned to the wavelength of the line bottom (see Chapter 1, Figure 1.8). Again from the data of Clarke and Basurah (1989), although not commented on at the time, it may be noted that there are diurnal changes in the polarization differences between the blue and red continua immediately adjacent to the lines, these being seen more clearly in the data here.

Data for Hβ line are displayed in Figures 4.24 to 4.28 for time intervals of 30 minutes. The polarization behaviour of the Hβ line is quite different from that of magnesium triplets. There is no enhancement either on the blue or the red shoulder of the line. However, there is a polarization depression at the line bottom. The significant change occurs during the midday where the line and the continuum levels are the same. It can also be seen that the polarization spectrum becomes more noticeable with time. It can also be gleaned from the data that the position angle for both sets of observations remaines unchanged.

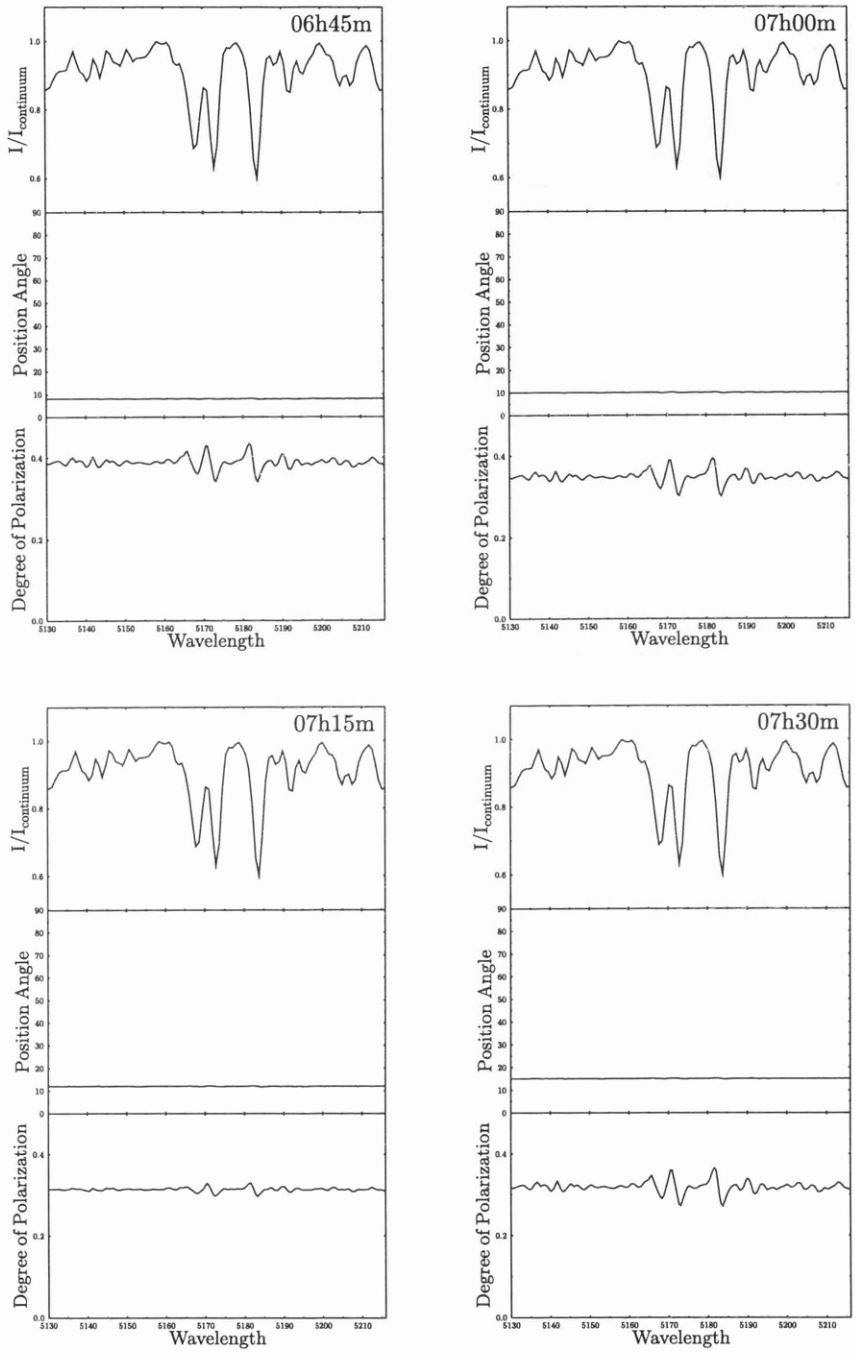

Figure 4.14: Graph of normalized flux, polarization and position angle spectrum for magnesium triplets with time.

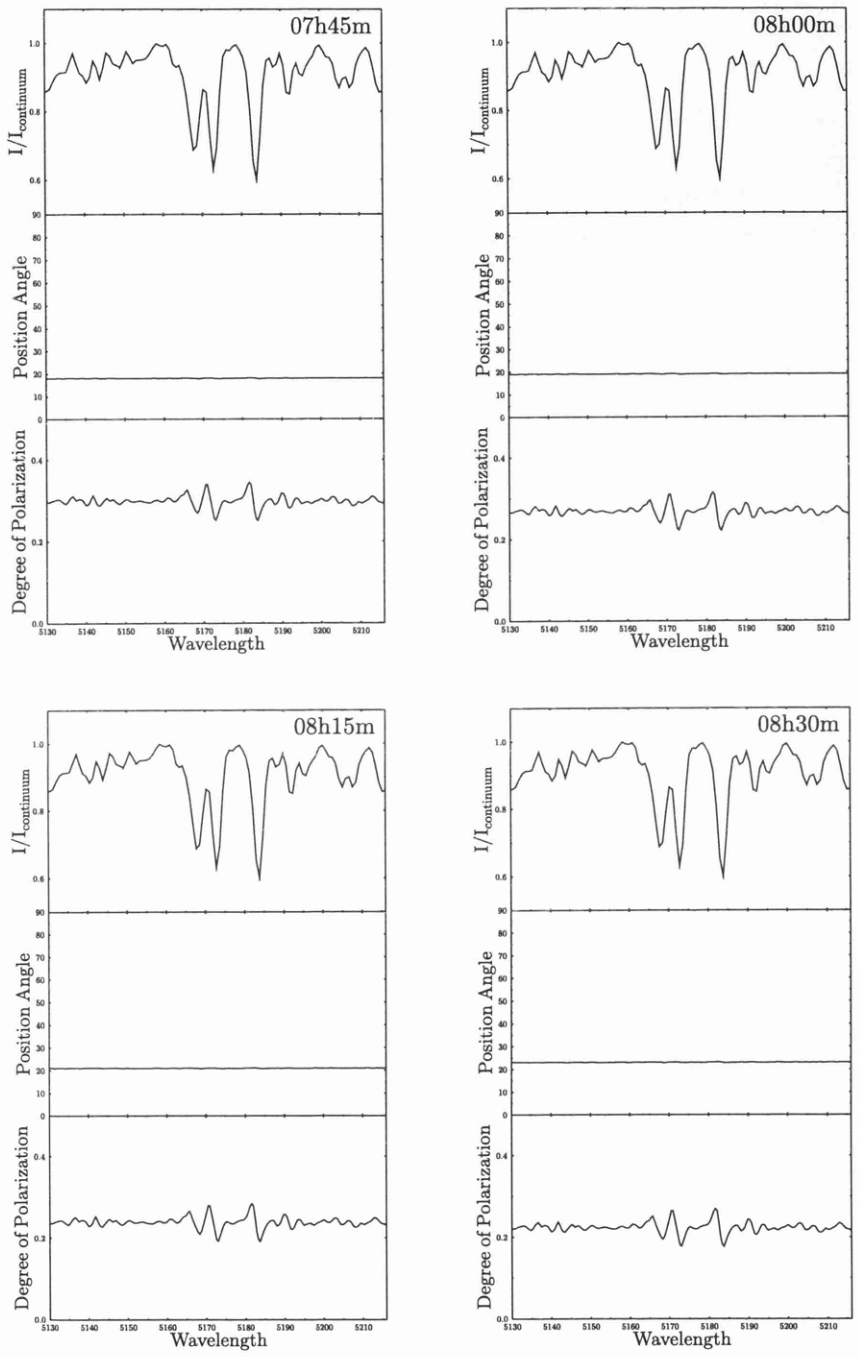

Figure 4.15: Graph of normalized flux, polarization and position angle spectrum for magnesium triplets with time.

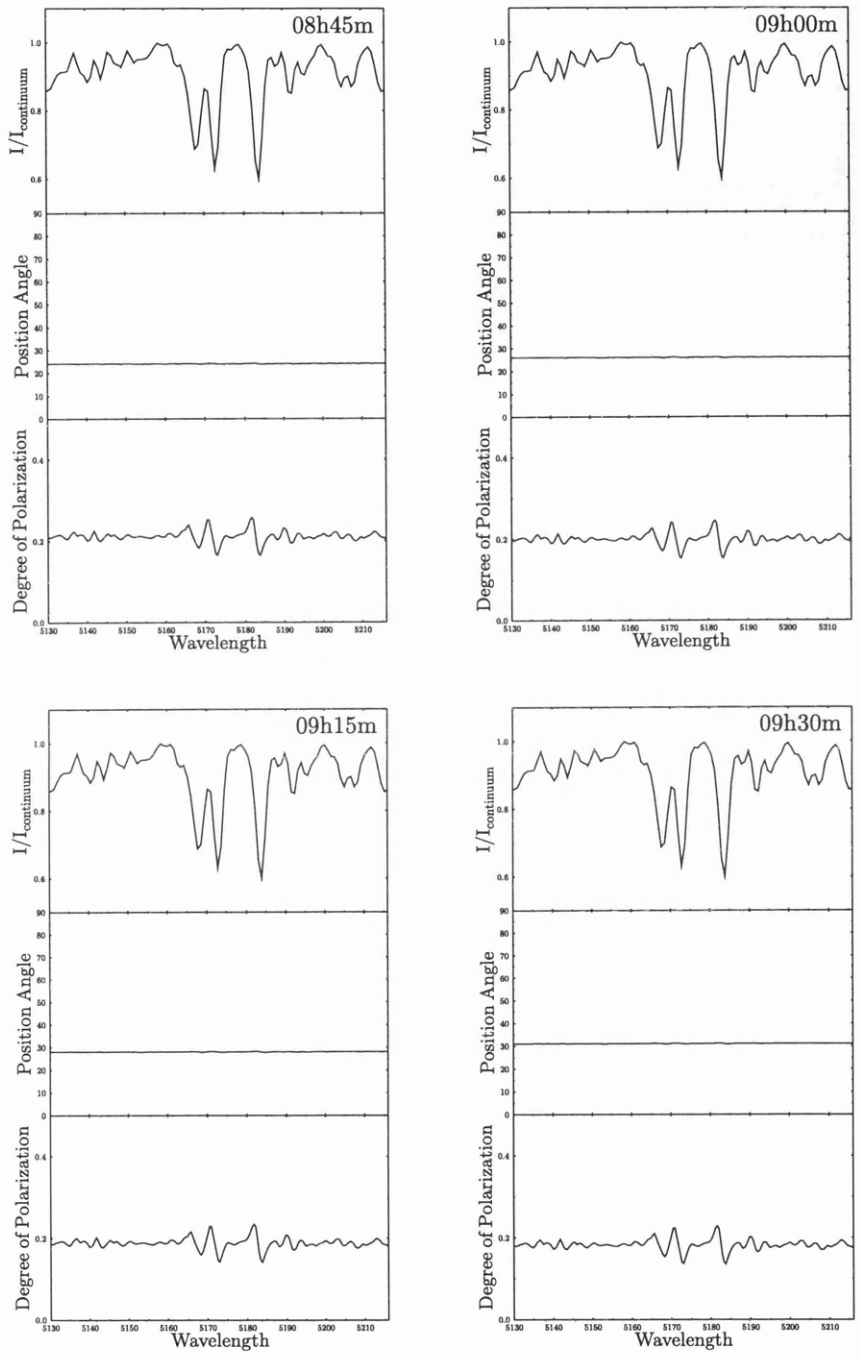

Figure 4.16: Graph of normalized flux, polarization and position angle spectrum for magnesium triplets with time.

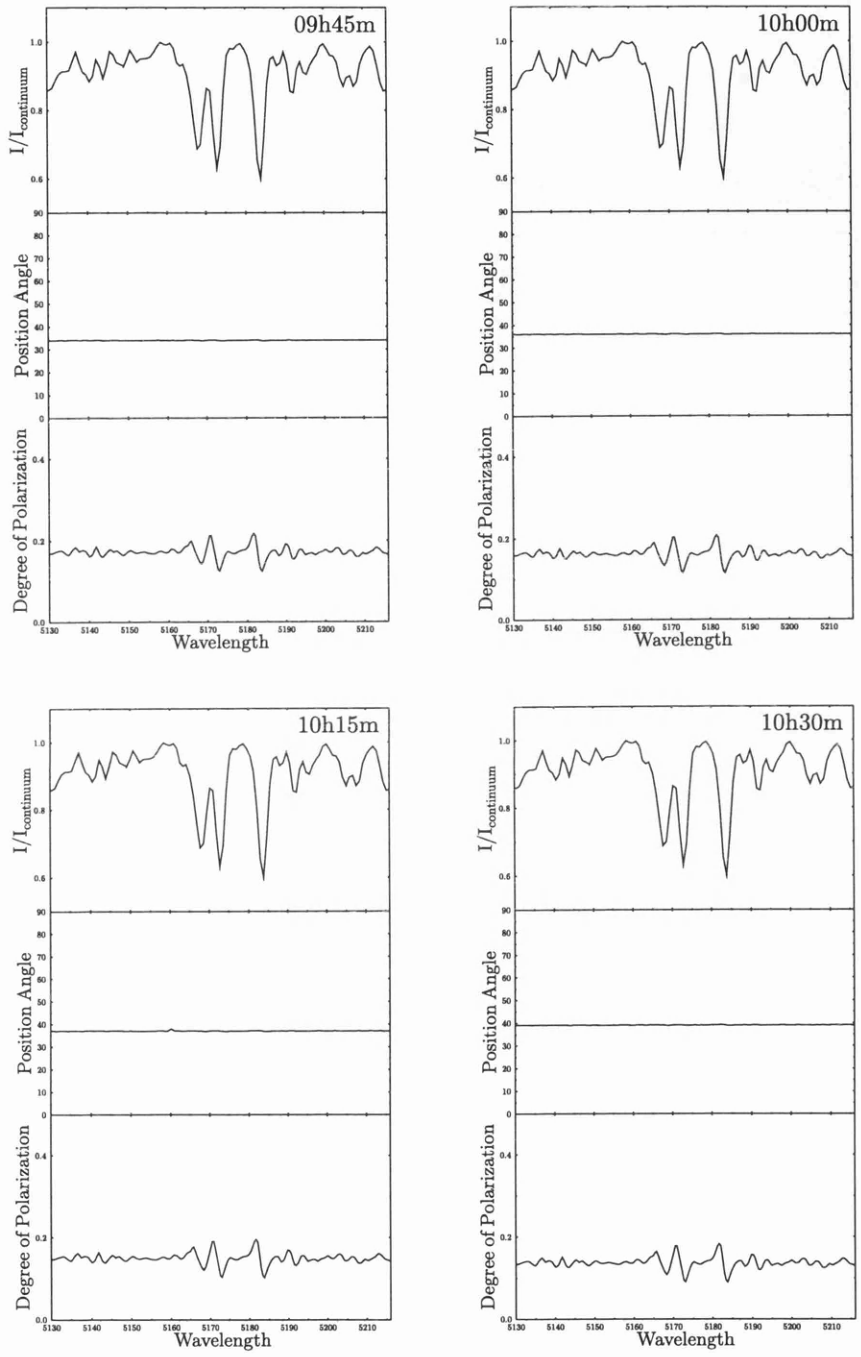

Figure 4.17: Graph of normalized flux, polarization and position angle spectrum for magnesium triplets with time.

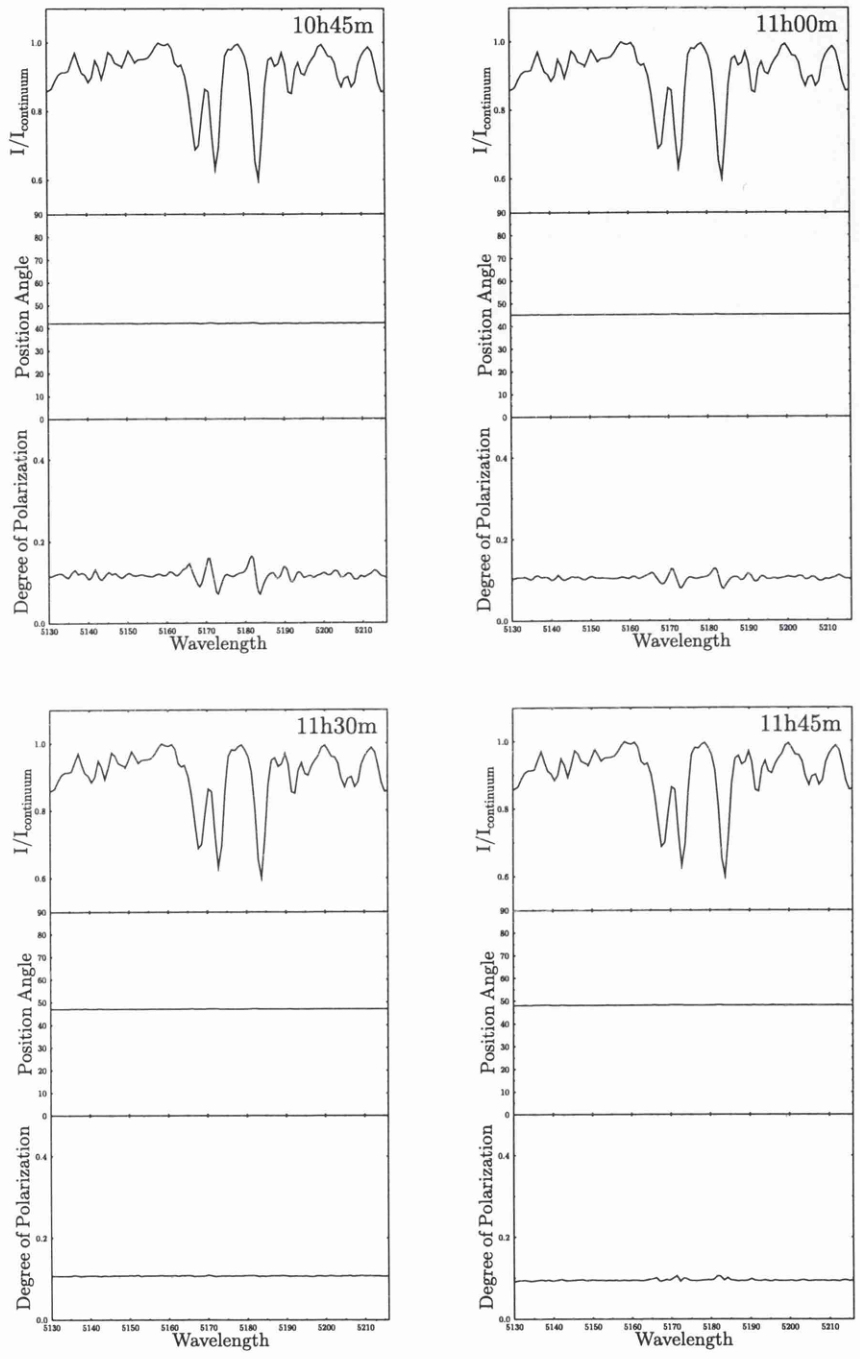

Figure 4.18: Graph of normalized flux, polarization and position angle spectrum for magnesium triplets with time.

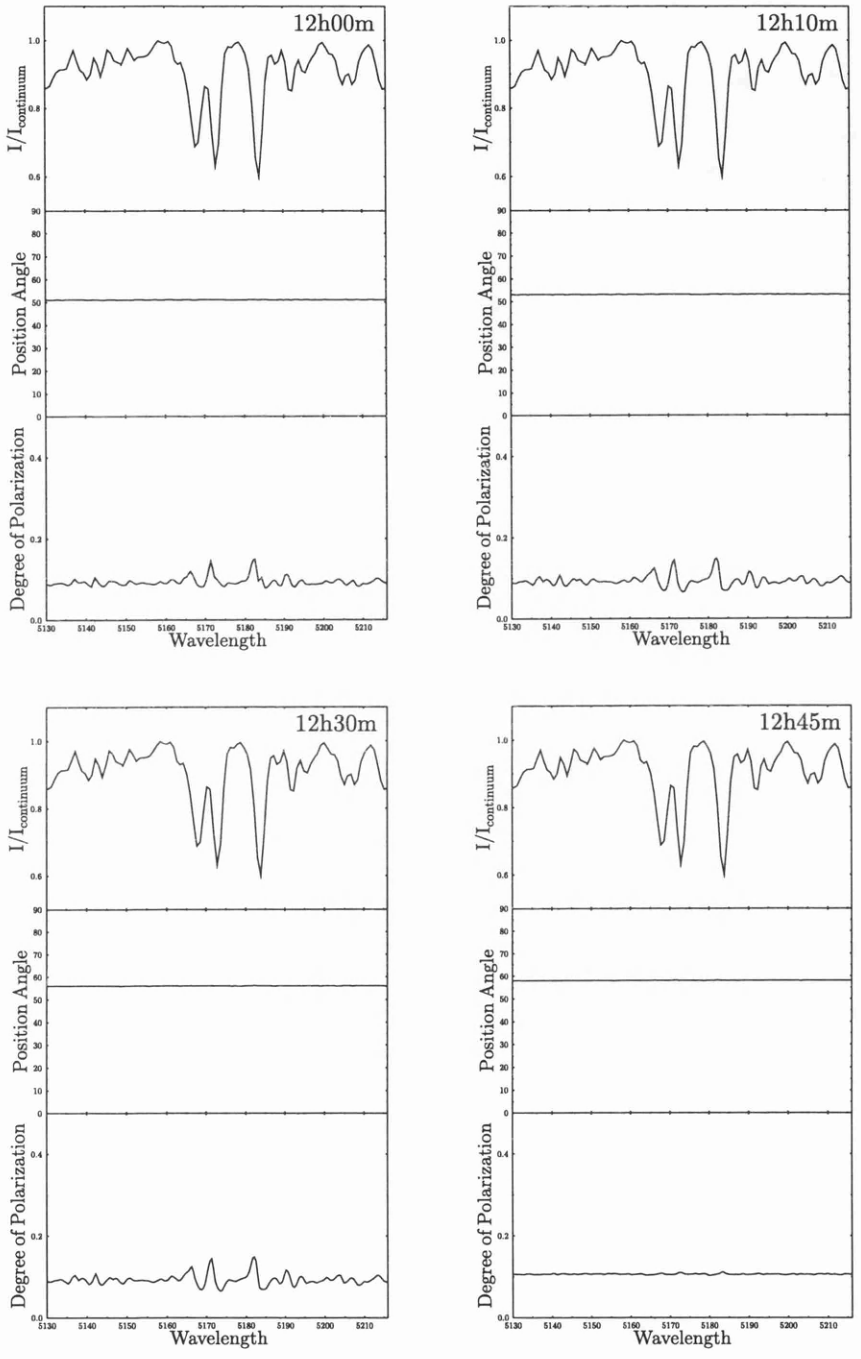

Figure 4.19: Graph of normalized flux, polarization and position angle spectrum for magnesium triplets with time.

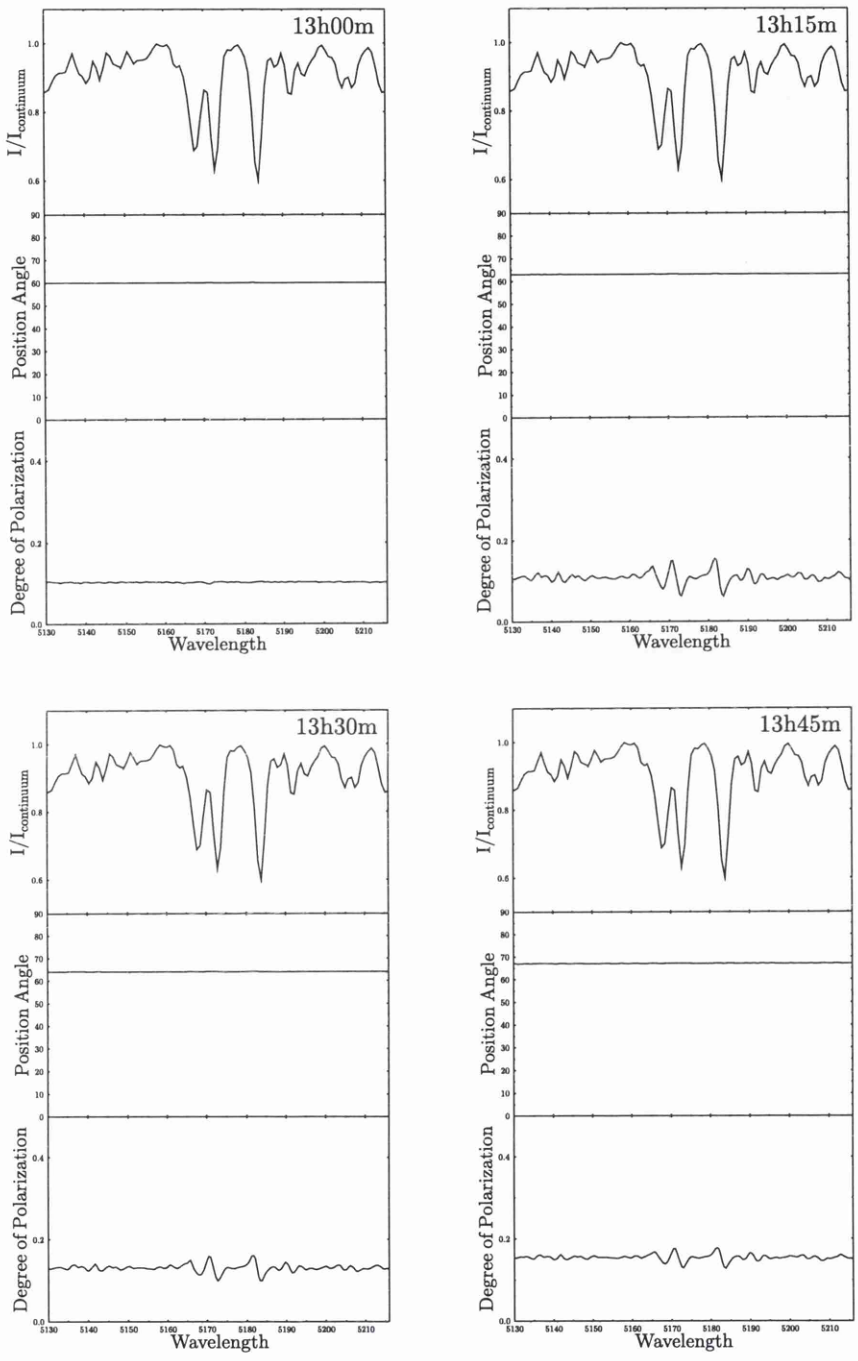

Figure 4.20: Graph of normalized flux, polarization and position angle spectrum for magnesium triplets with time.

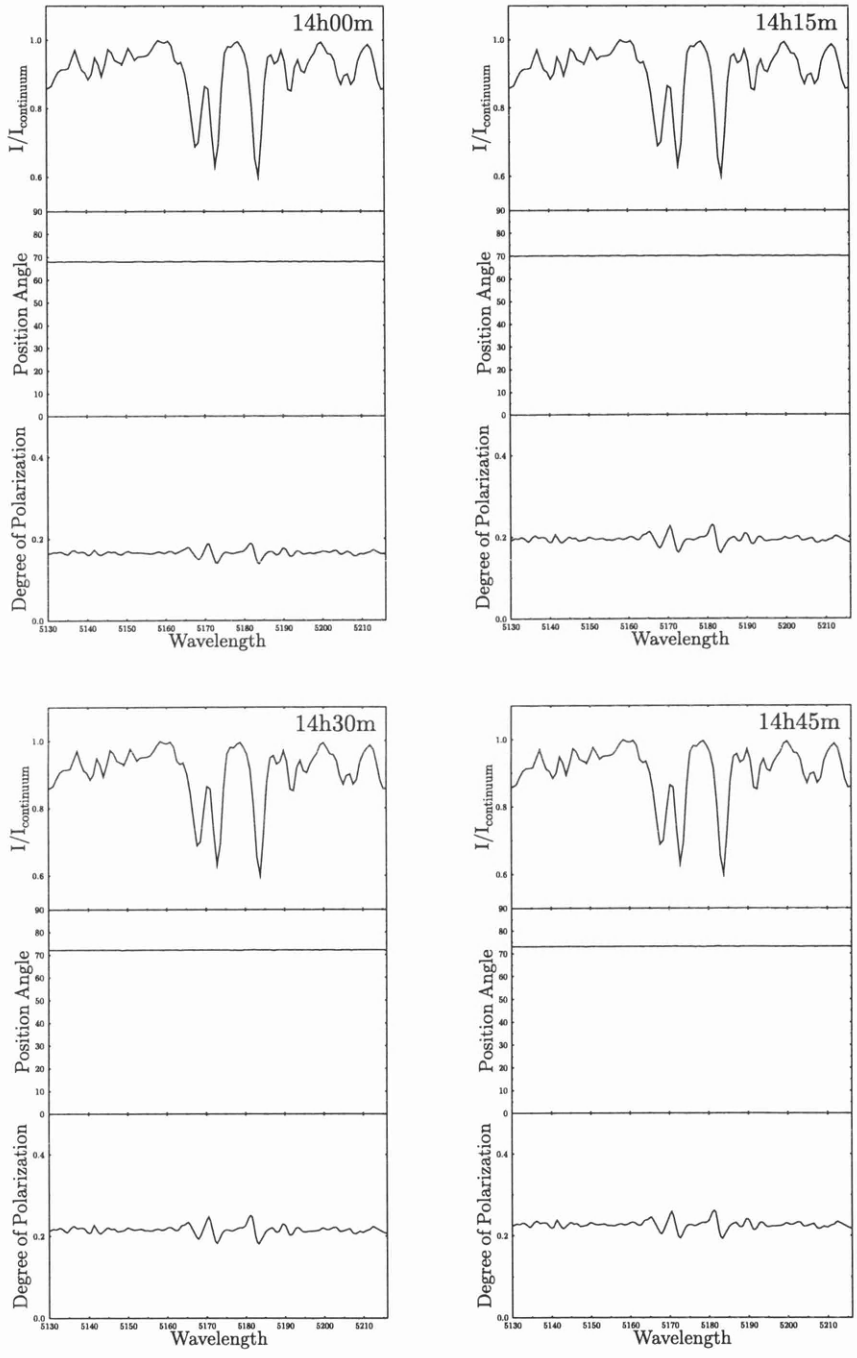

Figure 4.21: Graph of normalized flux, polarization and position angle spectrum for magnesium triplets with time.

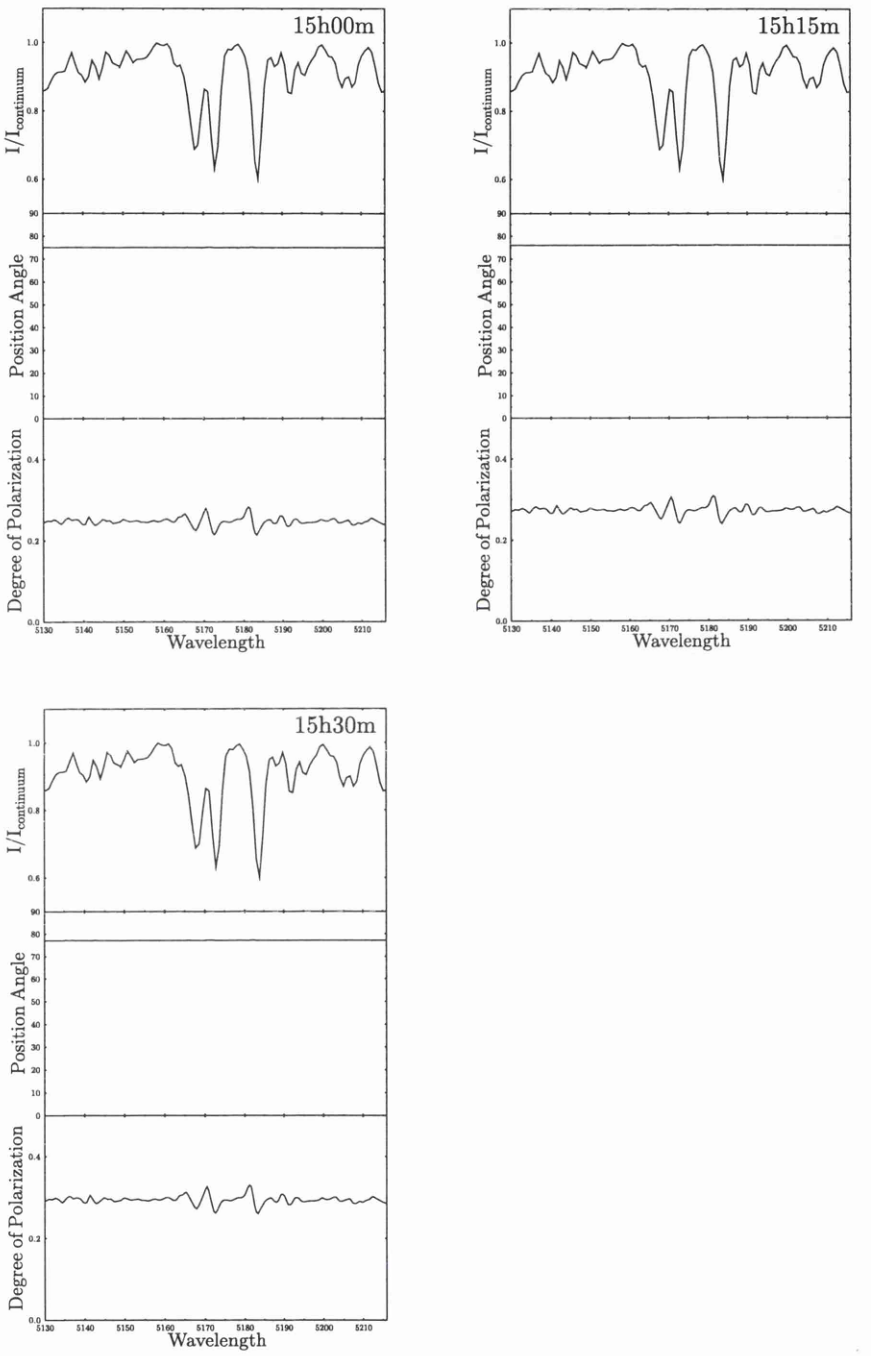

Figure 4.22: Graph of normalized flux, polarization and position angle spectrum for magnesium triplets with time.

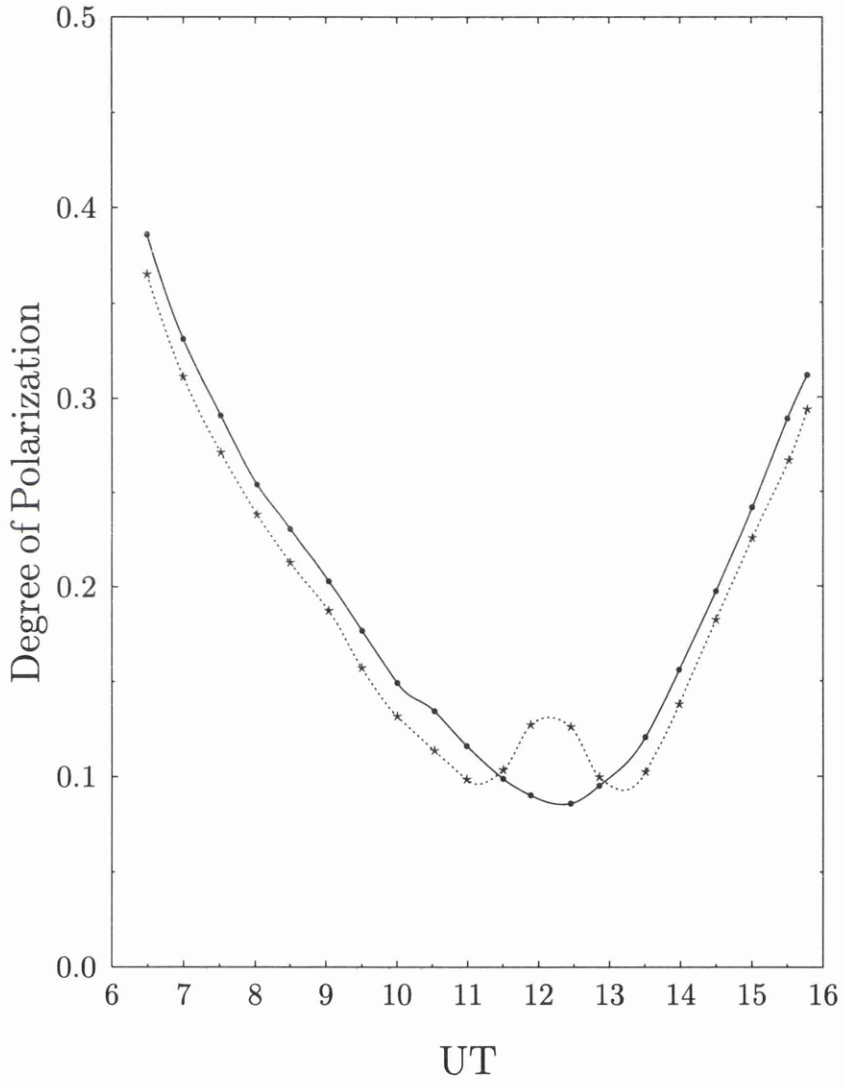

Figure 4.23: Diurnal change in polarization at the continuum (•) and an isolated line ($\star$) within the Magnesium triplets.

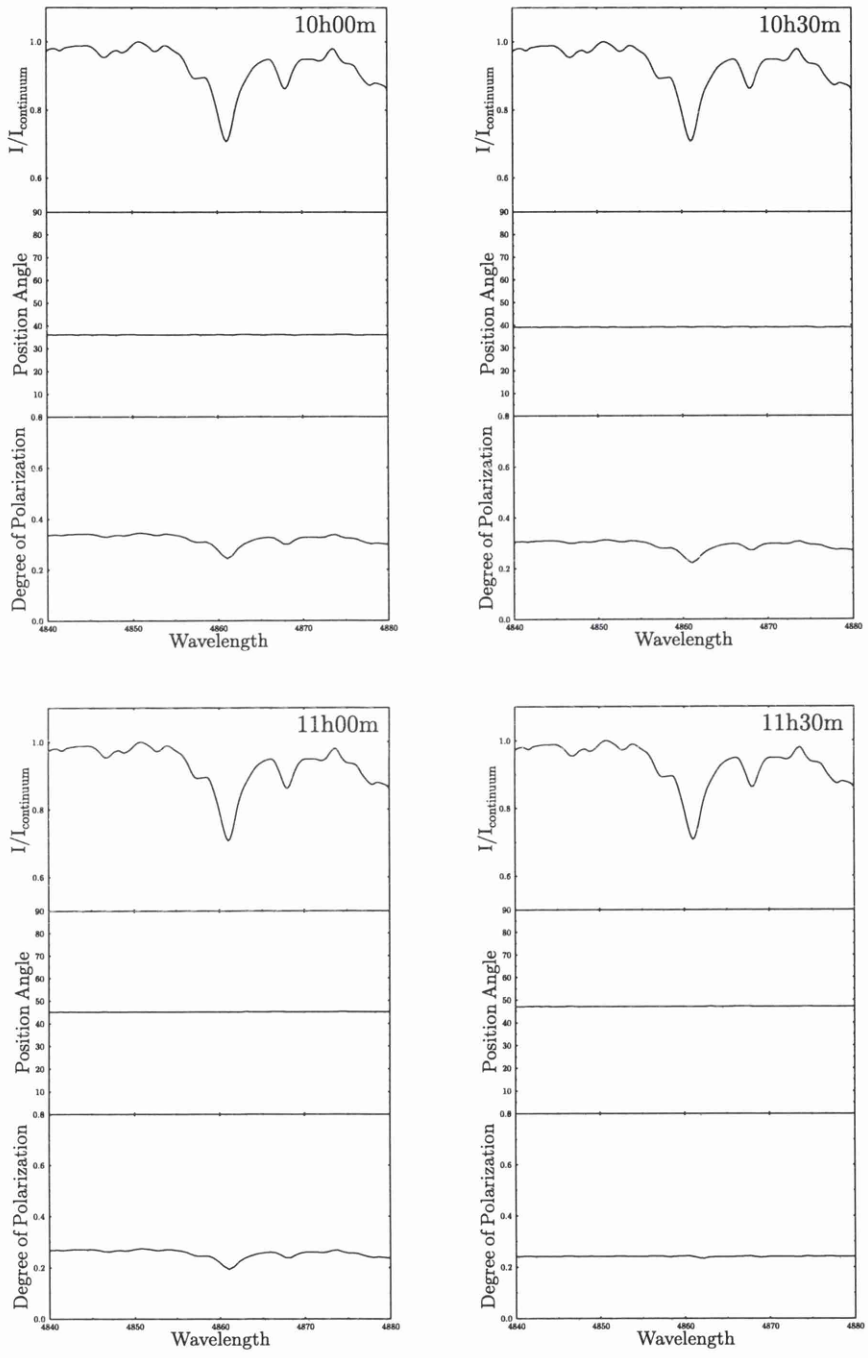

Figure 4.24: Graph of normalized flux, polarization and position angle spectrum for Hβ with time.

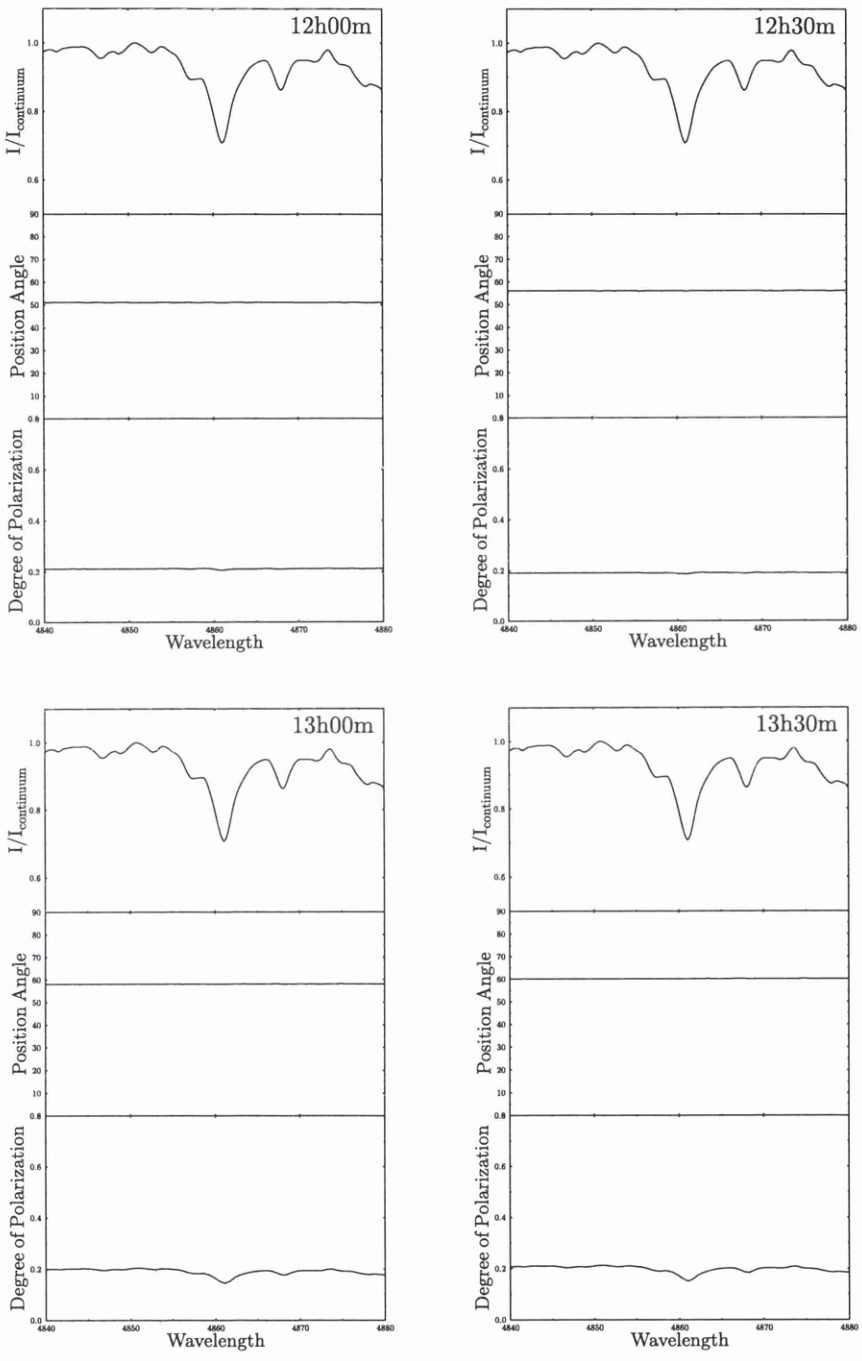

Figure 4.25: Graph of normalized flux, polarization and position angle spectrum for Hβ with time.

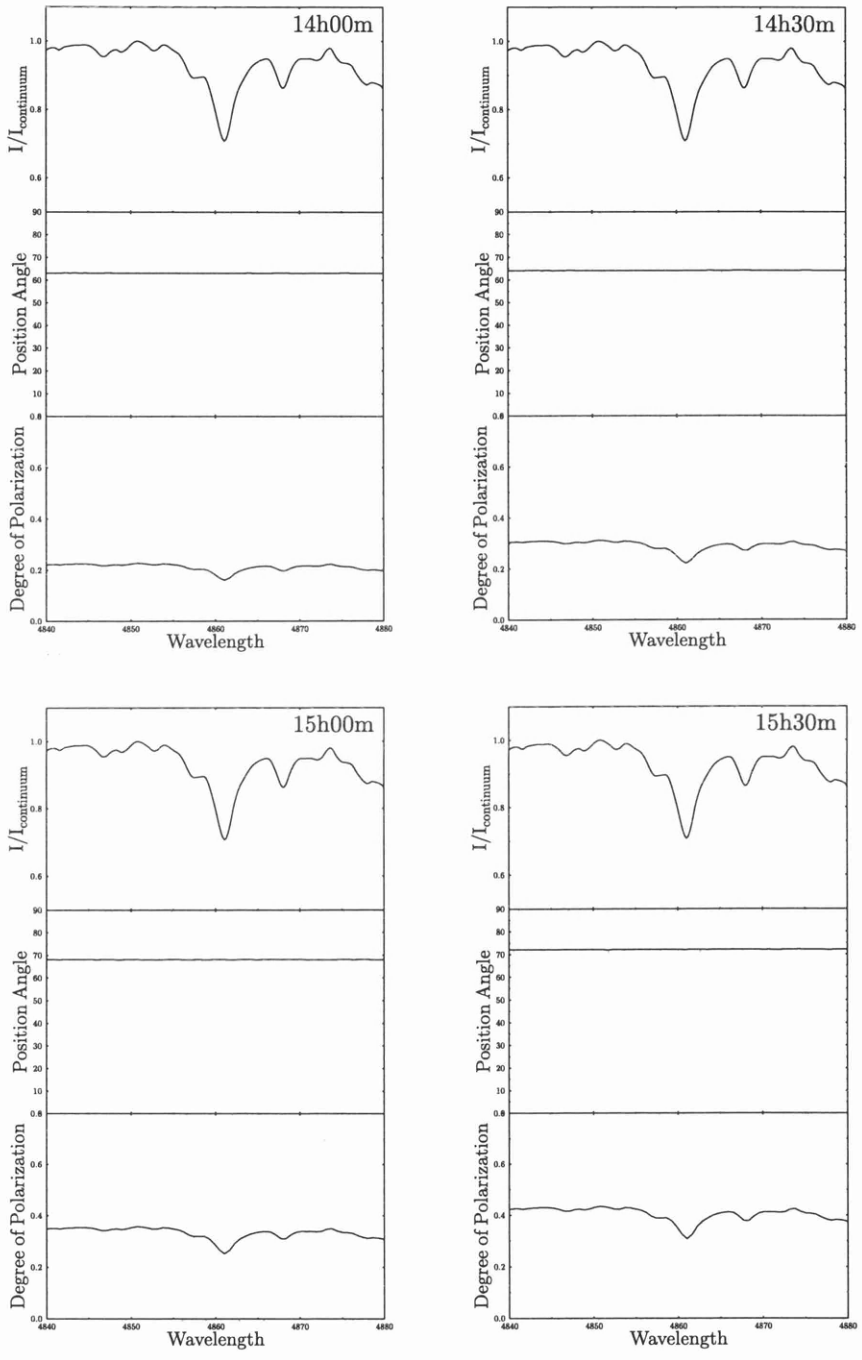

Figure 4.26: Graph of normalized flux, polarization and position angle spectrum for Hβ with time.

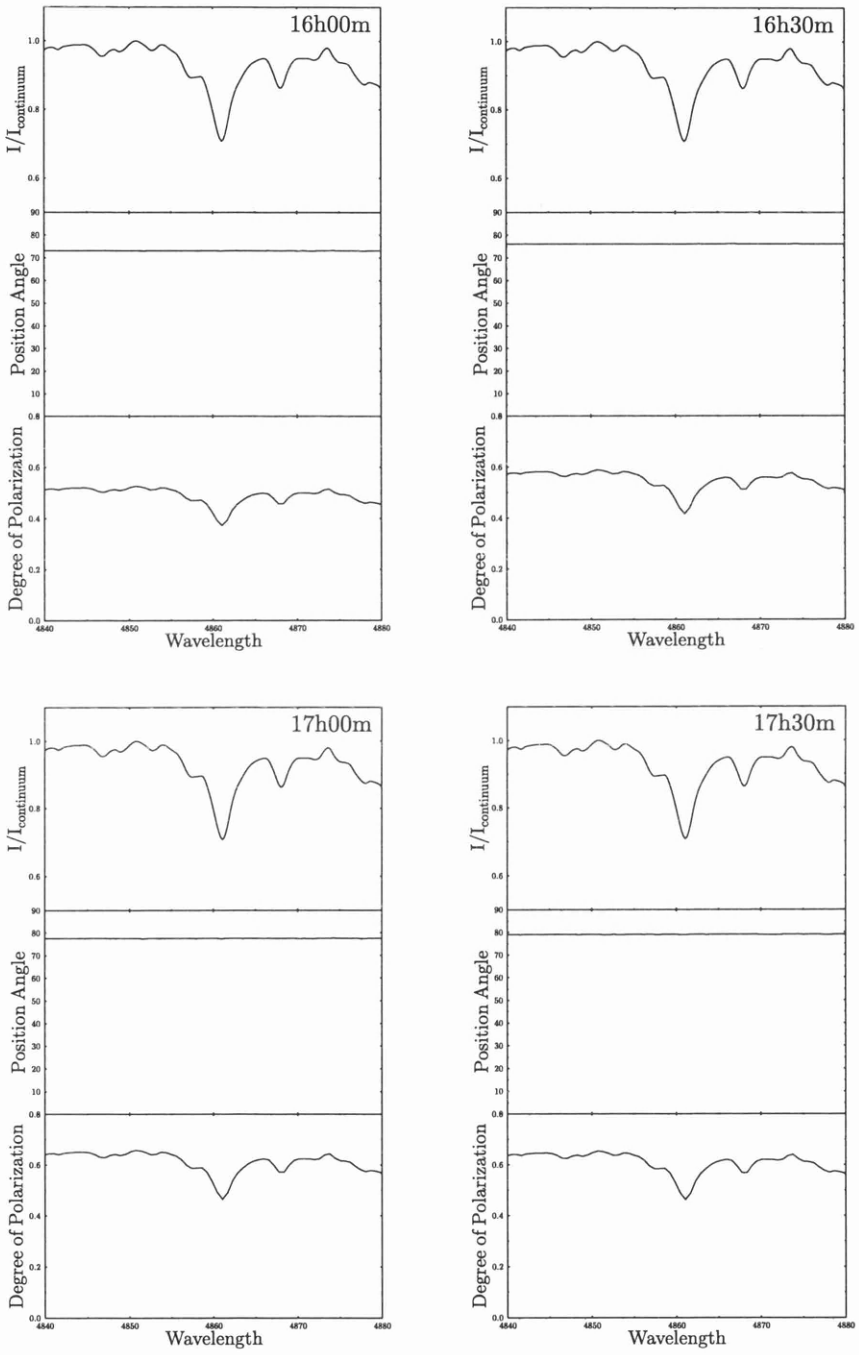

Figure 4.27: Graph of normalized flux, polarization and position angle spectrum for Hβ with time.

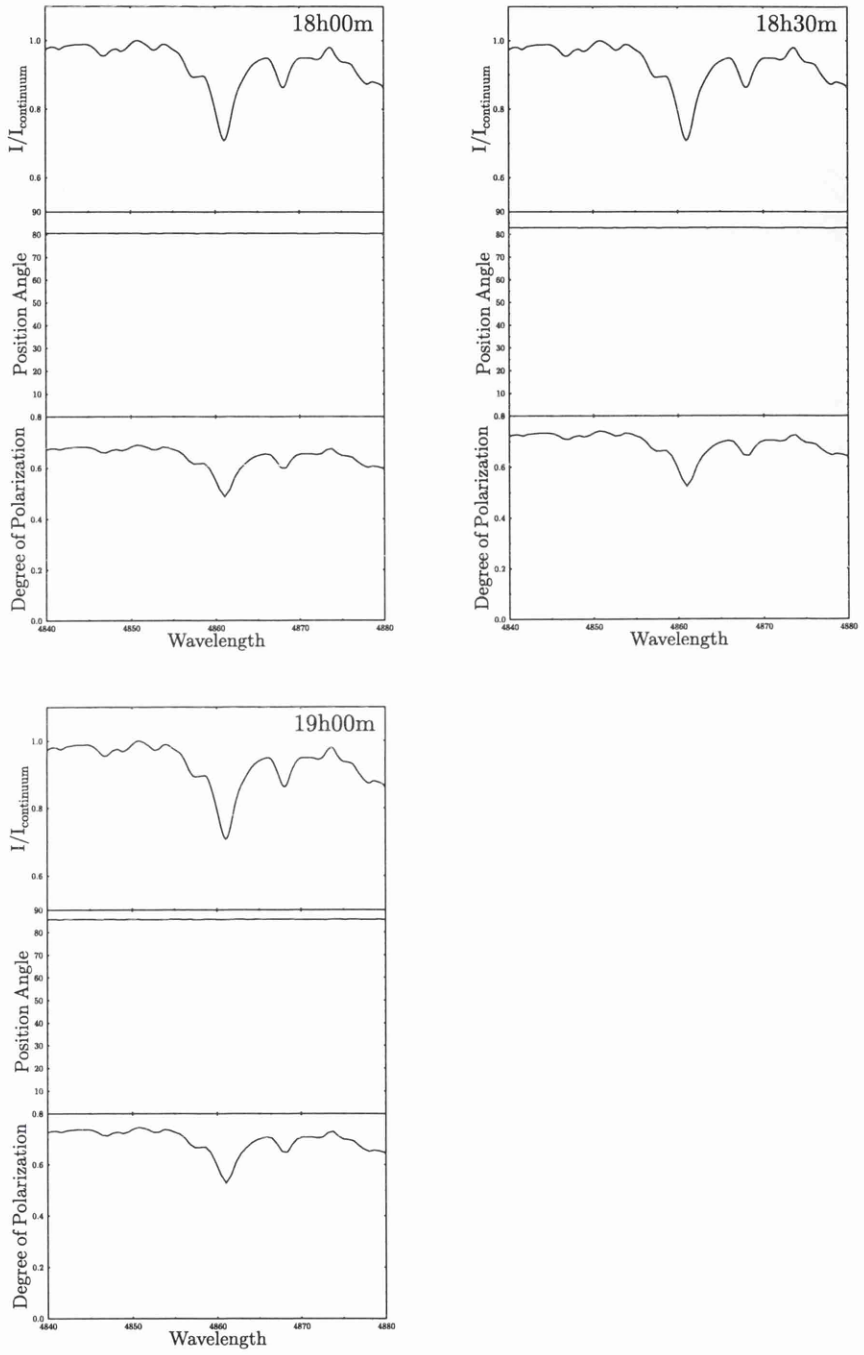

Figure 4.28: Graph of normalized flux, polarization and position angle spectrum for Hβ with time.

4.6.3 Interpretative Model

Although there are many mechanisms that contribute to the Fraunhofer line profiles in spectra of light from the sky being different from those in the original solar radiation, according to Lind and Dravins (1980), the main cause of the filling-in effect is incoherent rotational Raman scattering in the air by N_2 and O_2 molecules. This mechanism was first promoted by Brinkmann (1968) as an explanation of the Ring effect. From the laboratory measurement by Weber et al. (1967) on the Raman scattering by these molecules, Brinkmann deduced the total Raman scattered light within the sky brightness to be some few percent of the Rayleigh component.

The experiment of Weber et al. (1967) reveals a comb of Raman lines either side of the wavelength-unshifted Rayleigh component under an asymmetric "m" shape envelope, the Stokes' lines being slightly more intense than the anti-Stokes' lines. The general shape of this is shown in Figure 4.28. Thus for incoming radiation of a given wavelength, Raman scattered energy is distributed more red-wards rather than blue-wards. For radiation around 5000Å, the peaks of the "m" are about 10Å away from the original wavelength. The shape of the "m" and the structure of the Stokes'/anti-Stokes' components within the envelope are noticeably different for the two molecular species.

In principle, the contribution that Raman scattering makes to the adjustment of the recorded line profiles in the sky spectra, relative to those in the direct solar spectra, could be assessed by undertaking a convolution calculation on the original solar spectrum with the combined "m" combs of N_2 and O_2. For the case of the small spectrometer used in this study, the major effect will be dominated to the first order, not by the details of the individual Raman lines, nor by the comb envelope, but by the peaks either side of the "m" shape comb.

Suppose that the flux entering the observed line of sight column $\mathcal{I}(\lambda)$. The Rayleigh scattered component may be expressed as $\sigma_{Ry} \times \mathcal{I}(\lambda)$ where σ_{Ry} corresponds to integrated scattering cross-section along the column length. This scattered radiation will be linearly polarized and by judicious choice of co-ordinate frame the recorded flux can be represented

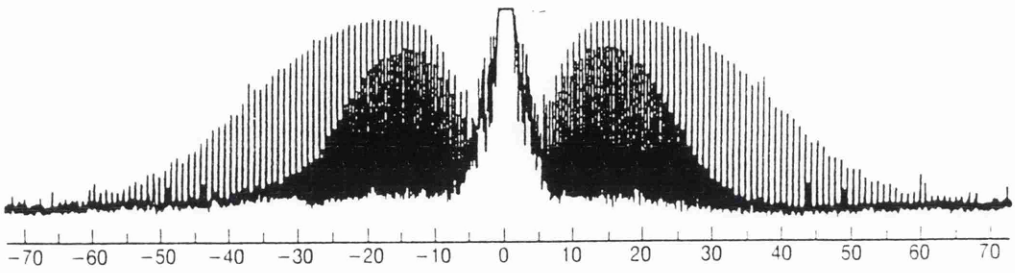

Figure 4.29: Stokes and anti-Stokes lines in a Raman spectrum. Where x axis refers to frequency and y axis to intensity.

as a reduced Stokes' vector in the form:

$$F_{Ry}(\lambda) \Longrightarrow \sigma_{Ry}\mathcal{I}(\lambda) \begin{bmatrix} 1 \\ q_{Ry} \end{bmatrix} \tag{4.14}$$

where q_{Ry} is the degree of polarization. First order, the intensity spectra may be represented by:

$$I(\lambda) + [f_1 \times I(\lambda - \Delta\lambda_1)] + [f_2 \times I(\lambda - \Delta\lambda_2)]$$

where $I(\lambda)$ corresponds to the form of the original solar spectrum - Rayleigh component - and f_1 and f_2 are respectively the fractional contribution at λ of the Stokes' and anti-Stokes' components originating at wavelengths $\lambda - \Delta\lambda_1$ and $\lambda - \Delta\lambda_2$.

The basic asymmetry of the $p(\lambda)$ behaviour across any line profile does suggest that by far the most important process is Raman scattering, previously promoted by Brinkmann (1968), whereby some part of the radiation collected from the zenith column suffers a preferential red shift of an order substantially less than the widths of the observed Fraunhofer

lines. In this way, radiation from the blue continuum influences the blue shoulder of the line, but light from the line core and red wing, being of lower intensity, has smaller effect on the nearby red continuum.

Both the form of the temporal behaviour and the scales of the observed effects cannot, however, be modelled simply by invoking the presence of Rayleigh and Raman scattering alone. At least one other element is required in the model description. Following the earlier reference to the polarization neutral points, interpretation of brightness and polarization maps of the daytime sky requires consideration of contribution of secondary scattering and, for the discussion here, an expression of the symbolic summary as given by Coulson (1974) is applied.

By using a co-ordinate reference frame corresponding to the scattering plane, the recorded radiation at a wavelength, λ, associated with Rayleigh scattering may by summarized by a Stokes' column vector in the form of

$$\begin{bmatrix} I(\lambda) \\ Q(\lambda) \\ 0 \\ 0 \end{bmatrix}_{Obs(\lambda)} = \begin{bmatrix} I(\lambda) \\ Q(\lambda) \\ 0 \\ 0 \end{bmatrix}_{PRy(\lambda)} + \begin{bmatrix} I(\lambda) \\ Q(\lambda) \\ 0 \\ 0 \end{bmatrix}_{SRy(\lambda)} \tag{4.15}$$

with the Rayleigh primary and secondary scattered radiation being separated and subscribed $PRy(\lambda)$, $SRy(\lambda)$ respectively giving rise to the observed, $Obs(\lambda)$, values. The secondary scattered component represents the integrated radiation entering the zenith column from all directions before being redirected downwards to contribute to the total signal. By the judicious choice of reference frame, the third Stokes' parameter, normally designated by U, is equal to zero in each vector, this assuming that the contribution from secondary scattering has symmetry about the original scattering plane and that Faraday rotation effects are negligible. It is also assumed that circular polarization has no part to play and that the fourth Stokes' parameter, normally designated V, is equal to zero in all cases. Radiation entering the zenith column from scattering in the surrounding atmosphere originates preferentially from horizontal planes (i.e. at right angle to the zenith column) and consequently the sign of $Q(\lambda)_{Obs(\lambda)}$ will be opposite to that of $Q(\lambda)_{PRy(\lambda)}$. It is for this reason that some observed lines of sight away from the zenith, the radiation of these parameters provides a zero value for $Q(\lambda)_{Obs(\lambda)}$, so giving rise to the well known

neutral points.

In order to extend the above summary to cover the effect of Raman scattering, consider that, for this component, the incoming radiation of a given wavelength, λ, is simply shifted redwards by a singular amount, $\Delta\lambda$. Again, for simplicity, assume that a result of either Rayleigh or Raman primary scattering is further subject to Rayleigh scattering only in contribution to the total observed intensity, i.e. secondary Raman scattering with a further wavelength shift is unimportant. Thus the Raman contribution results in the addition of two further vectors. By using reduced Stokes' vectors, the situation may now be summarized by:

$$\begin{bmatrix} I(\lambda) \\ Q(\lambda) \end{bmatrix}_{Obs(\lambda)} = \begin{bmatrix} I(\lambda) \\ Q(\lambda) \end{bmatrix}_{PRy(\lambda)} + \begin{bmatrix} I(\lambda) \\ Q(\lambda) \end{bmatrix}_{SRy(\lambda)} + \begin{bmatrix} I(\lambda) \\ Q(\lambda) \end{bmatrix}_{Ra(\lambda-\Delta\lambda)} + \begin{bmatrix} I(\lambda) \\ Q(\lambda) \end{bmatrix}_{SRa(\lambda-\Delta\lambda)} \tag{4.16}$$

where the subscript $Ra(\lambda - \Delta\lambda)$ indicated that the direct Raman scattered contribution now appearing at λ originally came from incoming radiation $(\lambda - \Delta\lambda)$ and subscript $SRa(\lambda - \Delta\lambda)$ refers to the component introduced to the zenith column from primary scattering integrated from all direction and with some part of this subsequently suffering Rayleigh scattering in a downward direction. In a similar fashion to the secondary Rayleigh component as described above, $Q(\lambda)_{SRa(\lambda-\Delta\lambda)}$ will have opposite sign to $Q(\lambda)_{Ra(\lambda-\Delta\lambda)}$. The observed degree of polarization may be represented by:

$$p = \left\{ \frac{Q(\lambda)_{PRy(\lambda)} + Q(\lambda)_{SRy(\lambda)} + Q(\lambda)_{Ra(\lambda-\Delta\lambda)} + Q(\lambda)_{SRa(\lambda-\Delta\lambda)}}{I(\lambda)_{PRy(\lambda)} + I(\lambda)_{SRy(\lambda)} + I(\lambda)_{Ra(\lambda-\Delta\lambda)} + I(\lambda)_{SRa(\lambda-\Delta\lambda)}} \right\} \tag{4.17}$$

A full treatment to obtain values for various contribution is an awesome task and no attempt is made in this thesis. However, it is seen that the interplay of the components and the way in which they account for the polarization measurements can be appreciated. From the observations, whether be it depression or enhancements will depend on the scattering angle and the relative amounts of secondary scattering with the Rayleigh and Raman components.

Chapter 5

General Conclusions

Two high accuracy polarimtric experiments have been described in this thesis which confirm the potential of CCDs in this area. In the first, the device provides a large number of "light buckets" to measure bright stars in a time efficient way, demonstrating its advantage over the "single pixel" photoelectric device. For the second, the true 2-D advantage of the CCD has been demonstrated by undertaking spectropolarimetry of the light from the daytime sky, providing a new understanding of the Ring effect. As for the future of 2D detectors in polarimetry, research is underway (see Rust and Thompson, 1992) to produce CCD chips with dichroic lenslets covering the pixels, making the basic detector itself self-imaging and sensitive to polarized light. Their exploitation is now awaited.

5.1 Imaging CCD Polarimetry

Although it has served us well in the past, the classical photoelectric technique is clearly outclassed by the modern solid state devices such as CCDs. The high accuracy measurement described in this thesis confirms the potential of CCDs when used in an aperture imaging system. Although array detectors are most often used in polarimetry to obtain two-dimensional images of the sun in a narrow spectral bandpass or spectral along a slit, they can also be used for very sensitive one-dimensional measurements.

Aperture imaging experiments have been carried out at the University of Glasgow Chocno station, using the 510 mm Cassegrain telescope. After the focal plane field stop, a rotatable superachromatic half-wave plate was placed prior to a Savart plate and resolved orthogonal images focused on an SBIG ST6 CCD camera. In order to be able to estimate the photon shot noise, the variance method for determining the number of electrons per ADU was applied in the laboratory.

A simple prototype instrument described has opened the way for reaching high precision. It was shown that by using the CCD detector as a light collecting bucket it is possible to reduce the uncertainty values on the degree of polarization way beyond the photomultiplier techniques. CCDs provide an inherently high efficiency of measurements by taking 10^4 – 10^6 simultaneous measurements.

With this equipment, a single measurement of a defocused star, θBoo (mag 4.5), resulted in polarimetric noise level of $\sim \pm 0.01\%$. This was achieved by integrating along the CCD rows and columns. The number of pixels chosen for this experiment were 3200 pixels. The above accuracy was achieved on white light (no wavelength discrimination). The deterioration in expected accuracy results from the read-out noise. The above can be greatly improved by using a more professional system with low readout noise. Also by making full use of the CCD area by overcoming the overlap problems.

The results indicate the power of the technique in its application to accurate measurements of the low polarization associated with bright stars, an area for future exploration that cannot be realistically undertaken by standard photoelectric systems. By using larger telescopes and larger CCD chips with low readout noise and increase in full-well capacity, it would seem feasible to achieve polarimetric accuracies of ± 0.00001, this being a requirement, say for the study of solar type stars (see Clarke and Fullerton, 1996).

5.2 Terrestrial Blue Sky Spectropolarimetry

So far spectral line $p(\lambda)$ investigations of Ring effect have been performed by sequential measurements alternating between wavelength positions corresponding to the line core and

the nearby continuum. Consequently the complete spectral profiles were impossible. This observational technique is also inefficient and the results provide no real understanding of the phenomenon.

A spectropolarimeter was built incorporating a CCD detector to investigate the Ring effect. This instrument comprised a camera lens, followed by a half-wave plate, polarizer and a spectrometer. Two Fraunhofer lines were chosen for this study, one centered around the magnesium triplets (5183Å) and the other at Hβ (4861Å). The data reveals several "anomalies" which have not been reported by previous investigators.

For example, Harrison (1975) reported that there is a pronounced diurnal variation in the Ring effect. However, photometric results obtained here showed that there is no diurnal variations within the Fraunhofer lines. Hence, rejecting the evidence provided by Harrison (1975). It should be mentioned that Harrison seems not to have accounted for the instrumental effects caused by the strong polarization and rapid change of direction of vibration acting on the spectrometer.

The polarization measurements at magnesium lines revealed that at low scattering angles, there is an enhancement in the blue shoulder and depression in the line bottom, while at high scattering angle the enhancements were pronounced. However, the polarization profile of Hβ showed that there is no enhancement at the blue or red shoulder throughout the day.

There was also times (30 minutes either side of local noon) during the day in which there was no detectable polarization at the line bottom and continuum. This was present in the two sets of data.

These behaviours were modelled by considering scattering by the diatomic molecules of nitrogen and oxygen with dominance of Stokes shifted radiation in combination with Rayleigh scattering. As the energy redistribution is mainly towards the red, light from the continuum affects the blue shoulders of the lines but light from within the line of lower intensity has a lesser effect on the nearby red continuum. The fact that there are scattering angles at which the effects disappear requires an element of secondary scattering, also invoked to explain the polarimetric neutral points of Arago, Brewster and Babinet

occuring at specific angles from the Sun. These results are key to an explanation of the enigmatic behaviour of the Ring effect.

Unfortunately, due to the adverse weather in Glasgow it was not possible to carry out further observations of these lines. It is proposed that further observations of the Ring effect be performed at a better site. These observations must be carried out at different times of the year. This will enable one to see if the variations in the polarization profiles of Fraunhofer lines are seasonal.

Appendix A

Recent Developments in Precision Polarimetry

Since the publication of this thesis, there have been some advances in the polarimetric precision. Some of these advances are briefly reviewed in this appendix.

Magalhaes et al. (1996) have described a direct CCD imaging polarimeter at the CTIO (Cerro Tololo Interamerican Observatory, Chile). Their method employs a rotatable retarder and a Savart plate. They claim to have achieved a high precision for non-extended sources. It is claimed by the authors that the polarimetric precision is in the order of 0.03%. They state that the polarimetric errors are within the predicted photon noise error of 0.02%.

The work carried out by Keller (1996) has resulted in obainting a spectropolarimetric precision of <0.01% by coadding many frames. The instrument used is called - ZIMPOL I, loacted at the National Solar Observatory, USA. The instrument setup can be found in Keller et al. (1992), Povel et al. (1994) and Povel (1995). The advantage of this instrument is that it can also be used to obtain a circular polarization. It is commented by the author that by reaching these high polarimetric accuracy the instrumental effects produces spurious polarization.

For a number of years now the WHT of the Royal Greenwich Observatory, UK, has been capable of operating in the spectropolarimetry mode. Tinbergen and Rutten (1992) describes the instrument and procedures needed to achieve an instrumental precision of order of 0.01%. The polarimeric instrumentation described in this thesis is based on WHT instrument.

Other worker such as Hough et al. (1991) and Smith et al. (1994) also discuss ways in which polarimetric precision can be improved.

Bibliography

Babcock, H. W.: 1947, *Ap. J.* **105**, 105

Baldiali, M., Catala, C., Favata, F., Fridlund, M., Franden, S., Gough, D. O., Hoyng, P., Pace, O., Roca-Cortés, T., Roxburgh, I. W., Sterken, C., and Volonté, S.: 1996, *STARS, Seismic Telescope for Astrophyical Research from Space*, Technical report, ESA

Barmore, F. E.: 1975, *J. Atmospheric Sci.* **32**, 1489

Bartl, E.: 1959, *Universitäts–Sternwarte zu Jena* **39**, 5

Bastien, P., Drissian, L., Menard, F., Moffat, A. F. J., Roberts, C., and St-Louis, N.: 1988, *The Astronomical Journal* **495**, 900

Baur, T. G.: 1981, *Optical Engineering* **20(1)**, 2

Birnkmann, R. T.: 1968, *Ap. J.* **154**, 1087

Boksenberg, A. and Burgess, D. E.: 1973, in J. W. Glaspey and G. A. H. Walker (eds.), *Astronomical Observations with Television-Type Sensors*, University of British Columbia

Born, M. and Wolf, E.: 1965, *Polarized Light and Optical Measurement*, Pergamon Press, Inc., New York

Boyer, G. R., Lamouroux, B., Prade, B. S., and Vinet, J. Y.: 1981, *Optical Engineering* **20(1)**, 44

Breckinridge, J. B.: 1971, *Applied Optics* **10**, 286

Breger, M.: 1986, in J. B. Hearnshaw and P. L. Cottrell (eds.), *Instrumentation and research programmes for small telescopes*, pp 149–157, IAU Symposium No. 118, Kluwer Academic

Brinkmann, R.: 1968, *Astrophys. Journal* **154**, 1087

Brooks, A., Clarke, D., and McGale, P. A.: 1994, *Vistas in Astronomy* **38**, 377

Buil, C.: 1991, *CCD Astronomy: Construction and Use of an Astronomical CCD Camera*,

Willmann-Bell Inc.

Chandrasekhar, S.: 1946, *Astrophysical Journal* **103**, 351

Chandrasekhar, S.: 1947, *Astrophysical Journal* **105**, 424

Clarke, D.: 1965, *Monthly Notices of the Royal Astronomical Society* **129(1)**, 71

Clarke, D.: 1991, *Vistas in Astronomy* **34**, 303

Clarke, D. and Basurah, H.: 1989, *Plant. Space Sci.* **37**, 627

Clarke, D. and Bjorkman, K.: 1998, *Astronomy and Astrophysics Journal* in press

Clarke, D., Deighan, G., Fry, G., Goodsir, S., and MacLeod, D.: 1996, *Experimental Astronomy* In press

Clarke, D. and Fullerton, S.: 1996, *Astronomy and Astrophysics Journal* **310**, 331

Clarke, D. and Grainger, J. F.: 1971, *Polarized Light and Optical Measurement*, Pergamon Press, Oxford

Clarke, D. and McLean, I. S.: 1975, *Plant. Space Sci.* **23**, 557

Clarke, D. and Naghizadeh-Khouei, J.: 1994, *The Astronomical Journal* **108(2)**, 687

Clarke, D., Naghizadeh-Khouei, J., Simmons, J. F. L., and Stewart, B. G.: 1993, *Astronomy and Astrophysics Journal* **269**, 617

Clarke, D., Stewart, B. G., Schwarz, H. E., and Brooks, A.: 1983, *Astronomy and Astrophysics Journal* **126**, 260

Clemens, D. and Leach, R. W.: 1987, *Optical Engineering* **26(9)**, 923

Cooper and Walker: 1989, *Getting the measure of the stars*, Adam Hilger

Coulson, K. L.: 1974, in T. Gehrels (ed.), *Planets, Stars and Nebulae Studied with Photopolarimetry*, pp 444–471, University of Arizona Press

Davis, L. and Greenstein, J. L.: 1951, *Astrophysical Journal* **114**, 206

Dekker, H. and D'Odorico, S.: 1986, *Messenger* **46**, 21

Dollfus, A.: 1953, *Archives Acad. Sci. Paris* ***, **

Dyck, H. M., Forbes, F. F., and Shawl, S. J.: 1971, *Astron. J.* **76**, 43

Fernie, J. D.: 1976, *Publication of the Astronomical Society of Pacific* **88**, 969

Fessenkov, V. G.: 1935, *Astronomical J. of Soviet Union* **XII**, 309

Fosbury, R., , di Serego Alighier, S., Tadhunter, C. N., and Quinn, P. J.: 1989, *The Messenger* **57**, 49

Fosbury, R., Cimatti, A., and di Serego Alighier, S.: 1993, *The Messenger* **74**, 11

Gehrels, T.: 1974, *Planets, Stars and Nebulae Studied with Photopolarimetry*, University

of Arizona Press

Grainger, J. F. and Ring, J.: 1962, *Nature* **193**, 762

Gudehus, D. H. and Hegyi, D. J.: 1985, *The Astronomical Journal* **90(1)**, 130

Hall, J. S.: 1949, *Science* **109**, 166

Harries, T. and Howarth, I.: 1996, *Astronomy and Astrophysics Journal* in press

Harrison, A.: 1976, *Can. J. Phys.* **54**, 1000

Harrison, A. and Kendall, D.: 1974, *Can. J. Phys.* **52**, 940

Harrison, A. W.: 1975, *Can. J. Phys.* **54**, 1000

Hiltner, W. A.: 1947, *Ap. J.* **106**, 231

Hiltner, W. A.: 1949, *Science* **109**, 165

Hough, J. H., Peacock, T., and Bailey, J. A.: 1991, *Mon. Not. Roy. Astron. Soc.* **248**, 74

Howarth, I. D. and Prinja, R. K.: 1989, *Astronomy and Astrophysics Supplement* **69**, 527

Hsu, J. and Breger, M.: 1982, *The Astrophysical Journal* **262**, 732

Janesick, J. R., Elliott, T., Daud, T., and Campbell, D.: 1985, *SPIE* 590

Janssen, E.: 1946, *Ap. J.* **103**, 380

Keller, C. U.: 1996, in J. O. Stenflo and K. N. Nagendra (eds.), *Solar Physics*, pp 243–252, Kluwer Academic Publishers

Keller, C. U., Aebersold, F., Egger, U., Povel, H. P., Steiner, P., and Stenflo, J. O.: 1992, *LEST Polarimeter*, Technical report, LEST

Kjeldsen, H. and Frandsen, S.: 1992, *Publication of the Astronomical Society of Pacific* **104**, 413

Kruszewski, A., Gerrels, T., and Serkowski, K.: 1968, *Astron. J.* **73**, 677

Lind, J. and Dravins, D.: 1980, *Astron. & Astrophys. Journal* **90**, 151

Lyot, B.: 1948a, *C. R. Acad. Sci. Paris* **226**, 25

Lyot, B.: 1948b, *C. R. Acad. Sci. Paris* **226**, 137

Mackay, C. D.: 1986, in G. Burbidge, D. Layzer, and J. G. Phillips (eds.), *Annual Review of Astronomy and Astrophysics*, Vol. 24, pp 255–283, Annual Reviews Inc.

Magalhaes, A. M., Rodrigues, C. V., Margoniner, V. E., and Pereyra, A.: 1996, in W. Roberge and D. Whittet (eds.), *Polarimetry of the Intestellar Medium*, pp 118–122, Astronomical Society of the Pacific

McLean, I. S., Cormack, W. A., Herd, J. T., and Aspin, C.: 1981, in J. C. Geary and D. W. Latham (eds.), *Solid State Images for Astronomy*, Vol. 290, pp 155–158, Proc.

SPIE

McLean, I. S., Coyne, G. V., Frecker, J. E., and Serkowski, K.: 1979, *The Astrophysical Journal* **228**, 802

Meisenheimer, K. and Röser, H. J.: 1986, in J. P. Baluteau and S. D'Odoric (eds.), *The Optimization of the Use of CCD Detectors in Astronomy*, Vol. 25, pp 227–236, ESO-OHP Workshop, ESO Conference and Workshop Proceedings

Metz, K.: 1979, *Mitt. Astron. Ges.* **45**, 39

Miller, J. S., Robinson, L. B., and Schmidt, G.: 1980, *Publication of the Astronomical Society of Pacific* **92**, 702

Miller, R.: 1963, *Applied Optics* **2(1)**, 61

Noxon, J. and Goody, R.: 1965, *Atm. and Oceanic Phys.* **1**, 275

Öhman, Y.: 1949, *Stockholm Obs. Ann.* **226(8)**, **

Pavlov, V., Teifel, Y., and Golovachev, V.: 1973, *Soviet Phys. Dokl.* **17**, 1038

Pickering, E.: 1874, *Proceedings of Amer. Acad. Arts and Sciences* **IX**, 135

Poretti, E.: 1992, *The Messenger* **68**, 52

Povel, H., Aebersold, H., and Stenflo, J. O.: 1990, *Applied Optics* **29(8)**, 1186

Povel, H. P.: 1995, *Opt. Eng.* **34**, 1545

Povel, H. P., Keller, C. U., and Yadigaroglu, I. A.: 1994, *Applied Optics* **33**, 4254

Rayleigh: 1871, *Phil. Mag.* **41**, 107

Röser, H. J.: 1981, *Astronomy and Astrophysics Journal* **103**, 374

Rudy, R. J. and Kemp, J. C.: 1978, *The Astrophysical Journal* **221**, 200

Rust, D. and Thompson, K.: 1992, *Space Physics Group - The John Hopkins University* **Preprint 03-92**, 1

Sánchez-Almeida, J. and Martinez-Pillet, V.: 1992, *Astronomy and Astrophysics Journal* **260**, 543

Sánchez-Almeida, J., Martinez-Pillet, V., and Wittmann, A. D.: 1991, *Solar Physics* **134**, 1

Scarrott, S. M., Warren-Smith, R. F., Pallister, W., Axon, D. J., and Bingham, R.: 1983, *Monthly Notices of the Royal Astronomical Society* **204(3)**, 1163

Schectman, S. and Hiltner, W. A.: 1976, *Publication of the Astronomical Society of Pacific* **88**, 960

Scholiers, W. and Wieher, E.: 1985, *Solar Physics* **99**, 349

Serkowski, K.: 1970, *Astrophys. J.* **160**, 1083

Serkowski, K.: 1974a, in T. Gehrels (ed.), *Planets, Stars and Nebulae Studied with Photopolarimetry*, pp 135–174, University of Arizona Press

Serkowski, K.: 1974b, in N. Carleton (ed.), *Methods in Experimental Physics*, Vol. 12, pp 361–414, Academic Press

Shurcliff, W. A.: 1967, *Polarized Light*, Harvard University Press, Cambridge

Simmons, J. F. L. and Stewart, B. G.: 1985, *Astronomy and Astrophysics Journal* **142**, 100

Smith, C. H., Aitken, D. K., and Moore, T. J. T.: 1994, *SPIE* **736**, 2198

Stenflo, J. O. and Povel, H.: 1985, *Applied Optics* **24(22)**, 3893

Stockman, H. S.: 1982, in D. L. Crawford (ed.), *Instrumentation in Astronomy IV*, Vol. 331, pp 76–80, Proc. SPIE

Stockman, H. S., Angel, J. R. P., and Heir, R.: 1979, *The Bulletin of American Astronomical Society* **10**, 689

Stokes, G. G.: 1852, *Trans. Cambridge Phil. Soc.* **9**, 399

Tinbergen, J.: 1974, in T. Gehrels (ed.), *Planets, Stars and Nebulae Studied with Photopolarimetry*, pp 175–188, University of Arizona Press

Tinbergen, J. and Rutten, R. G. M.: 1992, *A User Guide to WHT Spectropolarimetry, La Palma*, Technical report, Royal Greenwich Observatory

Tyson, J. A. and Lee, R. W.: 1981, in J. C. Geary and D. W. Latham (eds.), *Solid State Imagers for Astronomy*, Vol. 290, pp 144–149, Proc. SPIE

Warren-Smith, R. F., Scarrot, S. M., Murdin, P., and Bingham, R. G.: 1979, *Monthly Notices of the Royal Astronomical Society* **187**, 761

Weber, A., Porto, S., Cheesman, L., and Barrett, J.: 1967, *J. Opt. Soc. Am.* **57**, 19

Young, A. T.: 1973, *Icarus* **18**, 564